DGK Deutsche Geodätische Kommission
der Bayerischen Akademie der Wissenschaften

Reihe C | Dissertationen | Heft Nr. 770

Ilias Daras

Gravity field processing towards future LL-SST satellite missions

München 2016

Verlag der Bayerischen Akademie der Wissenschaften
in Kommission beim Verlag C. H. Beck

ISSN 0065-5325 ISBN 978-3-7696-5182-9

DGK Deutsche Geodätische Kommission
der Bayerischen Akademie der Wissenschaften

Reihe C Dissertationen Heft Nr. 770

Gravity field processing towards future LL-SST satellite missions

Vollständiger Abdruck
der von der Ingenieurfakultät Bau Geo Umwelt
der Technischen Universität München
zur Erlangung des akademischen Grades eines
Doktor-Ingenieurs (Dr.-Ing.)
genehmigten Dissertation

von

Ilias Daras

München 2016

Verlag der Bayerischen Akademie der Wissenschaften
in Kommission beim Verlag C. H. Beck

ISSN 0065-5325 ISBN 978-3-7696-5182-9

Adresse der Deutschen Geodätischen Kommission:

Deutsche Geodätische Kommission

Alfons-Goppel-Straße 11 ● D – 80 539 München

Telefon +49 – 89 – 23 031 1113 ● Telefax +49 – 89 – 23 031 - 1283 / - 1100

e-mail hornik@dgfi.badw.de ● http://www.dgk.badw.de

Prüfungskommission

Vorsitzender:	Univ.-Prof. Dr.-Ing. habil. T. Wunderlich
Prüfer der Dissertation:	1. Univ.-Prof. Dr.techn. R. Pail
	2. Univ.-Prof. Dr.-Ing. Dr. h.c. mult. R. Rummel (i.R.)
	3. Ass. Prof. Dr.-ir. P.N.A.M. Visser, Technische Universität Delft, Niederlande

Die Dissertation wurde am 29.10.2015 bei der Technischen Universität München eingereicht
und durch die Ingenieurfakultät Bau Geo Umwelt am 29.01.2016 angenommen.

.

Diese Dissertation ist auf dem Server der Deutschen Geodätischen Kommission unter <http://dgk.badw.de/>
sowie auf dem Server der Technischen Universität München unter elektronisch publiziert

---

ISSN 0065-5325 ISBN 978-3-7696-5182-9

Technische Universität München

Gravity field processing towards future LL-SST satellite missions

Dissertation by

Ilias Daras

Institute of Astronomical and Physical Geodesy

Technische Universität München

Ingenieurfakultät Bau Geo Umwelt

Lehrstuhl für Astronomische und Physikalische Geodäsie

Gravity field processing
towards future LL-SST satellite missions

Ilias Daras

Vollständiger Abdruck der von der Ingenieurfakultät Bau Geo Umwelt
der Technischen Universität München zur Erlangung des akademischen Grades eines

Doktor-Ingenieurs (Dr.-Ing.)

genehmigten Dissertation.

Vorsitzender:		Univ.-Prof. Dr.-Ing. habil. T. Wunderlich
Prüfer der Dissertation:	1.	Univ.-Prof. Dr.techn. R. Pail
	2.	Univ.-Prof. Dr.-Ing. Dr. h.c. mult. R. Rummel (i.R.)
	3.	Ass. Prof. Dr.-ir. P.N.A.M. Visser, Technische Universität Delft, Niederlande

Die Dissertation wurde am 29. Oktober 2015 bei der Technischen Universität München eingereicht und durch die Ingenieurfakultät Bau Geo Umwelt am 29.01.2016 angenommen.

Acknowledgments

I would like to express my deepest gratitude to Prof. Roland Pail
for his guidance and supervision of this PhD study.

I am also thankful to Prof. Reiner Rummel and Prof. P.N.A.M. Visser
for their contributions in improving this manuscript.

I would like to deeply thank my parents
for their immense support since the early days of my education.

Finally, I would like to thank my wife *Χρυσάνθη*
for her warm support and encouragement over all these years.

Summary

This study focuses on important aspects concerning gravity field processing of future Low-Low Satellite-to-Satellite Tracking (LL-SST) satellite missions. Closed-loop simulations taking into account error models of new generation instrument technology are used to estimate the gravity field accuracy that future missions could provide. Limiting factors are identified, and methods for their treatment are developed. The contribution of all error sources to the error budget is analyzed. It is shown that gravity field processing with double precision may be a limiting factor for exploiting the nm-level accuracy of a laser interferometer. An enhanced numerical precision processing scheme is proposed instead, where double and quadruple precision is used in different parts of the processing chain. It is demonstrated that processing with enhanced precision can efficiently handle laser measurements and take full advantage of their accuracy, while keeping the computational times within reasonable levels. However, error sources of considerably larger impact are expected to affect future missions, with the accelerometer instrument noise and temporal aliasing effects being the most significant ones. The effect of time-correlated noise such as the one present in accelerometer measurements, can be efficiently handled by frequency dependent data weighting. Residual time series that contain the effect of system errors and propagated accelerometer and laser noise, is considered as a noise realization with stationary stochastic properties. The weight matrix is constructed from the auto-correlation functions of these residuals. Applying the weight matrix to a noise case considering all error sources leads to reduction of the error level over the complete spectral bandwidth. Co-estimation of empirical accelerations does not show the same efficiency in reducing the propagated noise with the applied processing strategy. Temporal aliasing effects are reduced essentially by adding a second pair of satellites at an inclined orbit. Compared to a GRACE-type near-polar pair, such a Bender-type constellation delivers solutions with major improvements in terms of de-aliasing potential and recovery performance. When the integrated effect of all geophysical processes is recovered, the maximum spatial resolution of 11-day solutions can be increased from 715 to 315 km half-wavelength. A further reduction of temporal aliasing errors is possible by co-parameterizing low resolution gravity fields at short time intervals, together with the higher resolution gravity field which is sampled at a longer time interval. One day was found to be the optimal sampling period for reducing the error levels in the solutions. A uniform sampling at the co-parameterized short periods, is a prerequisite for an efficient reduction of aliasing errors. High frequency atmospheric signals are captured by daily solutions to a large extent. Hence co-parameterization at daily basis results in significant reduction

of aliasing caused by their under-sampling. This enables future gravity satellite missions to deliver the complete spectrum of Earth's geophysical processes. The corresponding by-products of daily gravity field solutions are expected to be very useful to atmospheric science and open doors to new fields of application.

Zusammenfassung

Diese Doktorarbeit befasst sich schwerpunktmäßig mit der Schwerefeldprozessierung zukünftiger Low-Low Satellite-to-Satellite (LL-SST) Satellitenmissionen. Um die Genauigkeit zukünftiger Satellitenmissionen abzuschätzen, wurden Closed-loop Simulationen unter Einbeziehung von Fehlermodellen neuer Instrumentengenerationen durchgeführt. Einschränkende Faktoren werden erörtert und entsprechende Lösungansätze entwickelt. Der Beitrag aller Fehlerquellen zum gesamten Fehlerbudget wird quantifiziert. Es wird nachgewiesen, dass die Schwerefeldprozessierung mit doppelter Rechengenauigkeit ein limitierender Faktor für die Ausschöpfung der nm-Messgenauigkeit eines Laserinterferometers sein kann. Ein alternatives Prozessierungsschema erhöhter Rechengenauigkeit wird stattdessen vorgeschlagen, in dem doppelte und vierfache Rechengenauigkeit in verschiedenen Prozessierungsschnritten verwendet wird. Es wird demonstriert, dass in diesem Fall Laserbeobachtungen mittels erhöhter Genauigkeit wirkungsvoll prozessiert werden können und deren Präzision voll ausgenutzt werden kann. Gleichzeitig bleibt der Rechenaufwand in angemessenen Grenzen. Allderdings, werden sich voraussichtlich andere Fehlerquellen stärker auf zukünftige Satellitenmissionen auswirken. Das Rauschen der Beschleunigungsmesser und die Effekte von zeitlichem Aliasing stellen die beiden größten Fehlerquellen dar. Fehler infolge von zeitkorreliertem Rauschen, wie z.B. in den Beobachtungen der Beschleunigungsmesser, können wirkungsvoll mittels frequenzabhängiger Datengewichtung behandelt werden. Eine Zeitreihe von Residuen, die den Effekt vom Systemrauschen, propagiertem Beschleunigungsmessrauschen und Laserrauschen beinhaltet, werden als Rauschrealisierung mit stationären stochastischen Eigenschaften berücksichtigt. Basierend darauf wird die Gewichtungsmatrix durch Autokorrelationfunktionen erstellt. Die Einbeziehung der Gewichtungsmatrix in einem Fall, der alle Fehlerquellen betrachtet, führt zur Reduzierung des Fehlerniveaus über das gesamte Spektrum. Dagegen führt das Mitschätzen von empirischen Beschleunigungen nicht zu derselben gleichmässigen Reduzierung von Fehlern. Effekte von zeitlichem Aliasing reduzieren sich wesentlich durch die Erweiterung um ein zweites Satellitenpaar mit inklinierter Bahn. Im Vergleich zu einem GRACE-ähnichen Paar mit fast polarer Bahn liefert eine solche Bender Konstellation verbesserte Ergebnisse hinsichtlich der Reduzierung von Aliasingeffekten und erzielbarer Genauigkeit. Wenn eine integrierte Wirkung aller geophysikalischer Prozesse betrachtet wird, kann sich die maximale räumliche Auflösung einer 11-tägigen Lösung von 715 auf 315 km halbe Wellenlänge steigern. Eine weitere Reduzierung der zeitlichen Aliasing-Effekte ist möglich durch Mitschätzung von niedrig aufgelösten Schwerfeldlösungen über kurze Zeitspannen, zusammen

mit der hoch aufgelösten Schwerfeldlösung, die über eine längere Zeitspanne abgetastet wird. Der optimale Abtastzeitraum für kurze Zeitspannen zur Reduzierung des Fehlerniveaus beträgt einen Tag. Ein einheitliches Abtasten innerhalb der kurzer Zeitspannen ist eine Voraussetzung für eine effektive Reduzierung der Aliasingfehlern. Hochfrequente Signale der Atmosphäre können in großem Maß aus täglicher Parametrisierung erfasst werden. Somit führt die Co-Parametrisierung in täglichen Zeitspannen zu einer signifikantent Reduzierung der Aliasingfehler. Das ermöglicht zukünftigen Satellitenmissionen, das ganze Spektrum von geophysikalischen Prozessen der Erde zu erfassen. Die entsprechenden täglichen Schwerefeldlösungen stellen zusätzliche Produkte dar, die nützlich für die Atmosphärenforschung sein konnen. Damit öffnen sich Perspektiven für gänzlich neue Anwendungen.

Contents

Chapter 1

Introduction

1.1 Background

Earth is a living planet that is subject to substantial changes due to processes and interactions between its geophysical sub-systems; namely the atmosphere, hydrosphere, biosphere and geosphere. A significant amount of these processes is related to mass redistribution in the Earth system and thus is translated into changes of the gravity field of the Earth. Knowledge about Earth's gravity field properties is therefore fundamental for many applications of Earth sciences. Gravity measurements contribute to the computation of geoid models used for regional height reference systems, thus allowing the combination of Global Positioning System (GPS) with classical leveling techniques. Global satellite observations are used for the computation of a global geoid model, with the ambitions to unify regional height systems into a global reference system, hence making local or continental height systems comparable. Geoid models are also very useful in the field of oceanography, where geoid heights are subtracted from sea surface heights (measured by satellite altimetry), to deliver the sea surface topography. The latter is used in ocean circulation modeling, which is the basis for understanding the global heat balance. Knowledge of Earth's gravity field is therefore implicitly a very valuable input for the computation of global climate models. Moreover, temporal gravity field changes are used to quantify changes in the global water balance, such as the polar ice cap melting, mean sea level change and seasonal changes in the water balance of large river basins. Global gravity observations contribute to the computation of hydrological, glaciological and Glacial Isostatic Adjustment (GIA) models. Finally, geophysical and geodynamical models used in solid Earth applications are improved from gravity field information. These models are very useful for a better interpretation of seismic events, volcanic processes and plate tectonics, as well as for the exploration of natural resources.

Space observations provide the only means to monitor and assess changes of Earth's sub-systems on a global and long-term perspective. They deliver long and continuous time series of important Earth system parameters, which contribute to the analysis and prediction of these changes. Mass distribution and transport processes in the Earth system consist mainly of dynamic processes in cryosphere, continental

hydrology, ocean, atmosphere and solid Earth. At the end of the 20th century, tracking data from satellite missions using various observation techniques (e.g. SLR, Doppler, PRARE, Doris or GPS) have been used to improve our knowledge on Earth's gravity field. In 2000, the era of dedicated geopotential missions began with the launch of the Challenging Minisatellite Payload (CHAMP) (ended in 2010) (Reigber, 1995). The Gravity Recovery and Climate Experiment (GRACE) (2002~present) (Tapley et al., 2004) and the Gravity field and steady-state Ocean Circulation Explorer (GOCE) (2009~2013) (Rummel et al., 2011) dedicated gravity missions that followed, resulted in remarkable improvements in the knowledge of Earth's time-varying and static gravity field, respectively. The great success of GRACE in mapping Earth's mass changes, established its products applicable to a large spectrum of Earth sciences. The continuity of the time-varying gravity field time series, is enabled by the upcoming launch (August 2017) of GRACE's successor, namely the GRACE Follow-On (GRACE-FO) mission (Flechtner et al., 2014a). GRACE-FO is a gap-filling mission that will cover the timespan between GRACE and Next Generation Gravity Missions (NGGMs) to be launched in the mid-term future (after 2020).

1.2 Motivation and objectives of this study

Dedicated gravity missions delivering observations for a period longer than 15 years, have left a precious heritage for studies of future satellite mission designs. The employment of different measuring techniques such as High-Low Satellite-to-Satellite Tracking (HL-SST), LL-SST and gravitational gradiometry, have been extensively investigated for their ability to improve specific properties of the static and time-varying part of Earth's gravity field. Analysis of the on-board sensor data led to assessment of their quality and estimation of their contribution to the gravity field error budget. Investigations concerning orbit design pointed out physical constraints caused by insufficient sampling. The aforementioned limitations constitute important lessons learnt from the dedicated gravity missions. These lessons, together with the needs and requirements of the scientific community, establish a solid background for mission design of NGGMs.

Main subject of this study is the gravity field processing of future LL-SST satellite missions. New generation instrument technology is expected to deliver measurements of substantially higher accuracy compared to the ones derived from current sensors. Key instrument of LL-SST missions is the inter-satellite ranging unit, which enables the detection of mass changes taking place below the satellites' orbital altitude. Laser interferometry is planned to substitute the K-Band Ranging (KBR) technology used so far in GRACE mission for the inter-satellite ranging. This will improve the measuring accuracy from μm to nm level, and raise potential for big improvements in terms of spatial resolution. However, this level of accuracy has to be contemplated with the noise levels from other error sources and limitations concerning processing accuracy. So far, gravity field processing accuracy has always been below the noise levels of observations. Advances in metrology of sensors such as the inter-satellite ranging instrument, may raise the demands for processing accuracy. In this study, we carefully address these

questions and propose solutions to the problems encountered.

The quantification of the contribution of all error sources to the error budget is a very important task for designing NGGMs. Comprehending the way each noise source propagates into the error spectrum, plays an important role for their effective treatment. In the frames of this study, we perform assessment of their contribution, and give special attention to the specific bandwidth part of the error spectrum each noise source is influencing. We develop methods for reducing the effect of error sources at the level of gravity field processing. Those methods are then applied for NGGMs of in-line GRACE-type formation, as well as for novel mission designs that constitute a constellation of satellites. It is also investigated, in which way the addition of a second pair of satellites improves the system's isotropy, and contributes to the reduction of temporal aliasing effects. The latter remains nevertheless one of the biggest contributors to the error budget of NGGMs. When using two pairs of satellites, temporal and spatial resolution are increased. That makes high frequency gravity field information taking place on large scales, easier to be retrieved. A further reduction of temporal aliasing effects is possible, when this information is taken into account and is properly assigned to the averaged solution. This leads to a gravity field approach with a wide spectrum of parameterization possibilities. This approach was implemented and investigated in this study, in the framework of a European Space Agency (ESA)-funded project with the name "Assessment of Satellite Constellations for Monitoring the Variations in Earth Gravity Field - SC4MGV" (Iran Pour et al., 2015). The spectrum of choices is explored and their effect is individually investigated. Possible relations between orbit design choices and the effectiveness of this method are also investigated, and recommendations on optimal parameterization choices are given. Finally, the relative improvements of solutions from such a NGGM compared to the state-of-the-art missions are discussed.

1.3 Outline

Chapter 2 gives the theoretical background for determining Earth's gravity field from satellite observations. It also presents the mission details of dedicated gravity satellite missions of the past and the present, and concludes by discussing concepts for future missions. Chapter 3 gives an overview of the simulation environment for the gravity field recovery. At first, the coordinate and time systems used are described. As a next step, the method for orbit simulation and the mathematical description of the functional model are presented. Finally, the formulation and solution of the system are described. Chapter 4 starts with an overview of the orbit designs for present and future gravity satellite missions. A brief discussion on science and mission requirements for future missions follows. Next, the noise models for the instrument performance used in the simulations are given, and results of closed-loop simulations for the error-budget analysis are presented. Chapter 5 reports the limitations when processing with standard accuracy, and investigates the use of enhanced accuracy in the gravity field processing chain. Chapter 6 presents the investigated methods of noise reduction, and analyzes their effect in gravity field processing at the presence of all noise sources. Chapter 7 deals with the treatment of temporal aliasing effects for NGGMs. Finally, Chapter 8 gives the conclusions of this study.

Chapter 2

Earth's gravity field determination from satellite observations

This chapter is dedicated to the description of the space methods that are used to determine features of the gravity field and the figure of the Earth. At first, the perturbing forces acting on a satellite are reviewed. As a next step, an overview of the dedicated gravity satellite missions of the past and the present is given. Finally, the state-of-the-art plans and challenges for NGGMs are presented.

2.1 Perturbing forces acting on a satellite

A near-earth artificial satellite flies around the Earth with an orbit that is slightly perturbed from its ideal Kepler motion. In case of a perturbed motion, the equation of motion takes the form of an inhomogeneous differential equation of second order:

$$\ddot{\mathbf{r}} + \frac{GM_E}{r^3}\mathbf{r} = d\ddot{\mathbf{r}}, \tag{2.1}$$

where G is the Newtonian gravitational constant, M_E is the Earth's total mass and $\mathbf{r}/r$ denotes a unit vector pointing from the center of the Earth to the satellite. For the analytical solution of Eq. (2.1), perturbation theory may be applied, where initially the homogeneous part of Eq. (2.1) is considered, leading to a Keplerian orbit. Each disturbing acceleration $d\ddot{\mathbf{r}}$ causes temporal variations in the orbital parameters that lead to an osculating ellipse which deviates from the Keplerian orbit. Those deviations are caused by perturbing forces that act on the satellite and are categorized into gravitational (or conservative) and non-gravitational (or non-conservative) forces. The gravitational forces are by far the strongest and mainly determine the satellite's orbit. They are induced by the gravitational attraction of the non-spherical part of Earth's gravity field and other celestial bodies (e.g. Sun, Moon and other planets) as well as tides (ocean, solid Earth, pole and third bodies). Non-gravitational forces include thrust forces, atmospheric drag, solar radiation pressure and Earth's reflected radiation (Earth albedo).

2.1.1 Earth's gravitational field

Newton's law of gravitation describes the attraction of two points with masses m_1 and m_2 separated by a distance l:

$$\mathbf{F} = G\frac{m_1 \cdot m_2}{l^2}, \tag{2.2}$$

where G is the Newtonian gravitational constant in Système International d'unités (SI) units:

$$G = 6.6743 \cdot \mathrm{m}^3\mathrm{kg}^{-1}\mathrm{s}^{-2}. \tag{2.3}$$

The gravitational field can be studied by calling one mass the attracting mass and the other the attracted mass. For simplicity the attracted mass is set equal to unity and the attracting mass is denoted by m. The gravitational force will then be equal to:

$$F = G\frac{m}{l^2}. \tag{2.4}$$

In geodesy we are considering the attraction of systems of point masses or of solid bodies. Thus it is easier to deal with a function such as the potential of gravitation, which is related to the force function in vector notation as

$$\mathbf{F} = grad(V) \tag{2.5}$$

Assuming that the point masses are distributed continuously over a volume υ with density ρ, the potential can be given by Newton's integral

$$V = G\iiint_{\upsilon}\frac{\rho}{l}d\upsilon \tag{2.6}$$

Outside the attracting masses, the density ρ is zero and the *Laplace equation* is satisfied:

$$\Delta V = 0 \tag{2.7}$$

where the symbol Δ is the so-called Laplacian operator. The solutions of Eq. (2.7) are called harmonic functions. Thus, the gravitational potential outside the Earth is also a harmonic function, whose solution is given by the sum of the surface spherical harmonics Y_n (Hofmann-Wellenhof and Moritz, 2006):

$$V = \sum_{n=0}^{\infty}\frac{Y_n(\theta,\lambda)}{r^{n+1}} \tag{2.8}$$

where r (radius vector), θ (polar distance) and λ (geocentric longitude) represent the spherical coordinates. The Laplace's differential equation for surface spherical harmonics has solutions given by the following functions:

$$Y^c_{nm}(\theta,\lambda) = P_{nm}(cos\theta)cosm\lambda \quad \text{and} \quad Y^s_{nm}(\theta,\lambda) = P_{nm}(cos\theta)sinm\lambda, \tag{2.9}$$

where $P_{nm}(cos\theta)$ is the *Legendre function*. Due to the linearity of those solutions, their combination will also be a solution that delivers the general expression for the surface spherical harmonics Y_n:

$$Y_n(\theta,\lambda) = \sum_{m=0}^{n} (a_{nm}cosm\lambda + b_{nm}cosm\lambda)P_{nm}(cos\theta) \tag{2.10}$$

where a_{nm} and b_{nm} are arbitrary constants. Substituting Eq. (2.10) to Eq. (2.8), the gravitational potential can be derived as an arbitrary function $f(\theta,\lambda)$ which is expanded into a series of surface spherical harmonics on the surface of the sphere:

$$f(\theta,\lambda) = V = \sum_{n=0}^{\infty} \frac{Y_n(\theta,\lambda)}{r^{n+1}} = \sum_{n=0}^{\infty} \frac{1}{r^{n+1}} \sum_{m=0}^{n} (a_{nm}cosm\lambda + b_{nm}cosm\lambda)P_{nm}(cos\theta), \tag{2.11}$$

Earth related applications benefit from the properties of spherical harmonics, when they are represented as an orthogonal set of solutions to the Laplace equation. The orthogonality property allows for a forward and inverse transform of a function to its spectrum. This is a reason why gravity field functionals are formulated in terms of spherical harmonic coefficients. Using the orthogonality properties of the functions included in (2.11):

$$\begin{aligned} \mathcal{R}_{nm} &= P_{nm}(cos\theta)cosm\lambda, \\ \mathcal{S}_{nm} &= P_{nm}(cos\theta)sinm\lambda, \end{aligned} \tag{2.12}$$

the equations for the constant coefficients a_{nm} and b_{nm} can be derived:

$$a_{n0} = \frac{2n+1}{4\pi} \iint_{\sigma} f(\theta,\lambda)P_n(cos\theta)d\sigma;$$

$$\left.\begin{aligned} a_{nm} &= \frac{2n+1}{2\pi}\frac{(n-m)!}{(n+m)!} \iint_{\sigma} f(\theta,\lambda)\mathcal{R}_{nm}(\theta,\lambda)d\sigma \\ b_{nm} &= \frac{2n+1}{2\pi}\frac{(n-m)!}{(n+m)!} \iint_{\sigma} f(\theta,\lambda)\mathcal{S}_{nm}(\theta,\lambda)d\sigma \end{aligned}\right\} \quad (m \neq 0). \tag{2.13}$$

In connection with satellite dynamics, Eq. (2.11) is often written in a form where the gravitational potential outside the Earth is expressed (Hofmann-Wellenhof and Moritz, 2006):

$$V(r,\theta,\lambda) = \frac{GM_E}{r}\left\{1 + \sum_{n=1}^{\infty}\sum_{m=0}^{n}\left(\frac{R_E}{r}\right)^n [C_{nm}\mathcal{R}_{nm}(\theta,\lambda) + S_{nm}\mathcal{S}_{nm}(\theta,\lambda)]\right\}, \tag{2.14}$$

where R_E is the mean equatorial radius of the Earth, so that it satisfies:

$$\left.\begin{aligned} C_{nm} &= \frac{1}{GMR_E^n} A_{nm} \\ S_{nm} &= \frac{1}{GMR_E^n} B_{nm} \end{aligned}\right\} \qquad (m \neq 0). \tag{2.15}$$

The A_{nm} and B_{nm} coefficients can be determined from the boundary values of gravity at the Earth's surface:

$$A_{n0} = G \iiint_{\text{earth}} r'^n P_n(cos\theta') dM;$$

$$\left.\begin{aligned} A_{nm} &= 2\frac{(n-m)!}{(n+m)!} G \iiint_{\text{earth}} r'^n \mathcal{R}_{nm}(\theta', \lambda') dM \\ B_{nm} &= 2\frac{(n-m)!}{(n+m)!} G \iiint_{\text{earth}} r'^n \mathcal{S}_{nm}(\theta', \lambda') dM \end{aligned}\right\} \qquad (m \neq 0), \tag{2.16}$$

where (r', θ', λ') are the spherical coordinates of a mass element dM inside Earth and (r, θ, λ) of a point at which the potential is to be determined. The conventional harmonics $\mathcal{R}_{nm}$ and $\mathcal{S}_{nm}$ can be replaced by other functions which are easier to handle, namely the *fully normalized* harmonics $\overline{\mathcal{R}}_{nm}$ and $\overline{\mathcal{S}}_{nm}$ given by (Hofmann-Wellenhof and Moritz, 2006):

$$\overline{\mathcal{R}}_{n0}(\theta, \lambda) = \sqrt{2n+1}\mathcal{R}_{n0}(\theta, \lambda) \equiv \sqrt{2n+1} P_n(cos\theta);$$

$$\left.\begin{aligned} \overline{\mathcal{R}}_{nm}(\theta, \lambda) &= \sqrt{2(2n+1)\frac{(n-m)!}{(n+m)!}} \mathcal{R}_{nm}(\theta, \lambda) \\ \overline{\mathcal{S}}_{nm}(\theta, \lambda) &= \sqrt{2(2n+1)\frac{(n-m)!}{(n+m)!}} \mathcal{S}_{nm}(\theta, \lambda) \end{aligned}\right\} \qquad (m \neq 0). \tag{2.17}$$

Similarly the corresponding fully normalized coefficients will be given by:

$$\overline{C}_{n0} = \frac{1}{\sqrt{2n+1}} C_{n0};$$

$$\left.\begin{aligned} \overline{C}_{nm} &= \sqrt{\frac{(n+m)!}{2(2n+1)(n-m)!}}\,C_{nm} \\ \overline{S}_{nm} &= \sqrt{\frac{(n+m)!}{2(2n+1)(n-m)!}}\,S_{nm} \end{aligned}\right\} \qquad (m \neq 0). \tag{2.18}$$

From a geometrical representation point of view, the spherical harmonics can be divided to zonal, tesseral and sectorial harmonics. Zonal are the harmonics with order equal to zero ($m = 0$), leading to an independence on longitude λ. The harmonics with equal degree and order ($m = n$) are called sectorial harmonics and do not depend on latitude ϕ. All other harmonics have $m \neq 0$ and $m \neq n$, are latitude and longitude dependent and are called tesseral harmonics. Zonal harmonics effect the satellite orbits to a much greater extent than tesseral harmonics, by influencing mostly the secular and long-periodic perturbations of the satellite's orbital elements a, e, i, e.t.c. Therefore, long observation periods with several satellite revolutions are needed in order to detect their influence in changes of orbital parameters. On the other hand, the perturbations due to tesseral harmonics lead to much shorter periods.

The very first spherical harmonic coefficients are of particular interest in geodesy. With Eq. (2.16) one can compute the zero-degree term A_{nm}:

$$A_{00} = G \iiint_{\text{Earth}} dM = GM_E, \tag{2.19}$$

which produces a zero-degree component of the geopotential V_{00} being nothing else than the gravitational potential of a point mass equal to the total mass of the Earth. Accordingly, the first-degree coefficients yield:

$$A_{10} = G \iiint_{\text{Earth}} z' dM, \quad A_{11} = G \iiint_{\text{Earth}} x' dM, \quad B_{11} = G \iiint_{\text{Earth}} y' dM. \tag{2.20}$$

Those three first-degree coefficients will be equal to zero if the origin of the used coordinate system coincides with the geocenter. In that case, the center of mass of the Earth coincides with the center of the Figure of the solid Earth. In general, LEO gravity field satellite missions such as the GRACE mission cannot provide accurate estimates of the geocenter motion since its effect cannot be separated from other parameters. As a result, the first-degree coefficients estimated from their measurements are of no value (Rietbroek et al., 2012).

Introducing the *moments of inertia* of the Earth with respect to the $x-$, $y-$, $z-$ axes

$$J_x = \iiint_{\text{Earth}} (y'^2 + z'^2) dM, \quad J_y = \iiint_{\text{Earth}} (z'^2 + x'^2) dM, \quad J_z = \iiint_{\text{Earth}} (x'^2 + y'^2) dM, \tag{2.21}$$

and the product of inertia of the Earth,

$$J_{xy} = \iiint_{\text{Earth}} x' y' dM, \quad J_{yz} = \iiint_{\text{Earth}} y' z' dM, \quad J_{xz} = \iiint_{\text{Earth}} z' x' dM, \tag{2.22}$$

we end up with the degree two coefficients (Hofmann-Wellenhof and Moritz, 2006):

$$A_{20} = G[(J_x + J_y)/2 - J_z], \quad A_{21} = GJ_{xz}, \quad A_{22} = \frac{1}{4}G(J_y - J_x)$$
$$B_{21} = GJ_{yz}, \quad B_{22} = \frac{1}{2}GJ_{xy}. \tag{2.23}$$

If the z axis of the coordinate system coincides with the Earth's principal axis of moment of inertia, J_{xz}, J_{yz} and consequently A_{21}, B_{21} will be equal to zero. Coefficient A_{20} is the largest perturbation term and is related to the ellipsoidal character of the Earth. It depends on the difference between the mean equatorial moment of inertia and that around the z axis, thus characterizing its flattening. Coefficient A_{22} is related to the difference in the moment of inertia with respect to the two axes in the equatorial plane, and thus it describes the equatorial non-symmetry of the mass distribution inside the Earth.

2.1.2 Direct tides (3^{rd} Body)

The satellite as well as the Earth itself are affected by gravitational forces of other celestial bodies, mainly the Sun and the Moon. The resulting force acting on the satellite is called direct tidal force. The acceleration of a satellite due to the attraction caused by a 3^{rd} body with a point mass M is given by:

$$\ddot{\mathbf{r}} = GM\left(\frac{\mathbf{s}-\mathbf{r}}{|\mathbf{s}-\mathbf{r}|^3} - \frac{\mathbf{s}}{|\mathbf{s}|^3}\right), \tag{2.24}$$

where $\mathbf{s}$ and $\mathbf{r}$ are the geocentric position vectors of the satellite and the celestial body respectively. For a typical Low Earth Orbiter (LEO) gravity satellite where the Sun and the Moon are far much further away from the Earth, the forces exerted from the Sun and the Moon are much smaller than the central attraction of the Earth. Therefore, for many applications the solar and lunar geocentric coordinates are not required to be known at the highest precision. Assuming an unperturbed motion of the Earth around the Sun, low-precision simplified equations for the solar and lunar coordinates are given by Montenbruck and Gill (2000).

2.1.3 Earth tides

Earth tides are a result of the attracting forces exerted by the gravitation of the Sun and the Moon, which lead to a time-varying deformation of the Earth. This deformation has an effect on the motion of the satellites. The Earth tides are categorized in solid Earth, ocean and pole tides, which are briefly discussed in the following section. For a more detailed description we refer to Petit and Luzum (2010).

Solid Earth tides

The Earth's solid body is elastic to first order. Thus, it responds to lunisolar gravitational attraction with small periodic deformations which are called solid Earth tides. Similarly to the Earth's static gravity field, spherical harmonics can be used to expand the solid Earth tidal-induced gravity potential that affect

the perturbed motion of the satellite. The time-dependent corrections to the unnormalized geopotential coefficients can be computed according to Sanchez (1975):

$$\begin{Bmatrix} \Delta C_{nm} \\ \Delta S_{nm} \end{Bmatrix} = 4k_n \left(\frac{GM}{GM_E}\right)\left(\frac{R_E}{R}\right)^{n+1} \sqrt{\frac{(n+2)(n-m)!^3}{(n+m)!^3}} P_{nm}(\sin\phi) \begin{Bmatrix} \cos(m\lambda) \\ \sin(m\lambda) \end{Bmatrix} (m \neq 0). \tag{2.25}$$

where M and R represent the mass and the geocentric distance of the Sun or the Moon, ϕ and λ their corresponding Earth-fixed latitude and longitude and k_n the Love numbers of degree n.

Ocean tides

The response of the oceans to the lunisolar gravitational attraction is known as ocean tides. It is another time-variable phenomenon occurring in the ocean and causing cyclic variations in the local sea level. This oceanic mass redistribution can be represented, as well as the solid Earth tides, by corrections of unnormalized geopotential coefficients (Montenbruck and Gill, 2000):

$$\begin{Bmatrix} \Delta C_{nm} \\ \Delta S_{nm} \end{Bmatrix} = \frac{4\pi G R_E^2 \rho_w}{GM_E} \frac{1+k_n'}{2n+1} \begin{Bmatrix} \sum\limits_{s(n,m)} (C_{snm}^+ + C_{snm}^- \cos\theta_s) + (S_{snm}^+ + S_{snm}^- \sin\theta_s) \\ \sum\limits_{s(n,m)} (S_{snm}^+ + S_{snm}^- \cos\theta_s) + (C_{snm}^+ + C_{snm}^- \sin\theta_s) \end{Bmatrix} (m \neq 0). \tag{2.26}$$

where ρ_w is the density of the seawater, k_n' are the load-deformation coefficients of degree n, $C_{snm}^{\pm}$ and $S_{snm}^{\pm}$ are the ocean tide coefficients in meters for the tide constituent s, θ_s is the weighted combination of the six *Doodson* variables. The Doodson variables are closely related to the arguments of the nutation series and principally denote the fundamental arguments of the Sun and Moon orbits.

Pole tides

Pole tides are caused by the contribution of the polar motion to the centrifugal potential due to Earth rotation. They affect mainly the geopotential coefficients C_{21} and S_{21} and can cause up to 25 mm tidal response in radial direction and 7 mm in horizontal direction (Petit and Luzum, 2010)

2.1.4 Non-gravitational forces

Atmospheric drag

Atmospheric drag is one of the largest non-gravitational perturbation forces that act on a LEO satellite and requires quite cumbersome calculations in order to be precisely modeled. The accurate modeling of aerodynamic forces is difficult due to the poor knowledge of the physical properties of the atmosphere (especially the density of its upper part). Moreover, a detailed knowledge of the interaction between neutral gas and charged particles with the different spacecraft surfaces is required. Finally, the time-

varying attitude of the satellite with respect to the atmospheric relative velocity has also to be taken into account.

Due to residual atmosphere, the satellite will experience atmospheric drag with a direction opposite to the velocity of its motion $\boldsymbol{\upsilon}_r$ (Montenbruck and Gill, 2000):

$$\ddot{\mathbf{r}} = -\frac{1}{2} C_D \frac{A}{m} \rho \upsilon_r^2 \mathbf{e}_\upsilon, \tag{2.27}$$

where m is satellite's mass, ρ is the atmospheric density at the location of the satellite, A is the satellite's cross-sectional area hit by a small mass element of an atmosphere column, $\mathbf{e}_\upsilon = \boldsymbol{\upsilon}_r / \upsilon_r$ is the unit vector of the relative velocity between satellite and atmosphere and C_D is a dimensionless quantity that describes the integrated interaction of the atmosphere with the material of the satellite's surface.

Solar radiation pressure and Earth Albedo

The radiation of the Sun exerts forces on a satellite by the absorption or reflection of photons. The acceleration due to the solar radiation depends on the satellite's mass and surface area. For a simplified case where the satellite's surface is perpendicular to the direction of the Sun this acceleration is given by (Montenbruck and Gill, 2000):

$$\ddot{\mathbf{r}} = -C_r P_s \frac{A}{m} (AU)^2 \frac{\mathbf{r} - \mathbf{r_s}}{|\mathbf{r} - \mathbf{r_s}|}, \tag{2.28}$$

where C_r is the radiation pressure coefficient, A and m are the area of the surface and the mass of the satellite respectively, AU is the length of one Astronomical Unit ($\approx 1.5 * 10^8 km$), P_s is the solar radiation pressure constant at 1 AU, $\mathbf{r}_s$ is the position vector of the Sun and $\mathbf{r}$ the position vector of the satellite. Eq. (2.28) is not precise enough for high-precision applications, such as geodetic space missions. In those cases, a detailed satellite structure together with its various surface properties has to be taken into account. An even more realistic modeling includes the use of shadow models for eclipse conditions, or Sun's occultation by Earth and Moon.

Earth reflects back radiation itself as a response to the solar radiation that it is receiving. The ratio between the reflected radiation and the incoming one is called *Earth albedo*. It comprises two components, the short-wavelength optical and the long-wavelength infrared radiation. The effect from both components decreases with increasing altitude. Typical amplitude values for the albedo accelerations sensed by LEO satellites reach up to 10% until 35% of the accelerations due to direct solar radiation pressure (Knocke et al., 1988).

2.2 Geopotential and its functionals

Any object located at the surface of the Earth will be subjected to both the gravitational force of the Earth $\vec{g_E}$ and the centrifugal force $\vec{g_C}$ due to Earth rotation. The sum of those two vectors $\vec{g}$ is the gravity vector

$$\vec{g} = \vec{g_E} + \vec{g_C}. \tag{2.29}$$

Objects located outside the Earth's surface will have equal $\vec{g}$ and $\vec{g_E}$ values. The corresponding potential functions of these forces are the geopotential W, the gravitational potential V and the centrifugal potential Ω

$$W = V + \Omega. \tag{2.30}$$

Let P be a point on the surface of the Earth with rectangular coordinates (x, y, z). The gradient of the geopotential W delivers the gravity vector $\vec{g}$ and its magnitude g at point P

$$\vec{g} = grad(W) = \begin{bmatrix} \frac{\partial W}{\partial x} \\ \frac{\partial W}{\partial y} \\ \frac{\partial W}{\partial z} \end{bmatrix}, \tag{2.31}$$

$$g = |\vec{g}| = \sqrt{\left(\frac{\partial W}{\partial x}\right)^2 + \left(\frac{\partial W}{\partial y}\right)^2 + \left(\frac{\partial W}{\partial z}\right)^2}. \tag{2.32}$$

An equipotential surface of the gravity field of the Earth can be implicitly defined as a surface with

$$W(x, y, z) = constant \tag{2.33}$$

One of the infinite equipotential surfaces around the Earth coincides approximately with the global mean sea level, and is known as the *geoid*.

Determination of the Earth's gravity field is facilitated by splitting it into a "normal" and a remaining small "disturbing" field. The normal gravity field has an equipotential surface of an ellipsoid of revolution, which is a second approximation of the figure of the Earth. The potential of the normal gravity field is called normal potential U and its gravity magnitude normal gravity γ. The difference between the geopotential W and the normal potential U is the disturbing potential T

$$T = W - U \tag{2.34}$$

Let P and Q be two points on the same ellipsoidal normal such that the geopotential W_P of the point P laying on the geoid is equal to the normal potential U_P of point Q laying on the ellipsoid. The difference

$$\Delta g_P = g_P - \gamma_Q, \tag{2.35}$$

is called the *gravity anomaly* at point P. The difference between the gravity value at a point P and the normal gravity value at the same point is called *gravity disturbance*

$$\delta g_P = g_P - \gamma_P. \tag{2.36}$$

The distance along the ellipsoidal normal between a point P on the geoid and point Q on the ellipsoid is

called *geoid height* or *geoid undulation*. It can be related to the disturbing potential with *Bruns formula*:

$$N = \frac{T}{\gamma} \tag{2.37}$$

It is usually assumed that there are no masses outside the geoid and that the gravity observations refer directly to the geoid. In that case, the density ρ is zero everywhere outside the geoid. Therefore, the disturbing potential T is harmonic there and satisfies the Laplace equation (2.7). Moreover, assuming a sphere instead of a reference ellipsoid for the equations of the quantities T, Δg, δg and N leads to a tolerable error due to approximation, since these quantities are small. Therefore, the following equations are derived (Hofmann-Wellenhof and Moritz, 2006):

$$\Delta g = -\frac{\partial T}{\partial r} - \frac{2}{r}T, \tag{2.38}$$

$$\delta g = -\frac{\partial T}{\partial r}, \tag{2.39}$$

where r is the geocentric distance of a point outside the Earth. The quantities T, Δg, δg and N can also be expressed in spherical harmonics:

$$T(r,\theta,\lambda) = \frac{GM_E}{R_E}\sum_{n=2}^{\infty}\left(\frac{R_E}{r}\right)^{n+1}\sum_{m=0}^{n}\left[\overline{C}'_{nm}\mathcal{R}_{nm}(\theta,\lambda) + \overline{S}_{nm}\mathcal{S}_{nm}(\theta,\lambda)\right], \tag{2.40}$$

$$\Delta g(r,\theta,\lambda) = \frac{GM_E}{{R_E}^2}\sum_{n=2}^{\infty}(n-1)\left(\frac{R_E}{r}\right)^{n+2}\sum_{m=0}^{n}\left[\overline{C}'_{nm}\mathcal{R}_{nm}(\theta,\lambda) + \overline{S}_{nm}\mathcal{S}_{nm}(\theta,\lambda)\right], \tag{2.41}$$

$$\delta g(r,\theta,\lambda) = \frac{GM_E}{{R_E}^2}\sum_{n=2}^{\infty}(n+1)\left(\frac{R_E}{r}\right)^{n+2}\sum_{m=0}^{n}\left[\overline{C}'_{nm}\mathcal{R}_{nm}(\theta,\lambda) + \overline{S}_{nm}\mathcal{S}_{nm}(\theta,\lambda)\right], \tag{2.42}$$

$$N(r,\theta,\lambda) = \frac{GM_E}{R_E\gamma}\sum_{n=2}^{\infty}\left(\frac{R_E}{r}\right)^{n+1}\sum_{m=0}^{n}\left[\overline{C}'_{nm}\mathcal{R}_{nm}(\theta,\lambda) + \overline{S}_{nm}\mathcal{S}_{nm}(\theta,\lambda)\right], \tag{2.43}$$

where $\overline{C}'_{nm} = \overline{C}_{nm} - \overline{C}^{ell}_{nm}$, are the differences of the geopotential coefficients to the reference normal potential coefficients. The above equations assume $\overline{C}_{00} = \overline{C}^{ell}_{00}$, which is the case when the chosen reference parameters GM_E and R_E are close to the true values. It is also assumed that the origin of the coordinate system is located in the center of mass of the Earth, which results in $\overline{C}'_{1m} = \overline{S}'_{1m} = 0$.

The summations at Eqs. (2.14) are normally truncated to a certain degree $n = n_{max}$. The maximum degree $n = n_{max}$ correlates to the spatial resolution at the Earth surface by:

$$\lambda_{min} \approx 40000km/2l_{max}, \tag{2.44}$$

where λ_{min} is the minimum wavelength (or half wavelength resolution) of the gravity field features that are resolved by the $(l_{max}+1)^2$ parameters of the spherical harmonic coefficients $\overline{C}_{nm}, \overline{S}_{nm}$. The average

signal amplitude per degree n of a spherical harmonic coefficient can be expressed by "Kaula's rule of thumb":

$$\sigma_n \approx \sqrt{(2n+1)\frac{10^{-10}}{n^4}}. \tag{2.45}$$

The power of the gravity potential signal at degree n of the spherical harmonic expansion can be expressed by the Signal Degree Amplitude (SDA) (Ilk et al., 2005):

$$SDA_n = \sqrt{\sum_{m=0}^{n}\left(\overline{C}_{nm}^2 + \overline{S}_{nm}^2\right)}. \tag{2.46}$$

Two different gravity field models a and b can be compared degree-wise with use of the Difference Degree Amplitude (DDA) (Ilk et al., 2005):

$$DDA_n = \sqrt{\sum_{m=0}^{n}\left(\Delta\overline{C}_{nm}^2 + \Delta\overline{S}_{nm}^2\right)}, \tag{2.47}$$

with $\Delta\overline{C}_{nm} = \overline{C}_{b,nm} - \overline{C}_{a,nm}$ and $\Delta\overline{S}_{nm} = \overline{S}_{b,nm} - \overline{S}_{a,nm}$. The formal error of a gravity field model can also be represented degree-wise as a function of the formal errors of the spherical harmonic coefficients $\sigma_{\overline{C}_{nm}}$ and $\sigma_{\overline{S}_{nm}}$ by the Error Degree Amplitude (EDA) and the Cummulative Error Degree Amplitude (CEDA):

$$EDA_n = \sqrt{\sum_{m=0}^{n}\left(\sigma_{\overline{C}_{nm}}^2 + \sigma_{\overline{S}_{nm}}^2\right)}. \tag{2.48}$$

$$CEDA_n = \sqrt{\sum_{i=2}^{n}\sum_{m=0}^{n}\left(\sigma_{\overline{C}_{im}}^2 + \sigma_{\overline{S}_{im}}^2\right)}. \tag{2.49}$$

2.3 Dedicated gravity satellite missions

The accurate determination of the gravity field of the Earth has been a subject of many satellite missions throughout the years. Even since the launch of Sputnik 1 in 1957, its orbit data such as optical observations, laser tracking and Doppler tracking data, have been used for estimation of Earth gravity field models (Vetter et al., 1993). With the operation of the GPS in the 1990's the HL-SST method began to be used, by tracking between the GPS satellite and a LEO satellite. However, due to signal attenuation with height, those methods did not provide enough information on the short wavelength gravity signals and the improvement was limited to the long and medium wavelength part. In order to meet the demands for an accurate determination of Earth's gravity field, dedicated satellite gravity missions had to be considered and designed.

2.3.1 The CHAMP mission

The CHAMP (Reigber, 1995) was the first LEO dedicated geopotential satellite mission with geoscientific and atmospheric research objectives, to carry a GPS receiver in space. It operated for 10 years (from 2000 until 2010) and was initiated by the Deutsches Geoforschungszentrum (GFZ) and managed by the Deutsches Zentrum für Luft und Raumfahrt (DLR). Its primary objective was to collect simultaneously highly precise gravity and magnetic field measurements. The main observables were the HL-SST observations from the GPS satellites to the CHAMP satellite. Along with the GPS receiver, the CHAMP satellite contained also an accelerometer for measuring the sum of the non-gravitational forces acting on the satellite, and a star tracker which provided the orientation of the satellite in space. CHAMP data initially aimed to map the Earth's global long to medium wavelength gravity field, but have also been successfully used for the retrieval of its low frequency temporal variations. In Prange (2010) the Earth's static gravity field is resolved up to a maximum degree $n_{max} = 106$ and the largest seasonal variations such as trends ($n_{max} = 10$) are also estimated.

2.3.2 The GRACE mission

The GRACE mission launched in March 2002 is a dedicated twin-satellite gravity mission between the National Aueronautics and Space Administration (NASA) and DLR, with a main objective to monitor the time-variable gravity field of the Earth (Tapley et al., 2004). Main focus of the GRACE mission is to quantify the on-going mass redistributions near the Earth's surface that related to geophysical and climatologically driven processes. Since its launch, it has provided the user community with observation time series that are of great value for a wide spectrum of the Earth system related applications. The estimation of mass changes due to the continental water cycle from GRACE fields has been very successful (Tapley et al., 2004; Lambert et al., 2013; Wouters et al., 2011; Ramillien et al., 2011). GRACE gravity field solutions have also been extensively used for estimation of ice sheet mass loss at Antarctica (Luthcke et al., 2013; Chen et al., 2011; Schrama and Wouters, 2011) and Greenland (Velicogna and Wahr, 2013), as well as GIA for this region (Riva et al., 2009). Moreover, GRACE is even able to detect the gravity changes due to mega earthquakes (magnitude $M > 8.5$) and contribute to the estimation of co- and post-seismic effects (Han et al., 2006; Einarsson et al., 2010). GRACE data have been successfully used for the estimation of polar motion excitation (Jin et al., 2010).

The GRACE mission consists of two identical satellites that orbit one behind the other in the same orbital plane at a distance of 220km. The GRACE satellites are similar in construction as the CHAMP satellite except for the boom with the magnetic field instruments, and they represent free falling proof-masses in the Earth's gravity field. However, the GRACE mission is the first one to employ the satellite-to-satellite concept in the low-low mode (LL-SST). Following this measuring concept (Fig. 2.3.1), the inter-satellite separation (range) of the two satellites and the its change over time (range-rate), allows for the recovery of the global gravity field down to spatial scales of a few hundred kilometers with a temporal resolution of monthly or even sub-monthly intervals.

The distance variation is measured by the KBR instrument, that provides dual one-way range observations by means of microwave radio link transmission in two frequencies in the K/Ka-band. The KBR instrument is able to measure the range between the satellites with an accuracy of about $10\mu m$ and the corresponding range-rate with $1\mu m/sec$. Along with the KBR instrument, each GRACE satellite carries a GPS receiver, a cold gas propulsion system, three magnetic torque rods, a three-axis magnetometer, a three-axis Inertial Measurement Unit (IMU) for measuring the angular rates, star tracker cameras and an accelerometer. The star tracker cameras provide the precise orientation (attitude) of each satellite with respect to the stars. The GPS receiver serves for the precise orbit determination of the GRACE satellites and provides data for atmospheric and ionospheric profiling. The GPS data are also needed for calibrating the accelerometers. The GPS measurements through the HL-SST principle, contribute mainly to the estimation of the low degrees of the gravity field. The accelerometer is responsible for measuring all the non-gravitational forces that act on the satellite.

Gravity field estimates from the GRACE mission are provided by several groups, which apply different processing strategies and tuning parameters that result in solutions with regionally specific variations and error patterns. Fig. 2.3.2 depicts the CEDA values for solutions provided from the GFZ and visualizes the progress that is achieved from release 04 to release 05. Overall, a mm internal accuracy in terms of geoid height undulations can be achieved at a spatial resolution of 350 km half wavelength.

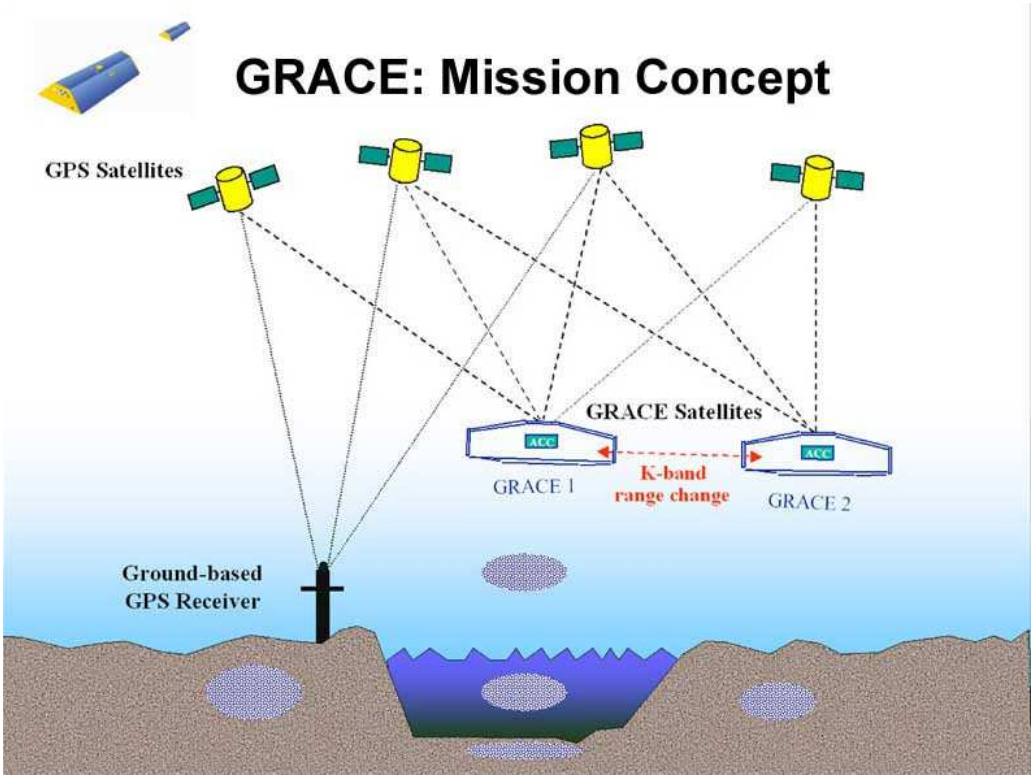

Figure 2.3.1: GRACE mission measuring concept (Courtesy of CSR/TSGC, retrieved 28 May 2015, from http://www.csr.utexas.edu/grace/publications/presentations/HPC2001.html)

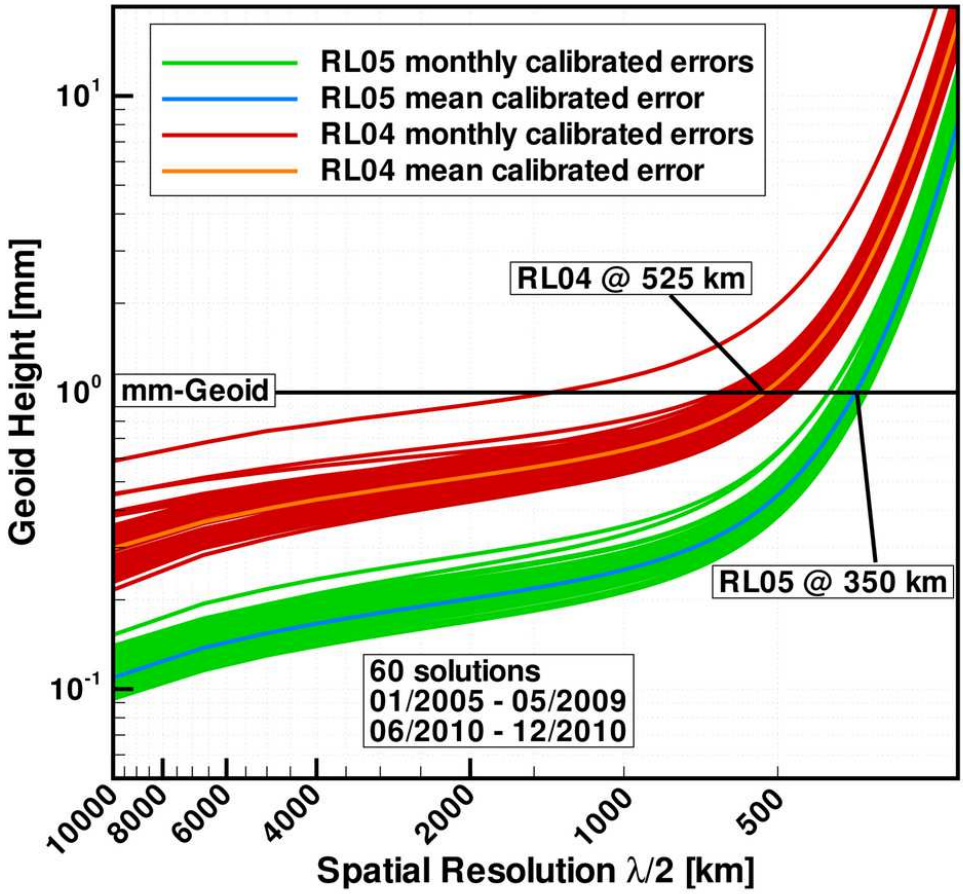

Figure 2.3.2: CEDA values for the monthly GFZ RL04 and RL05 solutions in terms of geoid height undulations (Courtesy of GFZ potsdam, retrieved 28 May 2015, from http://www.gfz-potsdam.de/sektion/globales-geomonitoring-und-schwerefeld/themen/entwicklung-betrieb-und-auswertung-von-schwerefeld-satellitenmissionen/grace/schwerefeldergebnisse/grace-gfz-rl05/)

2.3.3 The GOCE mission

The GOCE mission was launched on 17^{th} of March 2009 by the ESA as the first Earth Explorer mission. GOCE completed its mission after nearly trippling its lifetime and re-entered the atmosphere on 11^{th} of November 2013. Its primary objective was the survey of Earth's static gravity field with a global mean accuracy of 1 mGal in terms of gravity anomalies. Eventually, GOCE data contributed to the estimation of a high resolution map of Earth's gravity field reaching accuracies of 2.4 cm at a spatial scale of 100 km outside the polar regions (Brockmann et al., 2014). The spacecraft operated at a very low orbital altitude of under 270 km which, late in the mission, was lowered further to 224 km. The satellite was equipped with active drag compensation and angular control, in order to maintain its low orbit altitude on one hand, and to compensate for the effect of all non-gravitational forces acting on it, on the other. GOCE's core and unique measurement instrument is a three-axis gradiometer based on three pairs of electrostatic

servo-controlled accelerometers. The gradiometer measures acceleration differences along baselines of 0.5 m in the Gradiometer Reference Frame (GRF) (Rummel et al., 2011). These measurements are reduced by centrifugal and angular acceleration terms and are properly calibrated before they serve as the second derivatives of the Earth's gravitational potential in the GRF.

2.4 Concepts for future satellite gravity missions

The recent dedicated satellite gravity missions described in sec. 2.3 have successfully monitored precisely the static and temporal part of Earth's gravity field. Especially with the GRACE mission, more than a decade-long continuous series of space-based observations of changes in the Earth's gravity field, from global down to regional spatial scales on time scales even of one week, demonstrated the importance of such missions for monitoring key climate indicators such as ice-sheet mass balance, the total water cycle and other mass transport processes. Their global view of mass transport provides a unique framework for the coherent interference between results from other missions observing Earth subsystems.

On the way to meet the scientific challenges, future satellite gravity missions should aim to overcome the shortcomings of their predecessors. Designing concepts for future satellite gravity missions is closely related to setting the goals to be achieved in the short, medium and long term. The short-term goals, which receive the highest priority, include:

- Continuation of the observation time series

The medium-to-long term goals include:

- Increase of the spatial resolution
- Increase of the temporal resolution
- Providing complementary observations and products

The means to achieve the short-term goal is the launch of missions such as the GRACE-FO mission, in order to maintain uninterrupted time series of measurements. The means to achieve the medium-to-long term goals include:

- Increase of the integrated sensors' accuracy
- Improvement of the supporting platforms (e.g. active compensation of drag forces)
- Usage of novel measurement principles
- Enabling complex Satellite Formation Flights (SFFs) with use of multiple satellite pairs, or even satellite constellations

2.4.1 The GRACE Follow-On mission

Among the scientific user community, it is generally agreed that one of the most valuable aspects for an integrated monitoring of the system Earth is the availability of a continuous and uninterrupted time series. In order to continue the record of climate change observations after the end of the GRACE mission, NASA and GFZ approved the launch of a successor mission simply called GRACE-FO. The mission is intended to act as a bridge connecting the original GRACE mission to the future Next Generation Gravity Missions (NGGMs).

The launch of GRACE-FO is scheduled for August 2017 (Flechtner et al., 2014a) and the setup will again consist of a pair of twin satellites which are based on GRACE and Swarm (Friis-Christensen et al., 2008) heritage. The instruments are slightly modified compared to those used in GRACE. The star cameras have an improved configuration, the IMU is more reliable, the thermal control is improved and the KBR instrument has been modernized based on heritage from the Gravity Recovery and Interior Laboratory (GRAIL) mission. As secondary objective, GRACE-FO will carry a Laser Ranging Interferometer (LRI) in order to demonstrate its effectiveness in improving the LL-SST measurement performance, which is directly linked to the accuracy of the gravity field models. The LRI design is based on the so called "race track configuration"(Sheard et al., 2012) and the minimum operation time is set to one year. The LRI will be operated in parallel with the microwave ranging instrument, and the goal is to increase the LL-SST inter-satellite measurement accuracy by a factor of 1000 compared to the KBR measurements from GRACE.

2.4.2 Next Generation Gravity Missions (NGGMs)

CHAMP was the first dedicated geopotential satellite mission to deliver precise gravity field models for the long and medium wavelengths. GRACE was a major step forward compared to CHAMP, and over the years, the gravity field processing centers improved their processing schemes and delivered much more accurate solutions. However, there are still limitations and shortcomings that cannot be overcome with the technology used for the GRACE or even GRACE-FO mission. Limitations posed from the measuring instruments are expected to be, up to a certain extent, overcome in the future. For example, the usage of laser interferometry for the basic measuring instrument of the inter-satellite distance, metrology improvements at the design of the accelerometers and the star cameras and usage of an improved drag control system, will all contribute to a general enhancement of the accuracy of the gravity field generation. However, a typical GRACE SFF is based on an architecture consisting of a master-slave formation with co-planar orbits. This concept provides the difference of the first derivatives of the gravitational potential between the two satellites, but it is sensitive only in the along-track direction. Since the GRACE orbits are nearly polar, sampling at the along-track direction is almost always parallel to the direction North-South. That allows for minor information for the gravitational forces to be gathered in the radial and cross-track directions, and introduces anisotropy to the system. Also connected to sampling, another limiting error source for in-line LL-SST missions like GRACE and GRACE-FO is the temporal aliasing

caused by under-sampling signal of interest and by errors in the background models for atmosphere, ocean and ocean tide models (Zenner et al., 2012; Han et al., 2004). Temporal aliasing is one of the major error sources of the GRACE mission and results into a distinguishable error pattern of longitudial striping in the gravity field solutions. The aforementioned shortcomings set the challenges for the NGGMs to be taken up. The current strategies for designing NGGM missions are discussed in detail in sec. 4.

Chapter 3

Description of the simulation environment for the gravity field recovery

This section is devoted to the description of the simulation environment for the gravity field recovery, including the formulation of the mathematical model used for the gravity field retrieval, as well as all the details concerning the gravity field processing procedure.

3.1 Outline of the simulation environment

For the purposes of this study, a simulation environment for full-scale LL-SST gravity field processing was developed (Daras et al., 2014), based on the software available at the Lehrstuhl für Astronomische und Physikalische Geodäsie (APG) used for processing of real GOCE data (Yi, 2012). The simulation software (or else simulator) is a collection of Fortran subroutines that contains all the necessary processing steps needed for a full-scale gravity field simulation retrieval, including the generation of the dynamic orbits and of the pseudo-observations, the setting up of the Normal Equation (NEQ) system and the solution of the system with the method of Least Squares Adjustment (LSA). The flowchart of the gravity field simulation is given in Fig. 3.1. The simulation scheme is divided into three major processing steps: the orbit simulation part, the setup of NEQs part and the solution of the NEQs. All simulations are performed at the Linux cluster of the supercomputing center of the Leibniz Rechnenzentrum (LRZ). Whereas most of the processing is performed in a serial manner, the part of assembling the NEQs (which is the core of the processing scheme) exploits the benefit of parallel processing. At a higher level, the setup of NEQs is autonomously processed at a daily basis, occupying one node for each day. By this, all days can be processed simultaneously, as long as there are enough nodes available at the cluster. At the end of the processing, the NEQs are stored and are ready to be accumulated in the next step (sec. 3.6.3). At a lower level, the setup of NEQs part itself is programmed by use of the Open Multi-Processing (OpenMP) interface, a compiler extension that allows to add parallelism into the source code via multithreading.

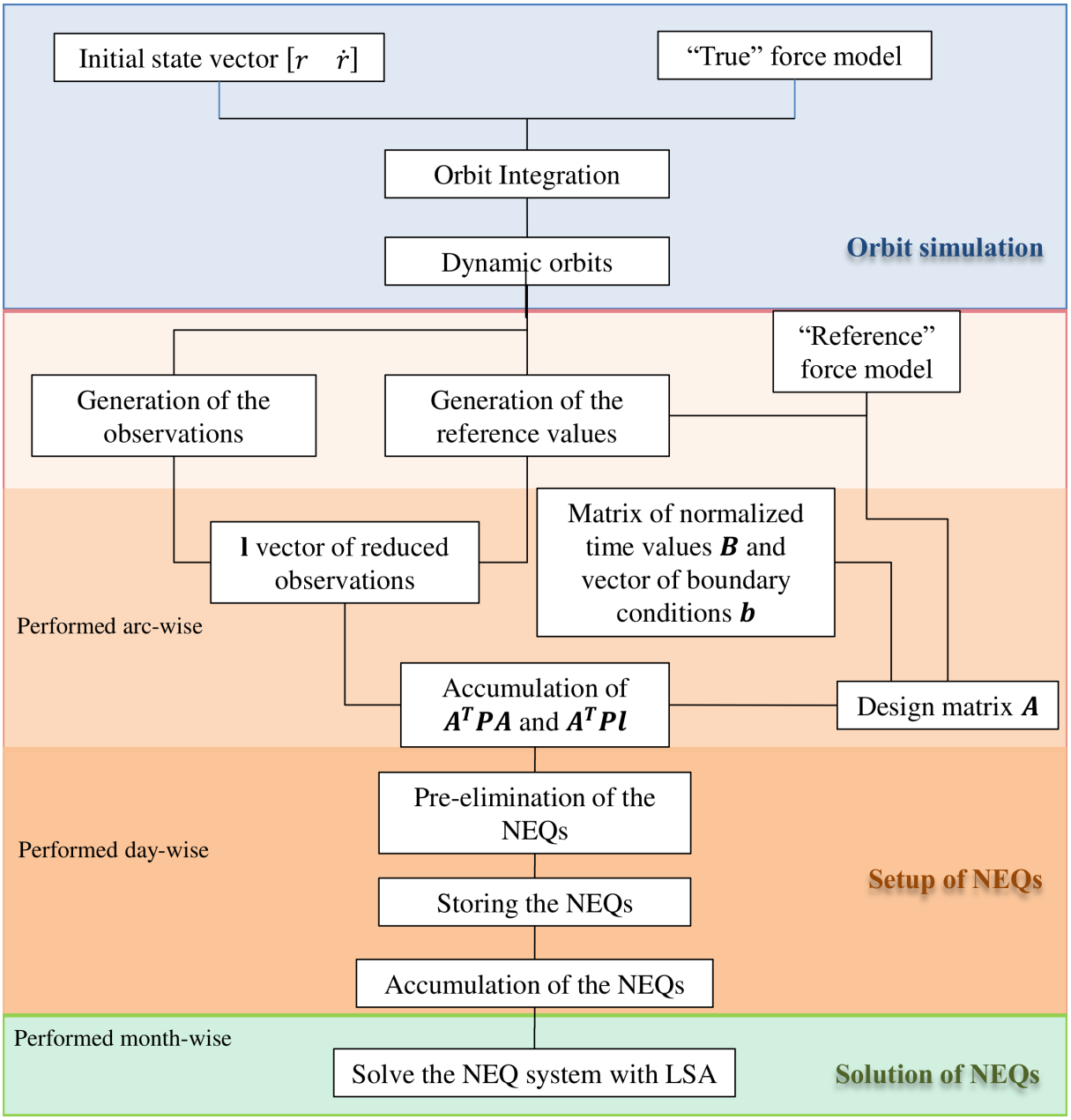

Figure 3.1.1: Gravity field simulation flowchart

Real gravity field processing of a LL-SST-type mission, makes use of observations from the satellite measuring units that are provided after a so-called Level-1 (L1) processing. Products from real observations such as GPS kinematic satellite orbits, inter-satellite ranges, non-gravitational accelerations sensed by the accelerometers and star camera orientation data are not available in a simulation environment. Thus, in order to simulate the Earth-system realistically, these observations have to be simulated, or their effect has to be taken into account. The observations needed for the HL-SST and the LL-SST part of the functional model are directly derived from the simulated dynamic orbits as described in Sec. 3.4.

Let us call them pseudo-observations. The measurements of non-gravitational accelerations sensed by the accelerometers and the star camera orientation data are not simulated explicitly. However, they are implicitly considered in the gravity field processing, by taking into account the imperfection of their sensors (sec. 4).

3.2 Coordinate and time systems

Geodetic applications require reference frames as a basis for three-dimensional, time-dependent positioning in global, regional and national geodetic networks. Reference frames are realizations of reference systems, which define the coordinate system and datum in which all landmarks have unique coordinates. The time systems in which the time variability of phenomena is expressed, are categorized based on various periodic processes such as Earth rotation, Earth revolution and atomic oscillations.

Conventional Celestial Reference System

The motion of the Earth-orbiting satellites is usually described in a coordinate system called (conventional) Celestial Reference System (CRS), with its practical realization being the (conventional) Celestial Reference Frame (CRF). It is also called geocentric quasi-inertial system, due to the accelerated motion of the Earth around the Sun. The system's origin is located at the center of mass of the Earth. The X_1^0-axis points towards the vernal equinox (on the line where the equatorial and the ecliptic plane intersect), the X_3^0-axis is identical to the position of the angular momentum axis at the reference epoch January $1,2000,0^h,0^{min},0^{sec}$ (J2000.0) and the X_2^0-axis is orthogonal to the X_1^0-axis and the X_3^0-axis in such a way that it completes a right-handed system. The numerical integration of the equations of motion used to simulate the dynamic orbits in this study (sec 3.3) is performed in the CRF.

Conventional Terrestrial Reference System

Satellite observations obtained from an observing site on the surface of the Earth cannot refer to a reference system such as the CRS which moves with the center of the Earth but is free of rotation. The locations on or within the Earth are best described with the (conventional) Terrestrial Reference System (TRS), with its practical realization being the (conventional) Terrestrial Reference Frame (TRF). For example, the specific forces acting on a satellite which are induced by the Earth's gravity field, require geolocation provided at the TRS. The TRS is also called Earth-fixed coordinate system and its origin is located at the center of mass of the Earth. The X_3-axis is identical to the mean position of the Earth's rotational axis as defined by the Conventional International Origin (CIO). The X_1-axis points to the intersection of the International Earth Rotation Service (IERS) Reference Meridian (IRM), which is close to the Greenwich meridian, while the X_2-axis is orthogonal to the X_1-axis and the X_3-axis and completes the right-handed system.

The transformation between the CRF and the TRF is achieved by means of the following subsequent rotations (Hofmann-Wellenhof et al., 2001):

$$\mathbf{r}_T = \mathbf{R}_M \mathbf{R}_S \mathbf{R}_N \mathbf{R}_P \mathbf{r}_C, \tag{3.1}$$

where

$\mathbf{r}_T$ ... vector in the TRF
$\mathbf{r}_C$ ... vector in the CRF
$\mathbf{R}_M$ ... rotation matrix for polar motion
$\mathbf{R}_S$ ... rotation matrix for sidereal time
$\mathbf{R}_N$ ... rotation matrix for nutation
$\mathbf{R}_P$ ... rotation matrix for precession

The estimation of the nutation and precession matrices, as well as of the Greenwich sidereal time is performed by the simulator using the Standards Of Fundamental Astronomy (SOFA) software package (Board, 2015), which follows the International Astronomical Union (IAU) conventions. The Earth Orientation Parameters (EOP) used were taken from the IERS (EOP 08 C04), where the precession and nutation parameters are related to the IAU 2006/2000A model.

Satellite-fixed Reference System

The satellite's own local reference frame has its origin at the satellite's center of mass. The realization of such a reference frame includes a X^S-axis which coincides with the satellite's velocity vector for a circular orbit and points towards the "along-track"direction, a X^R-axis which points in radial direction away from the satellite's body and a X^W-axis which is normal to the orbital plane and therefore called "out-of-plane"or "cross-track"axis. The satellite-fixed reference frame is a co-moving frame, which is particularly suited to describe non-gravitational perturbation accelerations, sensor biases and thrust components. The transformation from the satellite-fixed to the quasi-inertial reference frame is achieved by use of the transformation matrix $\mathbf{E}$:

$$\mathbf{E} = \begin{bmatrix} \mathbf{e_r} \\ \mathbf{e_w} \\ \mathbf{e_s} \end{bmatrix}, \tag{3.2}$$

where $\mathbf{e_r}$, $\mathbf{e_w}$, $\mathbf{e_s}$ are the unit vectors at the CRF:

$$\begin{aligned} \mathbf{e_r} &= \frac{\mathbf{r}(t)}{|\mathbf{r}(t)|}, \\ \mathbf{e_w} &= \frac{\mathbf{r}(t) \times \dot{\mathbf{r}}(t)}{|\mathbf{r}(t) \times \dot{\mathbf{r}}(t)|}, \\ \mathbf{e_s} &= \mathbf{e}_w \times \mathbf{e}_r. \end{aligned} \tag{3.3}$$

Time systems

The time system used to define the satellite's motion at the TRF, is the GPS time system, which is nominally related to the International Atomic Time (IAT) by:

$$t_{GPS} = t_{IAT} - 19.^s000, \tag{3.4}$$

where IAT is defined as the weighted average of the time kept by over 400 atomic clocks in over 50 laboratories around the world. The Terrestrial Time (TT) is the dynamic time that replaced the term Ephemeris Time and Terrestrial Dynamic Time used in the past. It is related to the IAT by:

$$t_{TT} = t_{IAT} + 32.^s184, \tag{3.5}$$

The Julian Date (JD) is defined by the number of mean solar days elapsed since the epoch 4713 B.C., January $1.^d5$. The Modified Julian Date (MJD) is obtained by subtracting 2400000.5 days from the JD, which refers to 2000 January $1.^d5$ (or else J2000.0). Moreover, the timespan expressed in Julian centuries of 36525 mean solar days between the epoch J2000.0 and a random epoch of observation, defines the parameter T which is used at the estimation of the precession parameters needed in Eq. (3.1). The Universal Time (UT) is a time standard that is the theoretical basis for all civil time-keeping. It is defined as the Greenwich hour angle augmented by 12 hours of a fictional Sun that uniformly orbits in the equatorial plane (Hofmann-Wellenhof et al., 2001). A version of the UT is the UT1, which includes an additional correction for the polar motion. The Universal Time Coordinated (UTC) is also one version of UT that coincides with the GPS standard epoch 1980, January $6.^d0$ and is related to the IAT by:

$$t_{UTC} = t_{IAT} - 1.^s000n, \tag{3.6}$$

with the integer n being the leap second that is reported by the IERS in the following way: when the time-dependent difference $dUT1 = UT1 - UTC$ provided by IERS becomes larger than $0.^s9$, a leap second is inserted into the UTC system. For example, in June 2000 the integer value was $n = 32$. The time series of the IERS EOPs used at the estimation of the transformation matrix $\mathbf{r}_T$ in Eq. (3.1), are provided in the UTC system.

3.3 Simulation of the satellite orbits

The approach of gravity field processing used in this study (sec. 3.4) requires GPS kinematic orbits to be used in a conventional tracking analysis as observations of satellite positions. For simulation purposes, dynamic orbits have been simulated and used instead. Dynamic satellite orbits are computed by use of a set of initial state vectors (position and velocity of the satellite) and a force model, which allows for continuous computation of the satellite's state vector. The initial state vector defines a solution of the satellite's equation of motion (Eq. (2.1)) at an initial epoch t_0 and refers to the satellite's center of mass

in the CRF. The numerical integration of the equation of motion starting from the initial state vector, provides the position and velocity vector of the satellite at every subsequent epoch t. Kaula (Kaula, 1966) was the first to express the Earth's disturbing potential as a harmonic function of the Keplerian parameters $(\Omega, i, \omega, \alpha, e, T_0)$. However, the high accuracy that is nowadays required for the computation of satellite orbits can only be achieved through the use of numerical methods for the solution of the equation of motion (Montenbruck and Gill, 2000).

The orbit integrator used in this study follows a multistep method for the numerical integration according to Shampine and Gordon (1975), which applies a modified divided difference form of the Adams Predict-Evaluate-Correct-Evaluate (PECE) formulas and local extrapolation. According to this method, the order and the step size are adjusted to control the local error per unit step in a generalized sense. For detailed information refer to Yi (2012). The local error thresholds denote the accuracy of the orbit and are selected by the user. They can reach up to 10^{-8}m in an absolute and 10^{-15}m in a relative sense when applying standard double precision processing. The dynamic orbits are generated at the first part of the gravity field simulation scheme, namely the "Orbit simulation"part (Fig. 3.1).

The usage of the dynamic orbits in a simulation environment is threefold:

- serving as computational points for the reference values of the observations (geolocation),
- explicitly computing the HL-SST and LL-SST reference values,
- implicitly computing the HL-SST and LL-SST pseudo-observations.

3.4 Functional model

The approach used for gravity field recovery is based on the integral equation approach (Schneider, 1969) which was later refined by Mayer-Gürr (2006) and named short-arc approach. It has already been successfully applied in real data applications to recover satellite-only gravitational field models for CHAMP, GRACE (Mayer-Gürr, 2006) and for GOCE (Yi, 2012; Schall et al., 2014). According to this approach, the computation of a satellite's orbit can be formulated as a boundary value problem in the form of a Fredholm-type 2 integral equation. The orbit is divided into short arcs and the gravity field coefficients are parametrized together with the boundary point values of each arc. The simulator uses a modification proposed by Yi (2012) which guarantees the continuity of the orbit by setting up the position vectors at the node points as unknown parameters and estimating them together with the gravity field model (Sec. 3.6.1). It is therefore directly based on the orbit positions and does not require solving variational equations, thus avoiding numerical errors due to differentiation.

The mathematical model implies a relationship between the orbit positions inside the arc and those at the boundary points, as well as the parameters of the force model to be estimated. The equations of motion in terms of the position of a satellite flying between the boundary points A and B of a short arc,

have the form of a Fredholm integral equation of a second kind (Mayer-Gürr, 2006):

$$\mathbf{r}(\tau) = \mathbf{r}_A(1-\tau) + \mathbf{r}_B\tau - T^2\int_0^1 K(\tau,\tau')\mathbf{f}(\mathbf{r}(\tau'))d\tau', \tag{3.7}$$

where K is a continuous kernel function (Schneider, 1969):

$$K(\tau,\tau') = \begin{cases} \tau'(1-\tau) & \text{for } \tau \le \tau' \\ \tau(1-\tau') & \text{for } \tau' > \tau \end{cases}, \tag{3.8}$$

$\mathbf{r}_A$ and $\mathbf{r}_B$ are the position vectors of the satellite at the beginning and the end of the arc respectively, $T = t_B - t_A$ the time period of the arc passage, $\tau = (t - t_A)/T$ is the normalized time and $\mathbf{f}$ is the sum of the specific forces acting on the two satellites. The equation of motion can also be expressed in terms of position differences between two satellites:

$$\mathbf{r}^{12}(\tau) = \mathbf{r}^{12}_A(1-\tau) + \mathbf{r}^{12}_B\tau - T^2\int_0^1 K(\tau,\tau')\mathbf{f}^{12}(\mathbf{r}(\tau'))d\tau', \tag{3.9}$$

where subscripts 1, 2 denote the different satellites, $\mathbf{f}^{12}$ the difference of the specific forces acting on the two satellites and $\mathbf{r}^{12}_{A/B}$ the position differences between the two satellites for each boundary point A and B. The velocity differences can be derived by differentiating Eq. (3.9):

$$\dot{\mathbf{r}}^{12}(\tau) = \frac{1}{T}(\mathbf{r}^{12}_B - \mathbf{r}^{12}_A) - T\int_0^1 \frac{\partial K(\tau,\tau')}{\partial\tau}\mathbf{f}^{12}(\mathbf{r}(\tau'))d\tau' \tag{3.10}$$

The functional model follows the typical formulation used for LL-SST missions like GRACE, which comprises of a HL-SST and a LL-SST component. Eq. (3.9) is used for the computation of the reference values for the HL-SST part of the observation system. The LL-SST part requires observations that are functionals of the KBR instrument measurements, such as the inter-satellite range, range-rate and range acceleration. The functional model may use those observables individually or totally by taking them all into account. In this study, the ranges and range-rates have been individually used as observables. The reference values for the LL-SST part are derived by projecting Eqs. (3.9) and (3.10) into the line-of-sight (LOS) of the two satellites. Projecting the position vector (Eq. (3.9)) onto the LOS leads to the computation of the inter-satellite range:

$$\rho(\tau) = \| \mathbf{r}^2(\tau) - \mathbf{r}^1(\tau) \| = \mathbf{e}^{12}(\tau)\cdot\mathbf{r}^{12}(\tau), \tag{3.11}$$

where $\mathbf{e}^{12}$ is the unit vector at the LOS direction:

$$\mathbf{e}^{12}(\tau) = \frac{\mathbf{r}^{12}(\tau)}{\| \mathbf{r}^{12}(\tau) \|}, \tag{3.12}$$

which is computed from the position vectors of the simulated dynamic orbits. Accordingly the projection

of the velocity vector (Eq. (3.10)) into the LOS leads to the computation of the inter-satellite range-rate:

$$\dot{\rho}(\tau) = \mathbf{e}^{12}(\tau) \cdot \dot{\mathbf{r}}^{12}(\tau) \tag{3.13}$$

3.5 Formulation of the NEQ system

The relationship between a model function $\mathbf{f}$ and the vector of observations $\bar{\mathbf{l}}$ can be described by the observation equation:

$$\bar{\mathbf{l}} = \mathbf{f}(\bar{\mathbf{x}}, \bar{\mathbf{y}}) + \bar{\mathbf{e}}, \tag{3.14}$$

where $\bar{\mathbf{e}}$ denote the random errors, $\bar{\mathbf{x}}$ are the unknown parameters that are to be estimated (i.e. gravity field coefficients) and $\bar{\mathbf{y}}$ are the parameters that cannot be derived by the observations, but they influence them nevertheless (e.g. high-frequency mass transport processes such as atmospheric changes at daily or hourly time scales). The functional model for the equations of motion (Eq. (3.9)) is not a linear function. A linearization can be achieved by expanding it into Taylor series and neglecting the higher order terms:

$$\bar{\mathbf{l}} = \mathbf{l}_0 + \left.\frac{\partial \mathbf{f}(\bar{\mathbf{x}}, \bar{\mathbf{y}})}{\partial \bar{\mathbf{x}}}\right|_{x_0} (\bar{\mathbf{x}} - \mathbf{x}_0) + \ldots, \tag{3.15}$$

where $\mathbf{l}_0$ is the vector derived from the a priori values of the unknown parameters:

$$\mathbf{l}_0 = \mathbf{f}(\mathbf{x}_0, \mathbf{y}_0). \tag{3.16}$$

Let $\mathbf{l}$ be the vector of the reduced observations, often called as observed minus computed (OMC) vector, or vector of the pre-fit residuals:

$$\mathbf{l} = \bar{\mathbf{l}} - \mathbf{l}_0, \tag{3.17}$$

$\mathbf{x}$ be the solution vector which contains the corrections to the a priori parameters:

$$\mathbf{x} = \bar{\mathbf{x}} - \mathbf{x}_0, \tag{3.18}$$

and $\mathbf{A}$ be the design matrix which contains the partial derivatives of the model function with respect to the unknown parameters:

$$\mathbf{A} = \left.\frac{\partial \mathbf{f}(\bar{\mathbf{x}}, \bar{\mathbf{y}})}{\partial \bar{\mathbf{x}}}\right|_{x_0}. \tag{3.19}$$

The linear observation equations can then be expressed as:

$$\mathbf{l} = \mathbf{A}\mathbf{x} + \mathbf{e} \tag{3.20}$$

This system of linear observation equations satisfies the Gauss-Markov theorem when the expected mean value and the covariance of the random errors are assumed to be:

$$\mathcal{E}(\mathbf{e}) = \mathbf{0} \qquad \text{and} \qquad C(\mathbf{e}) = C(\mathbf{l}) = \sigma_0^2 \mathbf{P}^{-1}, \tag{3.21}$$

where $\mathbf{P}$ is the weight matrix of the observations, $C(\mathbf{l})$ is the covariance matrix of the observations and σ_0 is the a priori standard deviation of the unit weight.

The overdetermined Gauss-Markov model can be optimally solved by LSA, which is based on the minimization of the quadratic sum of the misclosures:

$$\mathcal{L} = \mathbf{e^T P e} = (\mathbf{l} - \mathbf{A}\hat{\mathbf{x}})\mathbf{P}(\mathbf{l} - \mathbf{A}\hat{\mathbf{x}}) = \min. \tag{3.22}$$

The minimization criterion is satisfied when:

$$\frac{\partial \mathcal{L}}{\partial \hat{\mathbf{x}}} = 2\mathbf{A}^T\mathbf{P}\mathbf{A}\hat{\mathbf{x}} - 2\mathbf{A}^T\mathbf{P}\mathbf{l} = 0, \tag{3.23}$$

where the hat symbol (^) at the variable $\mathbf{x}$ represents its estimate. Eq. (3.23) rewritten leads to the system of NEQs:

$$\mathbf{N}\hat{\mathbf{x}} = \mathbf{n} \tag{3.24}$$

with

$\mathbf{N} = \mathbf{A}^T\mathbf{P}\mathbf{A}$ the NEQ matrix and

$\mathbf{n} = \mathbf{A}^T\mathbf{P}\mathbf{l}$ the right-hand side of the NEQ system.

$\mathbf{N}$ is a quadratic symmetric matrix with dimensions that correspond to the number of adjusted model parameters. The NEQ system is then solved by Cholesky decomposition and the final solution vector $\hat{\mathbf{x}}$ is obtained. The a posteriori (also called post-fit) residuals $\hat{\mathbf{e}}$ are computed by:

$$\hat{\mathbf{e}} = \mathbf{A}\hat{\mathbf{x}} - \mathbf{l} \tag{3.25}$$

The estimated (a posteriori) standard deviation of unit weight (also called root mean square (RMS) error) is estimated by:

$$\hat{\sigma}_0 = RMS = \sqrt{\frac{\hat{\mathbf{e}}^\mathbf{T}\mathbf{P}\hat{\mathbf{e}}}{f}}, \quad f > 0\ , \tag{3.26}$$

where $f = n - m$ is the degree of freedom, n is the number of observations and m the number of unknown adjusted model parameters. The variance covariance matrix $\mathbf{C}(\mathbf{x})$ of the adjusted model parameters is defined as:

$$\mathbf{C}(\mathbf{x}) = \hat{\sigma}_0^2 \mathbf{N}^{-1}. \tag{3.27}$$

Eq. (3.9) describes the position differences between two satellites at a random normalized epoch τ_i,

where

$$\tau_i = \frac{i-1}{N-1}, \text{for } i = 1, \ldots, N, \tag{3.28}$$

and N is the total number of discrete uniformly divided observation points inside one arc. Considering all the observation points $\mathbf{r}^{12}_{\tau_i}$ in one arc, the HL-SST part of the functional model can be written in a matrix form:

$$\mathbf{l} = \mathbf{B}\mathbf{b} + \mathbf{h}, \tag{3.29}$$

where

$$\mathbf{l}_r = \begin{pmatrix} \mathbf{r}^{12}(\tau_i) - \mathbf{r}^{12}_0(\tau_i) \\ \vdots \\ \mathbf{r}^{12}(\tau_N) - \mathbf{r}^{12}_0(\tau_N) \end{pmatrix} \quad \text{the vector of the reduced observations,} \tag{3.30}$$

$$\mathbf{B} = \begin{pmatrix} (1-\tau_i) & \tau_i \\ \vdots & \\ (1-\tau_N) & \tau_N \end{pmatrix} \quad \text{the matrix with the normalized time values,} \tag{3.31}$$

$$\mathbf{b} = \begin{pmatrix} \mathbf{r}^{12}_A \\ \mathbf{r}^{12}_B \end{pmatrix} \quad \text{the vector with the arc boundary values,} \tag{3.32}$$

$$\tag{3.33}$$

and $\mathbf{h}$ the vector with the integral function of (3.9) evaluated at the N observation points:

$$\mathbf{h} = \begin{pmatrix} \mathbf{h}(\tau_i) \\ \vdots \\ \mathbf{h}(\tau_N) \end{pmatrix} \quad \text{with} \quad \mathbf{h}(\tau_i) = -T^2 \int_0^1 K(\tau, \tau')\mathbf{f}^{12}(\mathbf{r}(\tau'))d\tau' \tag{3.34}$$

The unknown parameters of the functional model $\mathbf{x}$ consist of the gravity field coefficients and the boundary arc values, occupying vectors $\tilde{\mathbf{x}}$ and $\mathbf{b}$, respectively. The relationship of the functional model with the unknown parameters $\tilde{\mathbf{x}}$ is achieved through linearization of the integral function $\mathbf{h}$ with respect to the unknown parameters according to Eq. (3.15):

$$\mathbf{h} = \mathbf{h}_0 + \tilde{\mathbf{A}}\tilde{\mathbf{x}}, \tag{3.35}$$

where $\tilde{\mathbf{A}}$ is the design matrix with the partial derivatives of the integral $\mathbf{h}$ with respect to the unknown gravity field coefficients $\tilde{\mathbf{x}}$:

$$(\tilde{\mathbf{A}})_{ij} = \frac{\partial \mathbf{h}(\tau_i)}{\partial \tilde{x}_j}, \tag{3.36}$$

and $\mathbf{h}_0$ the reference values of the integral function $\mathbf{h}$. In case of position differences used as observables, the relationship between the integral function and the unknown parameters can be derived by applying the chain rule to the partial derivatives of Eq. (3.36) through the differences of the specific forces $\mathbf{f}^{12}_k$

between the two satellites, at the discretized epochs τ_i:

$$\tilde{\mathbf{A}} = \mathbf{KG} \quad \text{with} \quad (\mathbf{K})_{ik} = \frac{\partial \mathbf{h}(\tau_i)}{\partial \mathbf{f}_k^{12}} \quad \text{and} \quad (\mathbf{G})_{kj} = \frac{\partial \mathbf{f}_k^{12}}{\partial \tilde{x}_j} \tag{3.37}$$

with $\mathbf{K}$ the integration kernel matrix and $\mathbf{G}$ the matrix with the partial derivatives of the specific forces with respect to the gravity field coefficients. The convolution of the acceleration vector with the kernel function at Eq. (3.9) can now be converted to a matrix multiplication, which gives the kernel matrix $\mathbf{K}$ the following form:

$$\mathbf{K} = -T^2 \int_0^1 K(\tau, \tau') \cdot d\tau'. \tag{3.38}$$

The derivation details of matrix $\mathbf{K}$ can be found in Mayer-Gürr (2006). The matrix $\mathbf{G}$ contains the partials along all three directions:

$$\mathbf{G}_x = \begin{pmatrix} \frac{\partial \ddot{x}_0}{\partial f_0^{12}} & \frac{\partial \ddot{x}_0}{\partial f_1^{12}} & \cdots & \frac{\partial \ddot{x}_0}{\partial f_{m-1}^{12}} \\ \frac{\partial \ddot{x}_1}{\partial f_1^{12}} & \frac{\partial \ddot{x}_1}{\partial f_1^{12}} & \cdots & \frac{\partial \ddot{x}_1}{\partial f_{m-1}^{12}} \\ \vdots & \vdots & \ddots & \vdots \\ \frac{\partial \ddot{x}_{u-1}}{\partial f_0^{12}} & \frac{\partial \ddot{x}_{u-1}}{\partial f_1^{12}} & \cdots & \frac{\partial \ddot{x}_{u-1}}{\partial f_{m-1}^{12}} \end{pmatrix}, \quad \mathbf{G}_y = \begin{pmatrix} \frac{\partial \ddot{y}_0}{\partial f_0^{12}} & \frac{\partial \ddot{y}_0}{\partial f_1^{12}} & \cdots & \frac{\partial \ddot{y}_0}{\partial f_{m-1}^{12}} \\ \frac{\partial \ddot{y}_1}{\partial f_1^{12}} & \frac{\partial \ddot{y}_1}{\partial f_1^{12}} & \cdots & \frac{\partial \ddot{y}_1}{\partial f_{m-1}^{12}} \\ \vdots & \vdots & \ddots & \vdots \\ \frac{\partial \ddot{y}_{u-1}}{\partial f_0^{12}} & \frac{\partial \ddot{y}_{u-1}}{\partial f_1^{12}} & \cdots & \frac{\partial \ddot{y}_{u-1}}{\partial f_{m-1}^{12}} \end{pmatrix},$$
$$\mathbf{G}_z = \begin{pmatrix} \frac{\partial \ddot{z}_0}{\partial f_0^{12}} & \frac{\partial \ddot{z}_0}{\partial f_1^{12}} & \cdots & \frac{\partial \ddot{z}_0}{\partial f_{m-1}^{12}} \\ \frac{\partial \ddot{z}_1}{\partial f_1^{12}} & \frac{\partial \ddot{z}_1}{\partial f_1^{12}} & \cdots & \frac{\partial \ddot{z}_1}{\partial f_{m-1}^{12}} \\ \vdots & \vdots & \ddots & \vdots \\ \frac{\partial \ddot{z}_{u-1}}{\partial f_0^{12}} & \frac{\partial \ddot{z}_{u-1}}{\partial f_1^{12}} & \cdots & \frac{\partial \ddot{z}_{u-1}}{\partial f_{m-1}^{12}} \end{pmatrix}. \tag{3.39}$$

Eqs (3.29) and (3.37) together deliver the linear Gauss-Markov model for the HL-SST part when position differences are used as observables:

$$\bar{\mathbf{l}}_r = \mathbf{Bb} + \mathbf{KG}\tilde{\mathbf{x}} + \mathbf{e}. \tag{3.40}$$

The NEQ system is completed with the inclusion of the linear Gauss-Markov model for LL-SST part:

$$\bar{\mathbf{l}}_\rho = \mathbf{RBb} + \mathbf{RKG}\tilde{\mathbf{x}} + \mathbf{e}, \tag{3.41}$$

where $\mathbf{R}$ is the matrix with the partial derivatives of the 1-D inter-satellite ranges with respect to the corresponding 3-D vectors of the position differences, which implicitly serves in projecting the HL-SST

observation equations to the LOS:

$$\mathbf{R} = \begin{pmatrix} \frac{\partial \rho}{\partial \mathbf{r}^{12}}(\tau_i) \\ \vdots \\ \frac{\partial \rho}{\partial \mathbf{r}^{12}}(\tau_N) \end{pmatrix} = \begin{pmatrix} \mathbf{e}^{12}(\tau_i) \\ \vdots \\ \mathbf{e}^{12}(\tau_N) \end{pmatrix}, \tag{3.42}$$

where $\mathbf{e}^{12}(\tau_i) = [\mathbf{e}_x^{12}(\tau_i)\mathbf{e}_y^{12}(\tau_i)\mathbf{e}_z^{12}(\tau_i)]$ is the unit vector at the LOS direction for epoch τ_i. The reduced observation vectors $\bar{\mathbf{l}}_r$ and $\bar{\mathbf{l}}_\rho$ can be computed beforehand as follows:

$$\bar{\mathbf{l}}_r = \mathbf{r}^{12} - \mathbf{r}_0^{12} \tag{3.43}$$

$$\bar{\mathbf{l}}_\rho = \boldsymbol{\rho} - \boldsymbol{\rho}_0 \tag{3.44}$$

where the measured parameters of position differences $\mathbf{r}^{12}$ are derived from kinematic orbit determination and those of ranges $\boldsymbol{\rho}$ from the LL-SST distance measuring instrument, when processing with real data. In our simulation environment, the dynamic orbits (Sec. 3.3) are used instead. The reference parameters $\mathbf{r}_0$ and ρ_0 are computed by:

$$\mathbf{r}_0^{12} = \mathbf{B}\mathbf{b}_0 - \mathbf{K}\mathbf{f}_0^{12}, \tag{3.45}$$

$$\boldsymbol{\rho}_0 = \mathbf{R}_0\mathbf{B}\mathbf{b}_0 - \mathbf{R}_0\mathbf{K}\mathbf{f}_0^{12}, \tag{3.46}$$

with $\mathbf{f}_0^{12}$ being the vector of the reference values for the differences of the specific forces acting on the two satellites, estimated by use of a reference background gravity field model. The vector $\mathbf{b}_0$ contains the reference values for the boundary points $\mathbf{r}_A^{12}$, $\mathbf{r}_B^{12}$ and the matrix $\mathbf{R}_0$ the reference values for the unit vectors $\mathbf{e}^{12}$, which are estimated from the simulated dynamic orbits.

In case of using range rates $\dot{\rho}$ as observables for the LL-SST part, the matrices $\mathbf{K}$ and $\mathbf{B}$ in Eqs (3.41), (3.46) are substituted by their time derivatives $\dot{\mathbf{K}}$ and $\dot{\mathbf{B}}$ respectively, where:

$$\dot{\mathbf{K}} = -T \int_0^1 \frac{\partial K(\tau, \tau')}{\partial \tau} \cdot d\tau', \tag{3.47}$$

and

$$\dot{\mathbf{B}} = \frac{1}{T} \begin{pmatrix} -1 & 1 \\ \vdots & \vdots \\ -1 & 1 \end{pmatrix}. \tag{3.48}$$

The complete NEQ system consists of a HL-SST and a LL-SST part which contain observations of different accuracy. For example, GRACE real data processing consists of a HL-SST part with position differences computed from kinematic orbits of some *cm* accuracy, and a LL-SST part of KBR inter-satellite measurements of some μm accuracy. In order to take these accuracy differences into account the

complete NEQ system is expressed by a weighting summation of those two components (see also Sec. 3.6.3):

$$\mathbf{N} = \frac{1}{\sigma_{hl}^2}\mathbf{N}_{hl} + \frac{1}{\sigma_{ll}^2}\mathbf{N}_{ll}, \tag{3.49}$$

$$\mathbf{n} = \frac{1}{\sigma_{hl}^2}\mathbf{n}_{hl} + \frac{1}{\sigma_{ll}^2}\mathbf{n}_{ll}, \tag{3.50}$$

where the index *hl* stands for the HL-SST and *ll* for the LL-SST part.

3.6 Solution of the NEQ system

This section is dedicated to the description of the methods that lead to the optimal solution of the overdetermined observation system with the method of LSA. The following sections are dedicated to the description of those methods. Fig. 3.6 displays the scheme that is followed for estimating the unknown parameters, as well as the a posteriori analysis that is performed.

3.6.1 Parameterization of the unknown parameters

As described in Sec 3.5, the functional model defines two types of unknown parameters to be estimated; namely the gravity field coefficients and the boundary values of each arc. However, it is possible that other parameters are also estimated (e.g. empirical accelerations, Sec. 6.2). In this study, we categorize the parameters to be estimated as *local* and *global* parameters. The local parameters are all the parameters that are valid only for a short period of time (i.e. time period of short arc, half-daily, daily), such as the position vector at the boundary points and empirically estimated accelerations. The global parameters are the parameters that are estimated once over the complete observation time period, such as the gravity field coefficients $\overline{C}_{nm}, \overline{S}_{nm}$.

The simulator of this study makes use of a modification of the "short-arc"approach (Mayer-Gürr, 2006) proposed by Yi (2012), that ensures the continuity of the orbit. The approach is pretty handy when handling orbit data with interruptions, since whenever a data gap appears, the arc is terminated and a new one is started. Uninterrupted short arcs are thus stacked together in a long arc whose boundary values are set up as unknowns. Inside the long arc, the short arcs are connected to each other by setting up a special condition which demands the end of one arc to have the same position as the beginning of its consecutive. Eq. (3.40) can be expressed in terms of the linearized observation equations of Eq. (3.20) for a random arc i, with the design matrix $\mathbf{A}_i$ and the total vector of unknown parameters $\mathbf{x}_i$:

$$\mathbf{A}_i = \begin{pmatrix} \mathbf{B}_i \\ \tilde{\mathbf{A}}_\mathbf{i} \end{pmatrix} \qquad \text{and} \qquad \mathbf{x}_i = \begin{pmatrix} \mathbf{b}_i \\ \tilde{\mathbf{x}} \end{pmatrix} \tag{3.51}$$

As described in Sec. 3.6.3, the NEQs are accumulated arc-wise, leading to the accumulated design matrix

$\mathbf{A}$ and the vector of the total unknown parameters over the period of 1 long arc $\mathbf{x}$:

$$\mathbf{A} = \begin{pmatrix} \acute{\mathbf{B}} \\ \bar{\mathbf{A}} \end{pmatrix} \qquad \text{and} \qquad \mathbf{x} = \begin{pmatrix} \acute{\mathbf{b}} \\ \tilde{\mathbf{x}} \end{pmatrix} \tag{3.52}$$

where $\bar{\mathbf{A}} = \sum_{i=1}^{J} \mathbf{A}_i$ and J is the total number of short arcs inside one long arc. $\acute{\mathbf{B}}$ and $\acute{\mathbf{b}}$ represent the matrix with the normalized time values and the vector with the boundary values to be estimated over 1

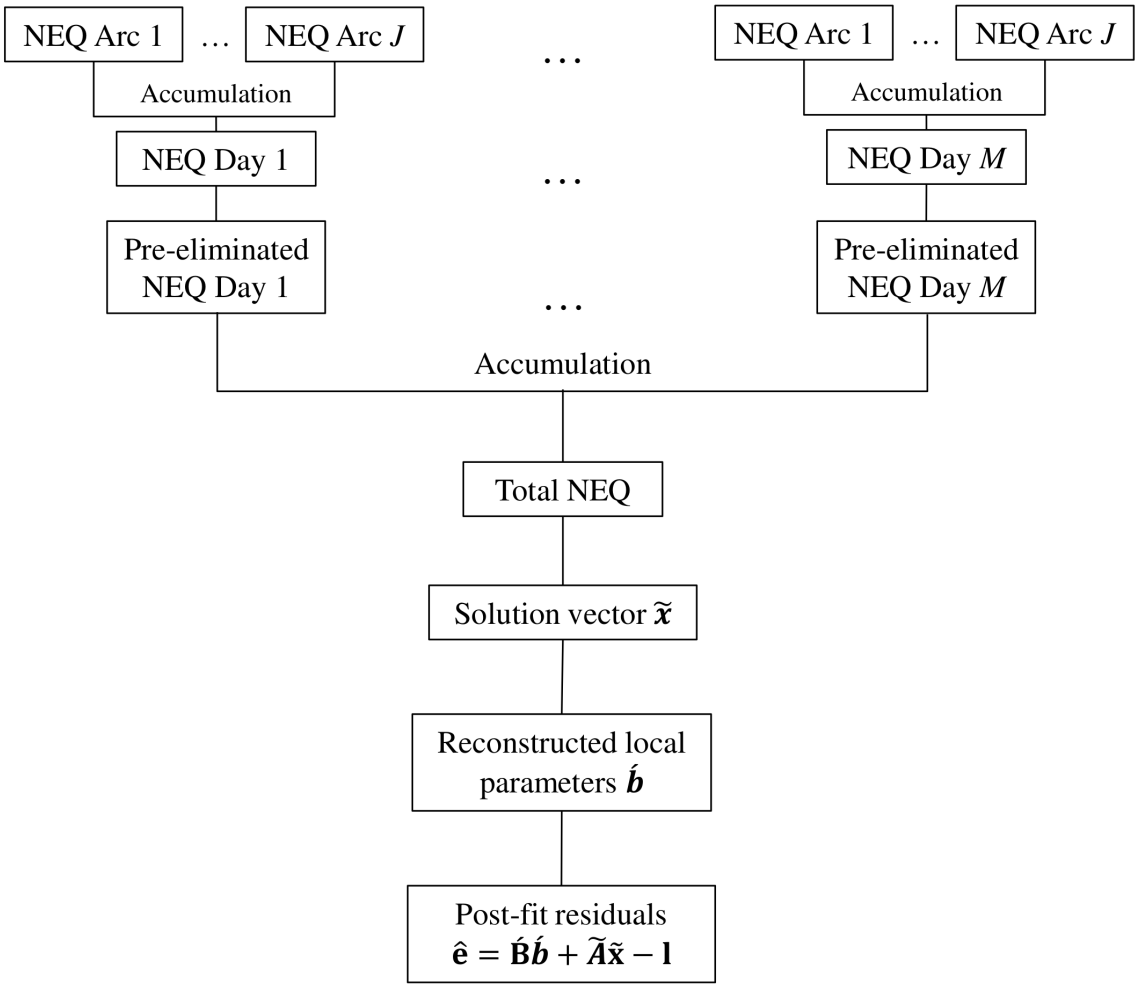

Figure 3.6.1: Parameter estimation flowchart

long arc correspondingly:

$$\acute{\mathbf{B}} = \begin{pmatrix}
(1-\tau_1) & \tau_1 & & & & & \\
(1-\tau_2) & \tau_2 & & & & & \\
\vdots & \vdots & & & 0 & & \\
(1-\tau_N) & \tau_k & & & & & \\
 & (1-\tau_1) & \tau_1 & & & & \\
 & (1-\tau_2) & \tau_2 & & & & \\
0 & \vdots & \vdots & & 0 & & \\
 & (1-\tau_N) & \tau_N & & & & \\
\vdots & \vdots & \vdots & \ddots & & & \\
 & & & & (1-\tau_1) & \tau_1 & \\
0 & & 0 & & (1-\tau_2) & \tau_2 & \\
 & & & & \vdots & \vdots & \\
 & & & & (1-\tau_N) & \tau_N &
\end{pmatrix} \begin{matrix} 1^{st}Arc \\ \\ \\ \\ 2^{nd}Arc \\ \\ \\ \\ \vdots \\ \\ \\ J^{th}Arc \\ \\ \\ \\ \end{matrix}, \tag{3.53}$$

$$\acute{\mathbf{b}} = \begin{pmatrix} \mathbf{r}_A^1 \\ \mathbf{r}_A^2 \\ \vdots \\ \mathbf{r}_A^N \\ \mathbf{r}_B^N \end{pmatrix}, \tag{3.54}$$

where the subscript $\wedge^{12}$ denoting the position difference between the two satellites has been neglected for simplification. In our simulated environment we deal with uninterrupted orbit data. Therefore, the short arcs are bonded to each other forming a long arc which has the length of 1 day. As an example, considering a constant time period of 30 min for the short arcs leads to a total number of local parameters equal to $(J+1)\times 3 = 147$ per satellite pair for the period of 1 day.

3.6.2 Parameter pre-elimination

The explicit solution of the local parameters (Sec. 3.6.1) is not always required as a final product. For the sake of efficiency, the local parameters are pre-eliminated from the NEQ system at a daily basis (Fig 3.1), after the accumulation of the NEQs (Sec. 3.6.3). The dimension of the NEQ system is then reduced significantly, resulting into a more rapid inversion of the final normal matrix when solving for the gravity field parameters.

Let us denote the two sets of parameters to be estimated as $\mathbf{x}_1 = \acute{\mathbf{b}}$ for the local parameters and $\mathbf{x}_2 = \tilde{\mathbf{x}}$

for the global parameters. The NEQ system can then be divided in two parts:

$$\begin{pmatrix} \mathbf{N}_{11} & \mathbf{N}_{12} \\ \mathbf{N}_{21} & \mathbf{N}_{22} \end{pmatrix} \cdot \begin{pmatrix} \mathbf{x}_1 \\ \mathbf{x}_2 \end{pmatrix} = \begin{pmatrix} \mathbf{n}_1 \\ \mathbf{n}_2 \end{pmatrix} \tag{3.55}$$

The sub-vector $\mathbf{x}_2$ contains the parameters that we want to solve for, while sub-vector $\mathbf{x}_1$ the parameters to be pre-eliminated. Solving the first part of Eq. (3.55) for $\mathbf{x}_1$ gives:

$$\mathbf{x}_1 = \mathbf{N}_{11}^{-1}(\mathbf{n}_1 - \mathbf{N}_{12}\mathbf{x}_2). \tag{3.56}$$

Inserting Eq. (3.56) into the second part of Eq. (3.55) yields:

$$\left(\mathbf{N}_{22} - \mathbf{N}_{21}\mathbf{N}_{11}^{-1}\mathbf{N}_{21}\right)\mathbf{x}_2 = \left(\mathbf{n}_2 - \mathbf{N}_{21}\mathbf{N}_{11}^{-1}\mathbf{n}_1\right). \tag{3.57}$$

Thus, the NEQ system can be re-arranged to:

$$\mathbf{N}_{22}^{*}\mathbf{x}_2 = \mathbf{n}_2^{*}, \tag{3.58}$$

where

$\mathbf{N}_{22}^{*} = \mathbf{N}_{22} - \mathbf{N}_{21}\mathbf{N}_{11}^{-1}\mathbf{N}_{21}$ the normal matrix of the global parameters $\mathbf{x}_2$ and

$\mathbf{n}_2^{*} = \mathbf{n}_2 - \mathbf{N}_{21}\mathbf{N}_{11}^{-1}\mathbf{n}_1$ the right-hand side of the reduced NEQ system.

From Eq. (3.52), it follows that matrix $\mathbf{N}_{11}$ corresponds to the matrix product $\acute{\mathbf{B}}^T\mathbf{P}\acute{\mathbf{B}}$, $\mathbf{N}_{22}$ to $\bar{\mathbf{A}}^T\mathbf{P}\bar{\mathbf{A}}$, $\mathbf{N}_{21}$ to $\acute{\mathbf{B}}^T\mathbf{P}\bar{\mathbf{A}}$, $\mathbf{n}_1$ to $\acute{\mathbf{B}}^T\mathbf{Pl}$ and $\mathbf{n}_2$ to $\bar{\mathbf{A}}^T\mathbf{Pl}$. After the pre-elimination, the pre-eliminated parameters $\mathbf{x}_1$ are taken account in the reduced NEQ system, although their estimates are not explicitly available. This procedure does not influence the results for the global parameters $\mathbf{x}_2$, which are the same as if the pre-elimination was not performed. During the gravity field processing of this study, the pre-elimination is performed to the accumulated NEQs obtained from observations of 1 day. After solving the NEQ system for the global parameters $\mathbf{x}_2$, the pre-eliminated local parameters $\mathbf{x}_1$ can be retrieved by means of back-substitution, using Eq. (3.56).

3.6.3 Accumulation of the NEQs

The NEQ system requires storage and matrix operations that are of very large dimensions. A monthly gravity field solution for a satellite mission like GRACE with a spatial resolution of 166 km (approx. degree and order d/o 120), demands the estimation of 14400 unknown gravity field coefficients. Without taking into account the co-estimated local parameters which are pre-eliminated at a previous step, the number of unknowns will be equal to $m = 14400$ in a period of 1 month. Assuming a continuous orbit sampling of 5 sec, the number of observations during 1 month period will be equal to $n = 518400$. The corresponding design matrix $\mathbf{A}_{n\times m}$ would possess 50 GBytes of disk space and the weight matrix

$\mathbf{P}_{n\times n}$ 1.8 TBytes. The computation of the normal matrix $\mathbf{N}_{m\times m} = \mathbf{A}^T_{n\times m}\mathbf{P}_{n\times n}\mathbf{A}_{n\times m}$ requires an enormous amount of computer memory, which is not available with the current computer performing standards. The demands for computer memory and storage are much more pronounced when simulating NGGM scenarios with 2 satellite pairs and double number of observations n than the GRACE mission.

Luckily, the dimension of the system can be reduced to that of a size corresponding to the observations of a short arc. This can be achieved by use of the sequential LSA, according to which the vectors of the reduced observations $\mathbf{l}$ and the design matrix $\mathbf{A}$ are generated for each short arc:

$$\mathbf{l} = \begin{pmatrix} \mathbf{l}_1 \\ \mathbf{l}_2 \\ \vdots \\ \mathbf{l}_J \end{pmatrix} \qquad \text{and} \qquad \mathbf{A} = \begin{pmatrix} \mathbf{A}_1 \\ \mathbf{A}_2 \\ \vdots \\ \mathbf{A}_J \end{pmatrix} \tag{3.59}$$

where J is the total number of arcs in 1 day. The NEQ system is then formed and accumulated arc-wise:

$$\mathbf{N} = \sum_{i=1}^{J} \mathbf{A}_i^T \mathbf{P}_i \mathbf{A}_i \qquad \text{and} \qquad \mathbf{n} = \sum_{i=1}^{J} \mathbf{A}_i^T \mathbf{P}_i \mathbf{l}_i, \tag{3.60}$$

where observations between different short-arcs are assumed to be uncorrelated. The accumulated NEQ system is afterwards saved, but the arc-wise generated NEQ system is removed from the computer memory, therefore releasing the necessary memory space for the next short arc. The combined NEQ system has now the size of an arc-sized system, which can then be solved to estimate the parameter vector $\hat{\mathbf{x}}$.

In our simulation environment, the NEQs are accumulated arc-wise for the period of 1 day (period of 1 long arc). The local parameters are then pre-eliminated and the resulting NEQs are stored on a daily basis. The setup of the daily NEQs is accelerated by exploiting the benefits of parallel processing and attributing the processing of an individual day to a node of the Linux cluster. Finally, the daily NEQs are combined in a monthly (or other) basis using the sequential LSA approach (this time accumulating daily), and the system is solved through Cholesky decomposition.

Chapter 4

Design aspects and error budget of future dedicated gravity satellite missions

The pre-requisites for NGGMs in order to improve the state-of-the-art accuracies that current missions deliver, have been analyzed in several publications (Rummel, 2003; Sneeuw et al., 2005). The technological improvements of the NGGMs concerning the metrology of their sensors and the satellite system, need to be accompanied by an optimization of the orbit design and the satellite formation parameters. The search space for the parameters that can be, within certain ranges, adjusted in order to improve the performance of a gravity mission, is indeed very wide. Apart from that, NGGMs plan to take advantage of the benefits that SFFs which are more complicated than the simple GRACE-type in-line SFFs can offer. This section begins with an overview of the state-of-the-art orbital design choices and the possible SFF candidates for the NGGMs. As a next step, the science requirements consolidated by the scientific and user communities are summarized, followed by the description of the noise models used for the simulations. Finally, an error budget analysis with the given noise models is performed.

4.1 Orbit design

The performance of a gravity mission should already be defined in the pre-launch period, in order for the selected orbit design to be optimized but also feasible. The parameters that can be adjusted, such as the orbital altitude, the inter-satellite distance, the inclination and the repeat mode of the satellite orbits, influence directly and indirectly the quality of the gravity field retrieval.

The choice of the orbital altitude is one of the most important parameters that affects directly the gravity field estimation. For applications that aim at measuring very long-wavelength features such as the temporal changes of Earth's oblateness or relativistic parameters, the choice of higher altitudes is preferred due to their serving as natural low-pass filters. In all other cases, especially when high resolution gravity field mapping is the goal, the best choice is simply the lowest possible altitude. This can be explained from the so-called inverse attenuation factor $[r/R_E]^{n+1}$, which reflects the variation of

the gravity signal amplitude depending on spherical harmonic degree n due to the change of the orbital altitude r. This factor results in the degradation of the gravity field recovery with the choice of higher orbital altitudes.

For a non-drag free mission, the lowest meaningful starting altitude will be around 450 km, where GRACE mission itself flies at a mean orbital altitude of 480 km. The satellite will then slowly descend due to atmospheric drag, and its mission lifetime will depend on the solar activity and the satellite's aerodynamic parameters. In case of a drag-free mission, an allowable operational orbital altitude for an assumed 10-year mission lifetime, will be around 290 km (Wiese et al., 2012). In Iran Pour et al. (2015), it is assumed that the use of ion thrusters for an in-line formation will allow an altitude limit of 340 km, taking into account a higher solar activity profile. The altitude choice also affects the errors induced by temporal aliasing. In Murböck et al. (2014), the orbital altitude choice is optimized towards minimization of temporal aliasing errors from both tidal and non-tidal sources.

Concerning the inter-satellite separation distance for LL-SST NGGMs, a laser interferometer will be likely used, for which a 100 km separation is considered as a fair trade-off between instrument performance and relative accuracy in determining short and long wavelength features of the gravity field (Wiese et al., 2009). The inclination choice is closely connected to the spatial coverage. For example, a polar orbit samples the Earth globally, while an inclined one may provide denser coverage at regions with lower latitude at the expense of polar gaps with a diameter equal to $2 \times (i - 90)^o$.

NGGMs are expected to fly in circular or near-circular orbits, in order to keep the relative changes in the measured inter-satellite distances due to orbit eccentricity at a minimum level. It is also planned to consider orbits with repeat subsatellite tracks in order to guarantee consistency between solutions, which is something that GRACE lacks. A repeat period (or repeat cycle) of a satellite track is performed exactly after β orbital revolutions, while the Earth rotates α times with respect to (w.r.t.) the satellite's precessing orbital plane. Thus, a satellite track repeats itself after an integer number of β orbital revolutions and an integer number of α nodal days. A nodal day is defined as the time period needed for the ascending node to be repeated over the same Earth-fixed meridian. A sub-cycle of the satellite track denotes a separate sub-pattern that is repeated during the period of a full cycle. The repeat cycle or sub-cycle is principally related to the choice of three orbital parameters, namely the orbital altitude, the inclination and the eccentricity. Perhaps an even more important aspect than the choice of the orbit repeat modes, is the maintenance of a dense sampling. Particularly, the goal is to obtain a homogeneous sampling with a dense ground-track pattern that evolves uniformly in time. The orbit design should generally avoid constellations that deliver big ground-track gaps, by predicting the gap evolution separately along the longitudes and the latitudes.

Overall, the orbit design can be optimized towards the following NGGM mission requirements:

- high spatial resolution,
- long mission lifetime,
- high isotropy of the error spectrum,

- feasibility of the SFF from technological and financial point of view,
- optimal usage of new sensor technologies and, at the same time, minimization of their coupling effects,
- minimization of aliasing effects,
- homogeneous and dense ground-track sampling,
- constant repeat orbits cycles and sub-cycles

However, the optimization of the orbit design towards some of the aforementioned requirements (e.g. system isotropy), has limitations when it comes to SFFs of a simple one-pair mission like the one used for the GRACE mission.

4.2 Satellite formation flights

SFF concepts have been the study objective of space agencies like NASA, ESA, Centre National d'Études Spatiales (CNES) and DLR since the beginning of gravity mission planning. The major difference between a SFF and a constellation of satellites, is that in case of a SFF the relative position and velocity and sometimes attitudes between two satellites can be controlled. SFFs with focus on recovering Earth's gravity field, make use of the Satellite-to-Satellite Tracking (SST) measurement principle.

The first SFF concept used for a LL-SST mission, was the master-slave formation used for the GRACE mission with a pure along-track configuration (Fig. 4.2.1, top-left). GRACE satellites fly simple in-line SFF at near-polar orbits, due to the demand for a global coverage. This leads to a severe anisotropic sensitivity of the system, where the East-West variations of the gravitational field are sensed much worse than the North-South ones. Since its launch, the data processing revealed the shortcomings stemming from the restrictions imposed from its SFF (Sec. 2.4.2). Some of those shortcomings, including the system anisotropy and the temporal aliasing effects, can be overcome by adding a second pair of satellites (Visser et al., 2010; Wiese et al., 2011a). In the scientific literature there exist several simulation studies that investigate the impact of complicated SFFs and SFFs constellations (Elsaka et al., 2014; Wiese et al., 2009), as well as more feasible ones (Bender et al., 2008). Let us assume a leading satellite instant position x, y, z expressed at the satellite-fixed reference frame with axes X^S, X^W, X^R (see Sec. 3.2). In case of circular orbits, the relative equations of motion are simplified to the linearized Hill equations, which are also referred to as Clohessy-Wiltshire equations (Clohessy and Wiltshire, 1960):

$$\begin{aligned} \ddot{x} + 2n\dot{z} &= f_x, \\ \ddot{y} + n^2 y &= f_y, \\ \ddot{z} - 2n\dot{x} - 3n^2 z &= f_z, \end{aligned} \tag{4.1}$$

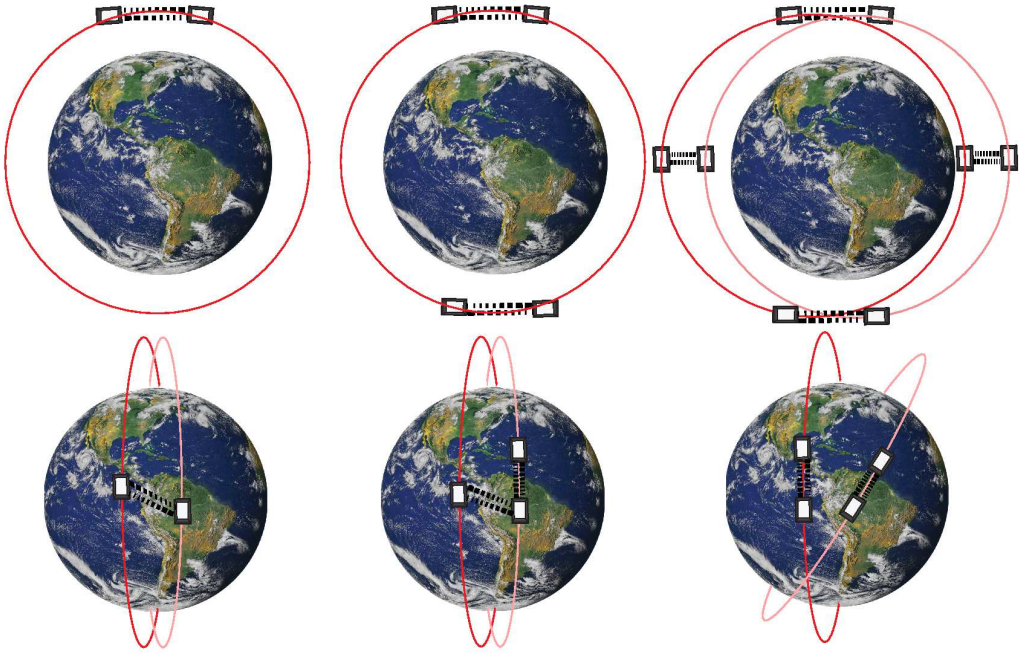

Figure 4.2.1: SFF and SFF constellations for NGGMs. Top (left to right): GRACE-type, multi-GRACE-type and Cartwheel. Bottom (left to right): Pendulum, GRACE-Pendulum and Bender-type.

where n is the mean motion of the satellite. The system of Eqs. in (4.1) can be solved in a closed form, assuming that no perturbations or thrusting accelerations are present (i.e. $f_x = f_y = f_z = 0$). Exploring the Clohessy-Wiltshire equations along with some principles of the relative dynamics of a circular orbit (Elsaka, 2010), different SFF architectures can be realized.

When a satellite orbit with an out-of-plane motion (y component), is added to a satellite orbit with a GRACE-type SFF, the configuration is of a *Pendulum*-type (Fig. 4.2.1, bottom-left). The two satellites have slightly different orbital planes, but the baseline vector maintains a constant direction. The along-track relative motion of the satellites, is replaced by the cross-track relative motion. Due to the difference of the ascending nodes, a maximum out-of-plane separation takes place at the equator and a minimum at the poles. A step further from the classical Pendulum SFF, is realized with the *GRACE-Pendulum*-type SFF constellation (Fig. 4.2.1, bottom-middle), where a pair of GRACE-type satellites is combined with a Pendulum-type formation. This constellation comprises of three satellites (GR-A, GR-B and PEND-A) and establishes two inter-satellite baselines; one between GR-A and GR-B (corresponding to the GRACE-type SFF) and another between GR-A and PEND-A (corresponding to the Pendulum-type SFF).

All the simple SFFs that contain one pair of satellites, have restrictions when it comes to mutual increase of both spatial and temporal sampling. The relationship between the spatial and temporal sampling can be approximated by the so-called Heisenberg-rule of spatio-temporal sampling of a satellite (Reubelt et al., 2010). For a LEO satellite the product between the spatial sampling S_{space} and the tem-

poral sampling S_{time} can be regarded as constant:

$$S_{space} \cdot S_{time} = 2\pi T_{rev} = const, \tag{4.2}$$

where T_{rev} is the revolution period of the satellite. According to that rule, an increase of the spatial sampling leads to a reduction of the temporal sampling (longer observation periods). This sampling problem can be overcome by use of multiple SFF, or else SFF constellations.

A simple SFF constellation regarding the design complexity, is the *four-satellite coplanar* configuration (Fig. 4.2.1, top-middle). This configuration consists of two collinear GRACE-type satellite pairs which are in the same orbital plane, but distant from each other. The only benefit of this configuration is that the sampling frequency is twice that of the simple GRACE-type formation, which brings improvements regarding aliasing issues. Another SFF constellation that has gained a lot of attention among NGGM investigation studies, is the so-called *Cartwheel* configuration (Fig. 4.2.1, top-right). This SFF constellation enables multiple observation types of satellite observations by considering the relative motion of a follower satellite S_2 around the leader S_1, at a 2:1 relative elliptical motion (i.e. the semi-major axis has twice the size of the semi-minor one). The observations are obtained during the motion in the along-track direction, as well as in the radial direction.

SFFs constellations of GRACE-Pendulum or Cartwheel type, are quite demanding in terms of mission implementation due to several constraints that the state-of-the-art technology imposes regarding the satellites' relative motion and omnidirectional inter-satellite ranging system (Flechtner et al., 2014b). The sustainability of their formation will require complex maneuvers to be performed frequently, which will substantially increase the demands on the propulsion system in a drag-free motion. In Wiese et al. (2009) it is concluded that in case of the Cartwheel-type SFF, restrictions imposed from inaccuracies in the background models (errors in the de-aliasing models and the ocean tide models) may lead to performance similar to a GRACE-type SFF.

An SFF constellation design that has proved quite promising regarding NGGM planning, while at the same time retaining its feasibility from an engineering point of view, is the *Bender*-type constellation introduced by Bender et al. (2008). This constellation comprises of two pairs of collinear satellites, one pair in a near-polar orbit and one in a lower inclined orbit (Fig. 4.2.1, bottom-right). The inclusion of the lower inclined pair improves the East-West sensitivity to the gravity field variations compared to the typical GRACE-type SFF. Therefore, the combination of two non-isotropic measurements taken in different directions, increases the isotropy of the system. Another advantage of this configuration is that even if the regions near the poles are sampled with only the near-polar pair, the spatial resolution is not compromised due to the fact that the subsatellite tracks are denser in those regions. Overall, the Bender configuration is considered as a good compromise between mission feasibility and potential improvement of the gravity field estimation accuracy (Wiese et al., 2011a; Elsaka et al., 2014). This constellation has already shown (Visser et al., 2010) substantial improvements regarding temporal aliasing effects, where its error is reduced by at least one order of magnitude compared to GRACE.

4.3 Selected orbits for the simulations

The satellite configuration used in this study for investigations concerning NGGMs, consists of a Bender-type constellation flying in drag-free mode. Details about the orbit setup of the two configurations are given in Table 4.1. The GRACE-type polar pair of the Bender constellation is used for a thorough investigation on the effect of next generation sensor technology on the gravity field estimation process (Sec. 4.6 and Chapter 5).

Altitude (km)	Inclination (deg)	Inter-satellite distance (km)	β/α (rev./day)	sub-cycle (days)
		Polar pair		
361.9	92	100	172/11	3
		Inclined pair		
342.5	115	100	460/29	7

Table 4.1: Configuration setup of the orbits

Sampling (sec)	Background models	max d/o (deg)	Absolute accuracy (m)
5	GOCO03s GOT4.7 AOHIS	120 50 120	10^{-8}

Table 4.2: Orbit integration setup parameters

The Bender-type configuration serves for investigations concerning temporal aliasing issues of NGGMs (Chapter 7). Table 4.2 includes the setup parameters for the integration of the dynamic orbits. The orbit integration is performed with the highest level of absolute accuracy (10^{-8}m). The orbits for the two pairs of the Bender constellation have been optimized in order to fulfill specific science requirements set up for the scopes of the "ESA-SC4MGV" project. The orbit choice was therefore optimized regarding an 11-year (full solar cycle) mission period, with the best possible spatial sampling that minimizes temporal aliasing effects and remains feasible from a technological and financial point of view. The initial osculating Kepler elements that lead to the required full and sub-cycles of the satellite orbits, were provided by TU-Delft at the frames of the project. These initial state vector parameters together with the background force models mentioned in Table 4.2 were used for the generation of the dynamic orbits. For more details about the orbit optimization procedure refer to Iran Pour et al. (2015). The ground-track spatial coverage for a sampling period that corresponds to a complete cycle of the polar pair (11 days) is depicted at Fig. 4.3.1, whereas the complete cycle of the inclined pair (29 days) is depicted at Fig. 4.3.2. The green dots

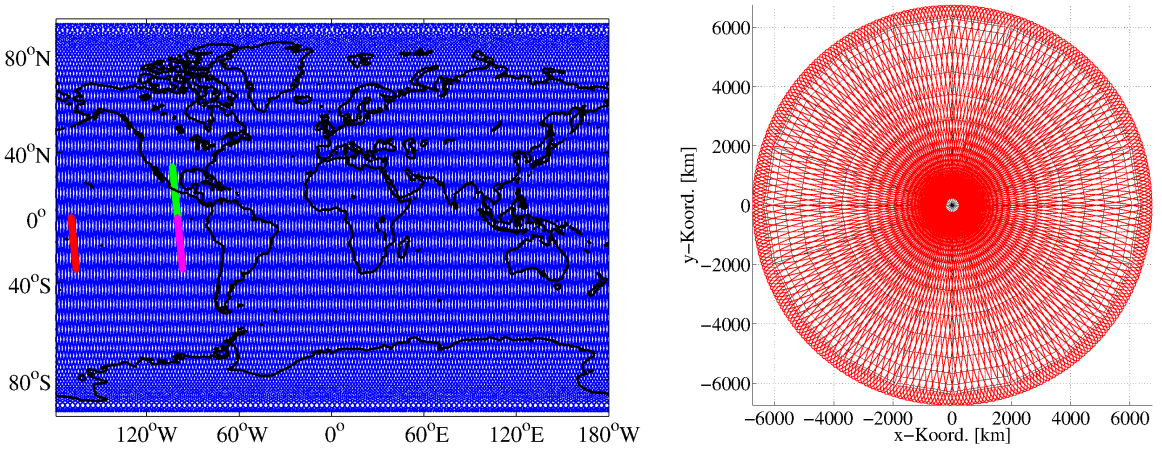

Figure 4.3.1: Spatial ground-track coverage of the near-polar pair of the Bender-type constellation for a period of a full cycle (11 days).

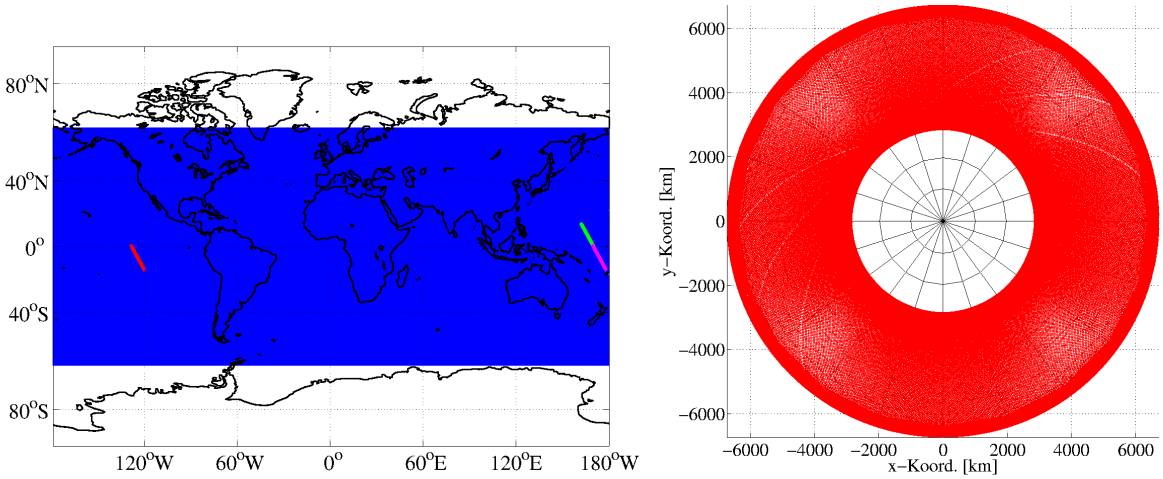

Figure 4.3.2: Spatial ground-track coverage of the inclined pair of the Bender-type constellation for a period of a full cycle (29 days).

in Figs. 4.3.1, 4.3.2-left, represent the starting ground-track positions, while the magenta and red dots the ending positions of the full-cycle and the first sub-cycle, respectively.

4.4 Science and mission requirements

The definition of the science requirements for NGGMs taking into account all the different processes of the system Earth, is a very demanding task that has been addressed extensively in many studies. ESA has funded some of them that deal with the assessment of NGGMs for monitoring the variations of Earth's gravity (ESA, 2010, 2011; Iran Pour et al., 2015). The main challenge of space gravimetry missions of a next generation, is to gain an improved understanding of the Earth's state behavior and the coupling of its

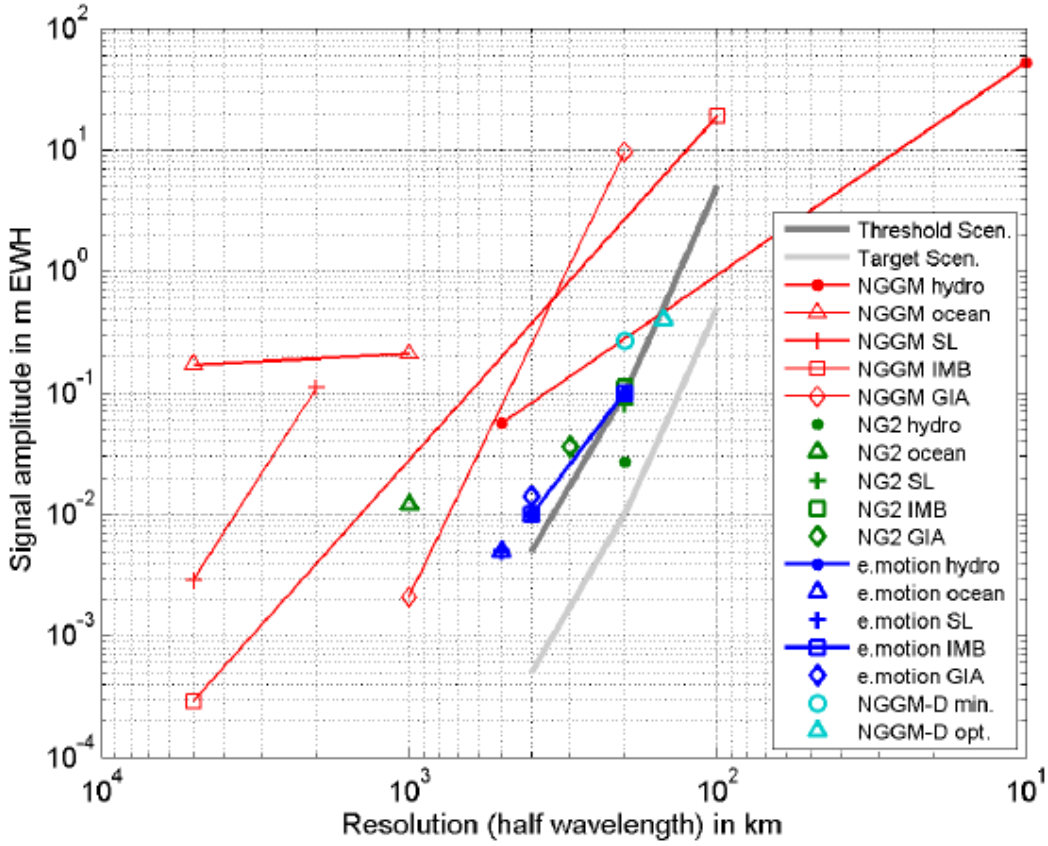

Figure 4.4.1: Science requirements derived in different studies for individual fields of applications. Red; NGGM (ESA, 2010), green; NG2 (ESA, 2011), blue; e-motion (Panet et al., 2013), cyan; NGGM-D (Gruber et al., 2014a). The light and dark grey curves represent the consolidated requirements of the target and threshold scenarios respectively defined at Pail et al. (2015). (Plot taken from Pail et al. (2015)).

dynamic processes. Fig. 4.4.1 (taken from Pail et al. (2015)) shows the science requirements defined by different studies, for the thematic fields of hydrology, sea level (SL), ice mass balance (IMB) and glacial isostatic adjustment (GIA). The requirements are given in terms of signal amplitude in equivalent water height (EWH) w.r.t. the spatial resolution. Some of those requirements are highly connected to societal needs. For example, the closing of the water balance by understanding the processes that govern the water exchange between all sub-systems, is a prerequisite for a sustainable water resource management strategy, and for the timely forecasting of floods and droughts. In the field of cryosphere, the evolution of ice sheets and glaciers is crucial for the understanding of the Earth and climate system, and thus important for the investigations about the climate change. Related to this, the ability of monitoring and predicting

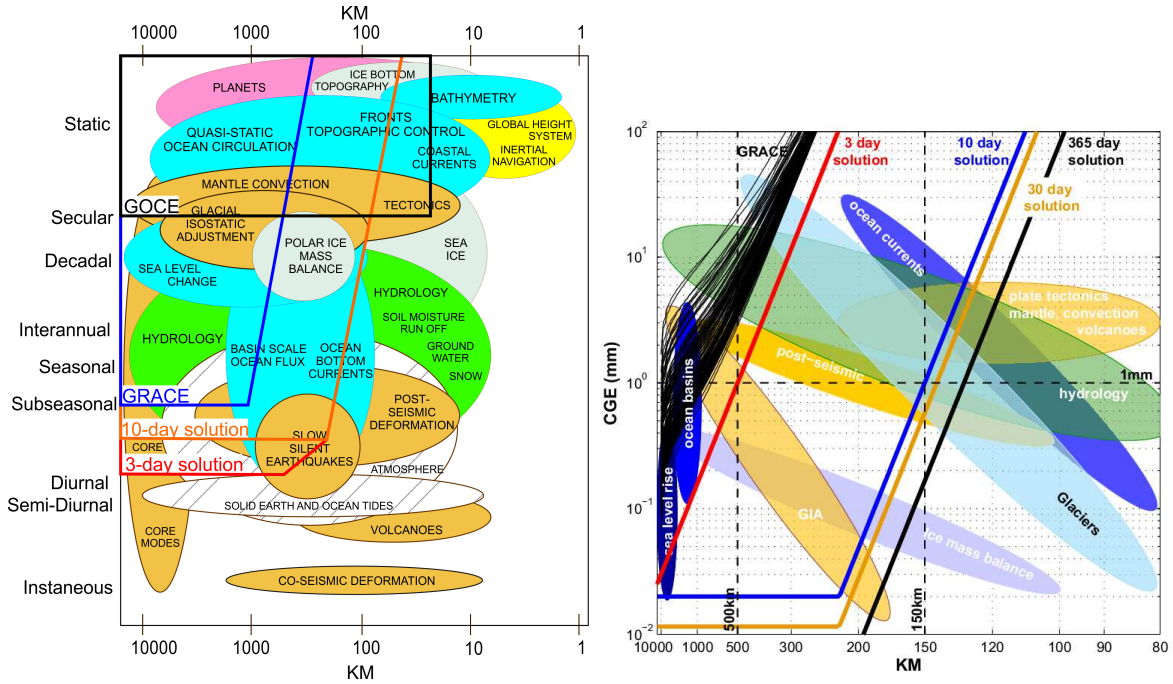

Figure 4.4.2: Anticipated performance in terms of spatial w.r.t. temporal resolution (left) and in terms of spatial w.r.t. cumulative geoid height error (right). (Plot taken from Gruber et al. (2014b)).

the sea level change by closing the sea level budget, has an important societal impact. Improvements of the accuracy of GIA models, is a very important aspect for solid Earth applications which will lead to a better understanding of its coupling with cryosphere and oceans. At last, a requirement from geodetic applications involves the global unification of height systems, which is expected to have a major impact on land management applications.

The improvements towards the state-of-the-art GRACE and GOCE achievements that are expected from a NGGM are included in the requirements for the optimization of the orbit design that are summarized in Sec. 4.1. Additionally, it can also be mentioned that higher precision is expected to be achieved by means of improvements in measuring technology. Fig. 4.4.2 (taken from Gruber et al. (2014b)) visualizes the anticipated performance of a NGGM defined in Iran Pour et al. (2015), together with the bubble plots for all the application fields. The left part of Fig. 4.4.2, shows the spatial w.r.t. the temporal resolution, where the right part shows the cumulative geoid error w.r.t. the spatial resolution. The curves with the 3-, 10-, 30- and 365-day solutions are defined from the "ESA-SC4MGV" project (Iran Pour et al., 2015) as mission requirements, where the GRACE and GOCE curves are also given as a reference. In Pail et al. (2015), an integrated investigation of all the fields of application (i.e. continental hydrology, cryosphere, ocean, atmosphere and solid Earth) concluded a required target performance of 5 cm in terms of EWH for monthly fields and 0.5 cm/year for long-term trends at spatial resolution of 150 km. That results in an improvement of the current GRACE mission performance roughly by a factor of 50, which given the accuracies of the next generation sensors in combination with optimized satellite constellations

could be a realistic goal. However, the limitations imposed from temporal aliasing issues (Murböck et al., 2014), as well as the gravity field processing itself (Daras et al., 2014), raise serious doubts on whether those accuracies can be achieved. Those limitations and strategies for their elimination are the subject of Chapters 5 and 7.

4.5 Noise models for the performance of the instruments

This section is dedicated to the description of the analytical noise models used for the simulation of the instrument performance. The stochastic models describe the behavior of state-of-the-art instruments that are similar to the accuracies of the GRACE-FO mission. The noise time series of each error source are then generated by scaling the spectrum of a normally distributed random time series according to the corresponding spectral model.

4.5.1 Laser interferometer errors

NGGMs are expected to make use of a laser interferometer as their principle inter-satellite measurement unit. Already on the GRACE-FO mission, the μm-level accurate KBR instrument will be supplemented with a 50~100 nm precise laser interferometer (Sheard et al., 2012). We assume a laser interferometer with an error behavior (Fig. 4.5.1) based on a more optimistic synthesis of the preliminary requirements from Sheard et al. (2012). The analytical model for the amplitude spectral density ($ASD = PSD^{1/2}$) is given by:

$$\left((30 \cdot 10^{-9})^2 + \frac{100Hz}{f}\left(355 \cdot 10^{-12} \cdot \frac{\rho_{avg}}{100km}\right)^2\right)^{-1/2} [m/\sqrt{Hz}], \tag{4.3}$$

with f being the frequency in Hz and ρ_{avg} the average inter-satellite distance in km. The noise time series are generated in terms of ranges or range rates (through differentiation in spectral domain) and are directly propagated to the solution through addition to the vector of the simulated pseudo-observations $\boldsymbol{\rho}$ or $\dot{\boldsymbol{\rho}}$.

4.5.2 Accelerometer errors

Each satellite is equipped with an accelerometer (ACC) which serves in measuring the non-gravitational forces acting on the satellite. The accelerometer has two sensitive and one less-sensitive axes. According to Kim (2000), for GRACE (and expectedly also for GRACE-FO) accelerometers, the sensitive axes are set to be at the along-track and radial direction, whereas the less-sensitive one at the cross-track direction. The ASD (Fig. 4.5.2) for the two sensitive axes is given by:

$$10^{-10} \cdot \left(1 + \left(\frac{10^{-4}Hz}{f}\right)^4 + \left(\frac{f}{10^{-2}Hz}\right)^4\right)^{1/2} [m/s^2/\sqrt{Hz}], \tag{4.4}$$

and for the less sensitive axis by:

$$2 \cdot 10^{-9} \cdot \left(1 + \left(\frac{10^{-4} Hz}{f}\right)^4 + \left(\frac{f}{10^{-2} Hz}\right)^4\right)^{1/2} [m/s^2/\sqrt{Hz}], \tag{4.5}$$

with f being the frequency in Hz. The noise assumptions are rather pessimistic for future LL-SST gravity missions (ESA, 2010). Noise time series of acceleration differences between the two satellites are generated for all three axes. Unlike the laser noise, the accelerometer noise is not transformed into range or range-rate noise to be directly added at the observations, instead it is propagated through the functional model into the system. It is therefore added to the modeled specific forces $\mathbf{f}^{12}$ which are then integrated in a next step (Eqs. (3.9) and (3.10)).

4.5.3 Star camera errors

Each satellite LL-SST tandem carries a Star Camera Assembly (SCA), which consists of 2 simultaneously operated star cameras, individually placed on each satellite. The star cameras are used for the precise orientation of the satellites within the attitude and orbit control system and for the correct interpretation of the accelerometer measurements. Errors in the star camera measurements lead to attitude determination errors and to uncertainties in the transformation of the non-gravitational forces from the satellite-fixed reference system to the CRF. The satellite can experience rotations around the along-track axis (roll), the cross-track axis (pitch) and the radial axis (yaw). The ASD of the analytical model for the

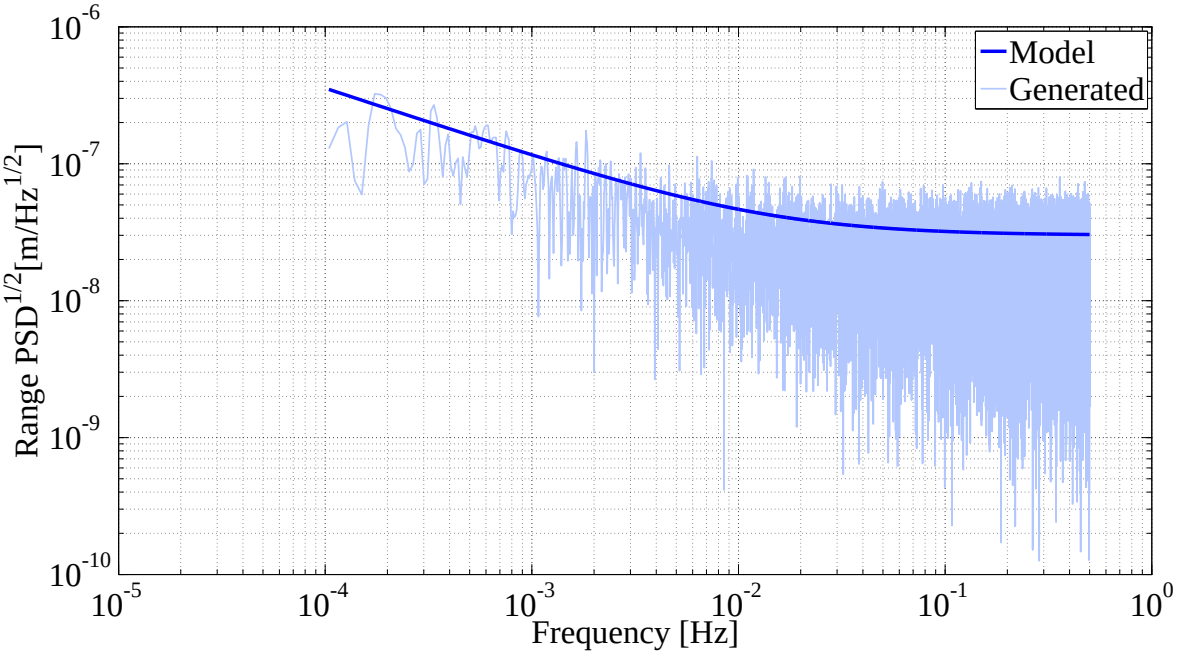

Figure 4.5.1: *ASD* of the total laser interferometer error model and of the generated inter-satellite range noise at 1 Hz sampling frequency. An average inter-satellite distance of 200 km was considered.

star sensor noise (Fig. 4.5.3) is the one used for the "ESA-SC4MGV" project (Iran Pour et al., 2015), which in terms of attitude angles for the roll rotation angle is given by:

$$10^{-5} \cdot \left(\left(\frac{10^{-3} Hz}{f} \right)^4 / \left(\left(\frac{10^{-5} Hz}{f} \right)^4 + 1 \right) + 1 \right)^{1/2} [\text{rad}/\sqrt{Hz}], \tag{4.6}$$

and for the pitch and yaw rotation angles by:

$$2 \cdot 10^{-6} \cdot \left(\left(\frac{10^{-2} Hz}{f} \right)^2 / \left(\left(\frac{10^{-5} Hz}{f} \right)^2 + 1 \right) + 1 \right)^{1/2} [\text{rad}/\sqrt{Hz}]. \tag{4.7}$$

The generated noise of attitude angles is transformed into attitude quaternion time series which are added epoch-wise to the transformation matrix of the satellite-fixed reference system to the CRF.

4.5.4 Residual drag accelerations

For reasons of orbit maintenance and formation monitoring, NGGMs will most probably fly in drag-free mode. As a consequence, the sum of the non-gravitational forces acting on the satellite will be compensated by the propulsion system. However, a complete compensation of the non-gravitational forces cannot be achieved, leading to residual drag. The accelerations caused by residual drag affect the satellite's orbit, but are also sensed and measured by the accelerometers. Being an output of the accelerometers, the residual drag accelerations are reduced from the specific forces acting on the satellite.

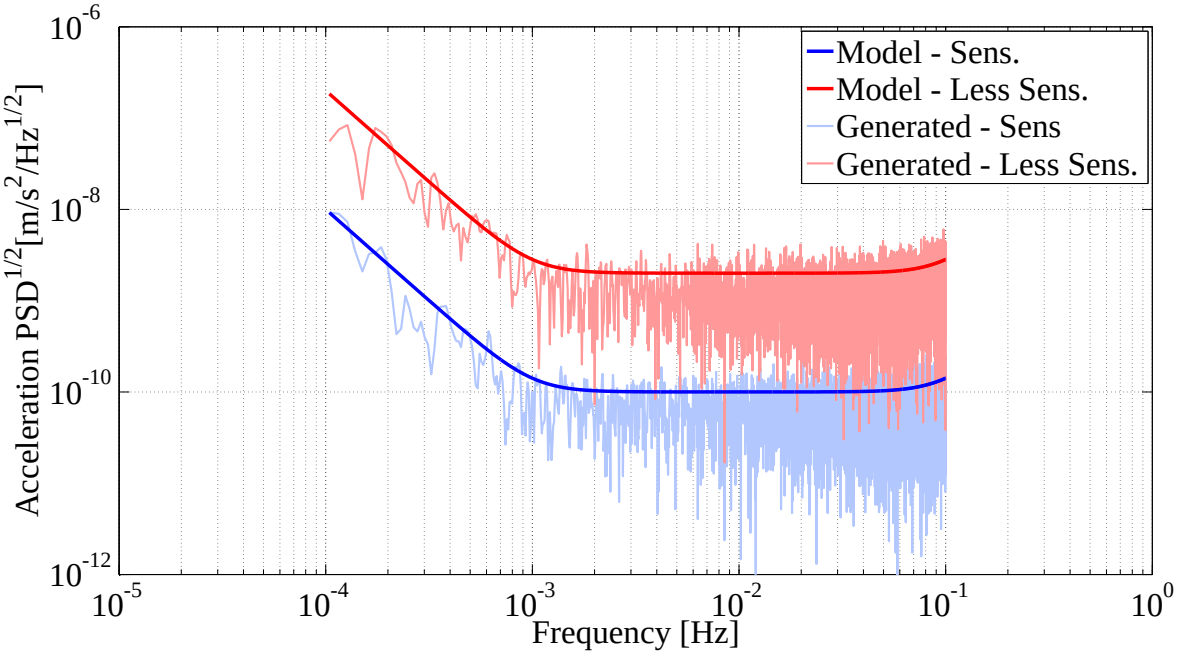

Figure 4.5.2: *ASD* of the accelerometer error model and of the corresponding generated accelerometer noise at 1 Hz sampling frequency, for the sensitive (blue) and less sensitive (red) axis.

Their effect nevertheless, can still couple with other error sources, such as the attitude errors. The ASD of the analytical model of the residual drag accelerations (Fig. 4.5.4), for the along-track component is given by (Iran Pour et al., 2015):

$$10^{-9} \cdot \left(\left(\frac{2 \cdot 10^{-4} Hz}{f} \right)^4 / \left(\left(\frac{2 \cdot 10^{-5} Hz}{f} \right)^4 + 1 \right) + 1 + \left(\frac{f}{10^{-1} Hz} \right)^4 \right)^{1/2} [m/s^2/\sqrt{Hz}], \tag{4.8}$$

for the cross-track component by:

$$10^{-9} \cdot \left(\left(\frac{4 \cdot 10^{-5} Hz}{f} \right)^4 / \left(\left(\frac{2 \cdot 10^{-5} Hz}{f} \right)^4 + 1 \right) + 1 + \left(\frac{f}{10^{-1} Hz} \right)^4 \right)^{1/2} [m/s^2/\sqrt{Hz}], \tag{4.9}$$

and for the radial component by:

$$10^{-9} \cdot \left(\left(\frac{8 \cdot 10^{-4} Hz}{f} \right)^4 / \left(\left(\frac{10^{-5} Hz}{f} \right)^4 + 1 \right) + 1 + \left(\frac{f}{10^{-1} Hz} \right)^4 \right)^{1/2} [m/s^2/\sqrt{Hz}]. \tag{4.10}$$

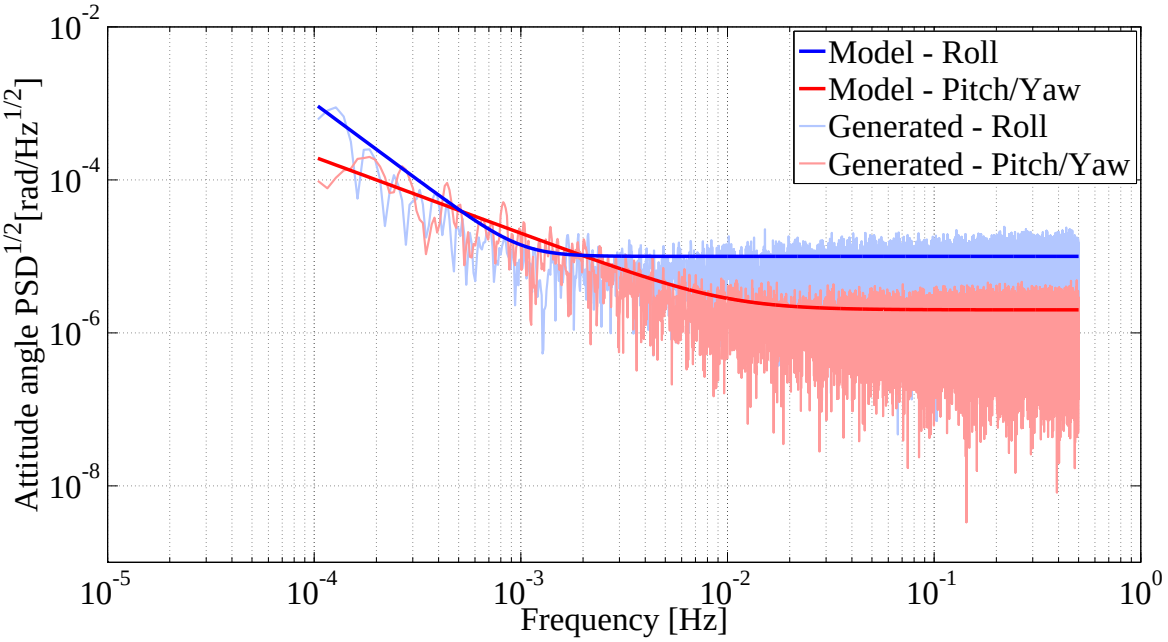

Figure 4.5.3: *ASD* of the the star camera error model and of the corresponding generated noise at 1 Hz sampling frequency, for the roll (blue), pitch and yaw (red) rotation angles.

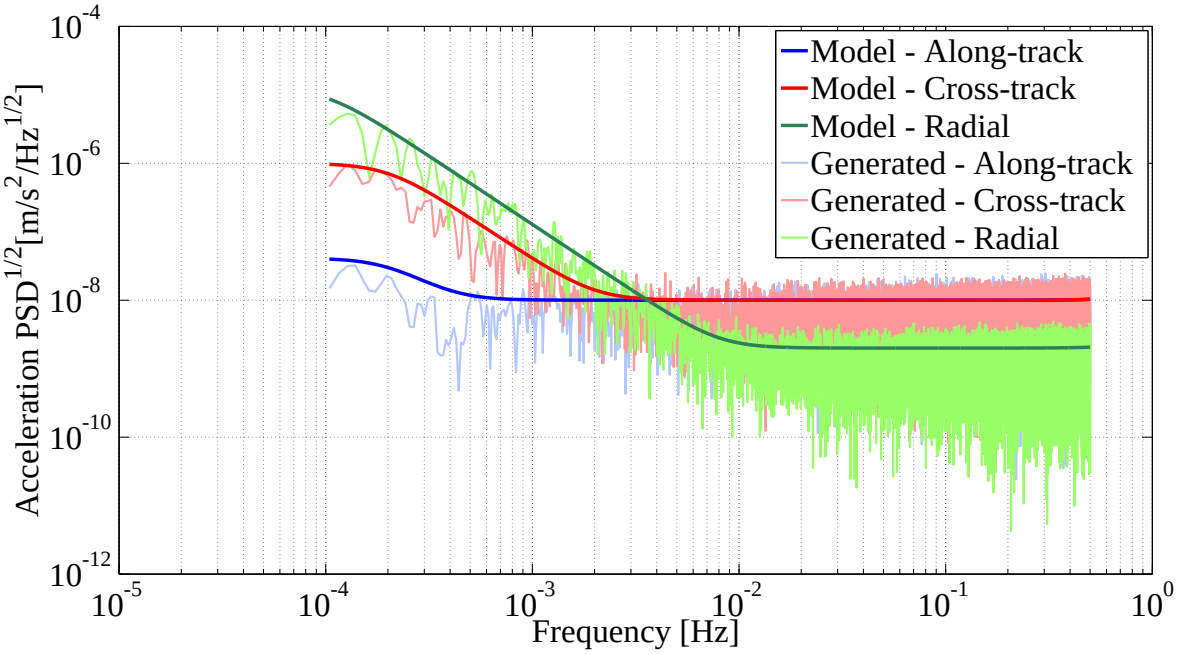

Figure 4.5.4: *ASD* of the residual drag analytical model and of the corresponding generated noise at 1 Hz sampling frequency, for the along-track (blue), cross-track (red) and radial (green) component.

4.6 Error budget analysis

Apart from the error sources that can be analytically modeled (Sec. 4.5), other error sources such as errors resulting from temporal aliasing or background model inaccuracies have a major contribution to the total error budget. The effect of each error source is determined individually by means of "closed-loop" gravity field simulations (Fig. 4.6.1). These types of simulations take their name from the comparison of the input gravity field entering the computations, with the output gravity field solution of the processing, thus forming a closed-loop comparison. The misclosure of this comparison when the processing is noise-free is a good estimate of the estimation accuracy. The input of the closed-loop simulation include the force models that represent a so-called "true" world which is used to simulate the pseudo-observations. Sensor noise generated from stochastic models can then be added to those error-free observations, in order to simulate observations that are closer to real measurements. Another set of force models comprises the "nominal" world, which is used by the functional model to compute the reference observations. Adjusting the components of the true w.r.t. the nominal world appropriately allows for estimating the contribution of specific error sources. Table 4.3 provides the description of error sources that are investigated for their effect on the gravity field estimation.

All simulations of the error budget analysis were performed using the polar pair of the Bender constellation (Table 4.1), and correspond to a solution period of one month. After experimenting with different choices of short-arc lengths (20 ~ 60 min), we were driven to the same conclusions as in Mayer-Gürr (2006); i.e., the choice of short-arc length plays a minor role in the gravity field retrieval and only for

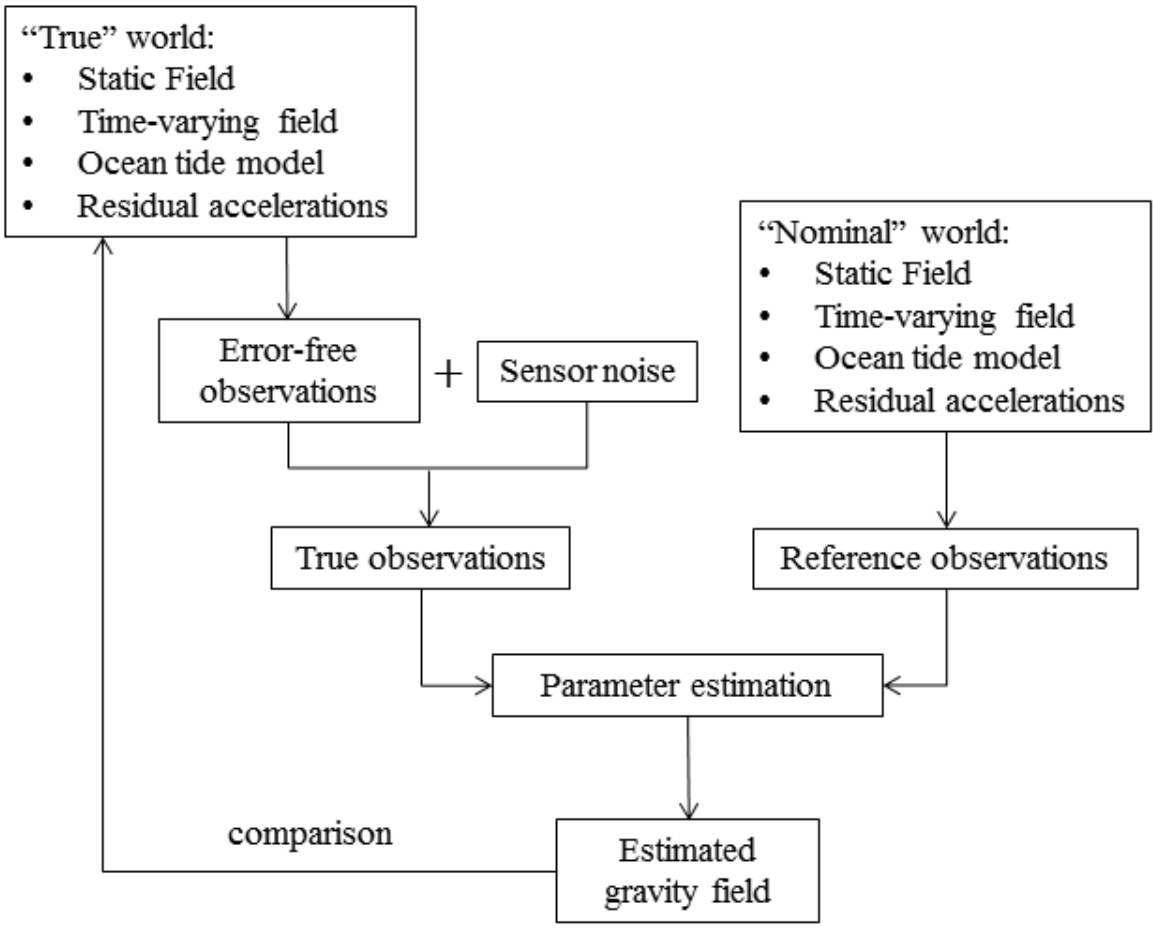

Figure 4.6.1: Closed-loop simulation scheme.

the long wavelength component. A 30 min arc length was then chosen for all the simulations performed. The results correspond to single-run simulations, and no iterations for improving the gravity field solutions have been made. There is also no empirical parameterization, or any kind of filtering applied at this stage, in order to examine the direct impact of the individual error sources to the quality of the gravity field.

In order to analyze the error budget in a consistent manner, the system accuracy has first to be determined as a basis for the comparisons. This is achieved via closed-loop simulations which use only the most dominant perturbation force, namely the static gravity field of the Earth. In that case, the static gravity field model GOCO03s, which is a satellite-only gravity field model based on GRACE, GOCE and LAGEOS (Mayer-Gürr et al., 2012), was chosen (Table 4.3). GOCO03s was used for the generation of the dynamic orbits ("true" force model), as well as for the gravity field retrieval ("nominal" force model). As a consequence, our assumption is that our gravitational force model is perfectly known. Figs. 4.6.2 and 4.6.3 display the DDA of the closed-loop simulations performed for each noise case, where

Noise case	"True" force models	max d/o (deg)	Sensor noise	"Nominal" force models	max d/o (deg)	Closed-loop misclosure St. Dev. [mm]
Error-free	GOCO03s	120	-	GOCO03s	120	$1.2 \cdot 10^{-1}$
Laser errors	GOCO03s	120	Laser	GOCO03s	120	$1.2 \cdot 10^{-1}$
ACC errors	GOCO03s	120	ACC	GOCO03s	120	$4.4 \cdot 10^{1}$
SCA errors	GOCO03s Res. acceler.	120	SCA	GOCO03s Res. acceler.	120	4
Orbit errors	GOCO03s	120	Orbits $10^{-2}m$ white noise	GOCO03s	120	$6 \cdot 10^{-1}$
Ocean tidel model errors	GOCO03s GOT4.7	120 50	-	GOCO03s EOT08a	120 50	$2.4 \cdot 10^{1}$
Temporal aliasing errors	GOCO03s AOHIS	120 120	-	GOCO03s AOHIS	120 120	$3.3 \cdot 10^{1}$
De-aliasing model errors	GOCO03s AOHIS	120 120	-	GOCO03s AO AO errors	120 120 50	$1 \cdot 10^{1}$

Table 4.3: Processing details and geoid height reconstruction errors of the noise cases.

the inter-satellite range was used as observable. In cases where the solutions contain only the effect of noise sources, the formal error curve of the input static gravity field model is depicted as reference. For GOCO03s, this corresponds to error estimates of a GRACE static gravity field, as its contribution is dominant up to d/o 120. For cases where temporal gravity field variations are used as input, their signal power averaged over one month is depicted as reference. The last column of Table 4.3 delivers the misclosures of the closed-loop simulations, in terms of standard deviations of geoid heights. Comparing Fig. 4.6.2 top-left with Fig. 4.6.2 top-right, it is evident that the retrieval error of the laser noise case is almost identical to the error-free case. The geoid height reconstruction errors for both cases have equally large standard deviation of $1.2 \cdot 10^{-1}$mm (Table 4.1). This finding, raises doubts of whether the processing accuracy is a limiting factor for exploiting the nm accuracy of a laser interferometer to its full extent. This problem is extensively addressed in Chapter 5. On the other hand, propagation of

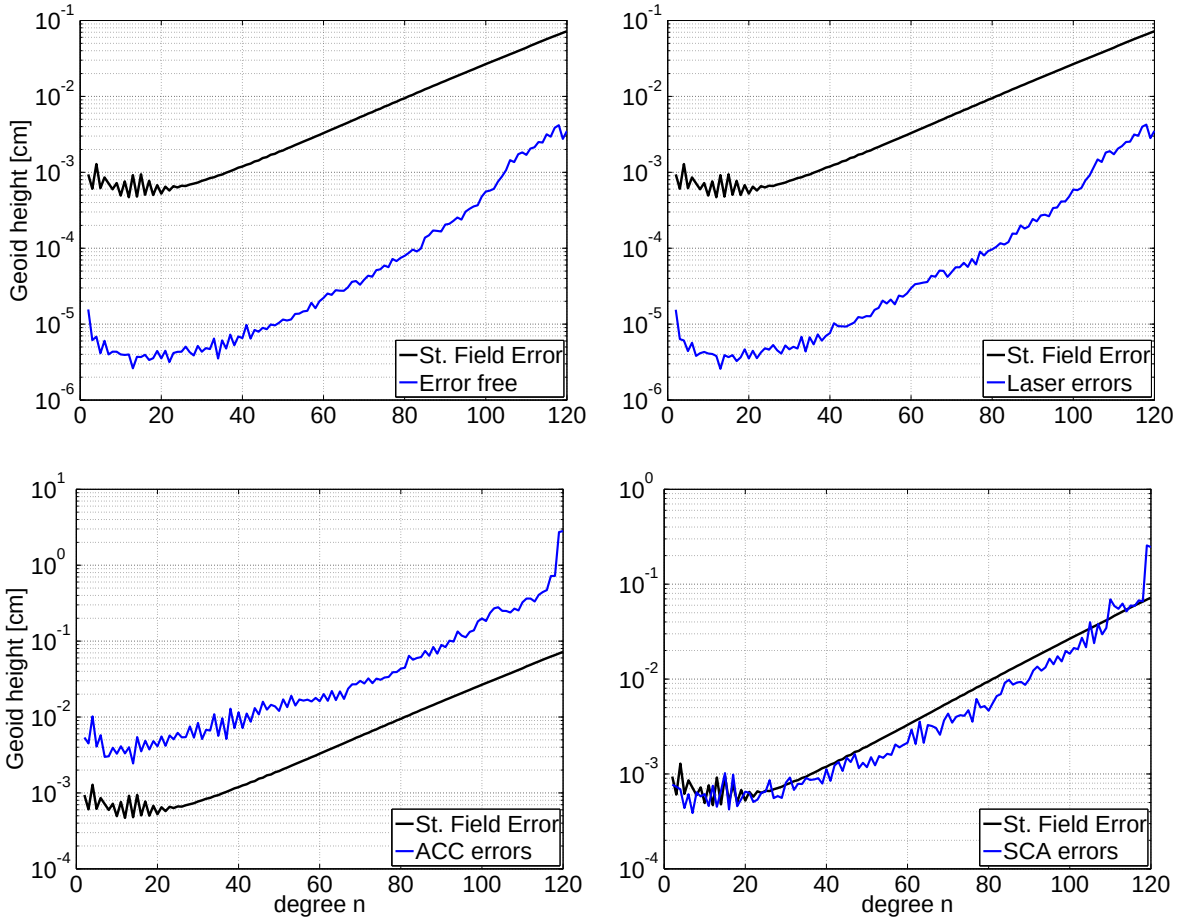

Figure 4.6.2: DDA in terms of geoid heights: Noise-free (top-left), Laser errors (top-right), ACC errors (bottom-left), SCA errors (bottom-right). The errors of the input static gravity field is depicted in black.

accelerometer errors (Fig. 4.6.2 bottom-left) lead to a considerably larger retrieval error, which certifies them as one of the most significant error sources. The treatment of accelerometer errors in the gravity field processing chain is addressed in Chapter 6.

The residual accelerations are considered during the computation of the dynamic orbits, but their effect is reduced at the gravity field processing through the reference observations. They are sensed by the accelerometers and thus are part of accelerometer observations. The non-gravitational forces measured by the accelerometers are transformed from the satellite-fixed reference system to the CRF, with use of the star camera orientation measurements which are subject to errors. Therefore, the effect of residual accelerations is coupled with the attitude errors of the star cameras. Their retrieval error is depicted at Fig. 4.6.2 bottom-right. The error levels are larger than that of the laser, but smaller than that of the accelerometer error levels and at the same level with the errors of the input static gravity field.

The impact of orbit errors on the gravity field processing was assessed by simulating the position accuracy of real kinematic orbits. This was achieved by propagating 1 cm white noise of the orbit

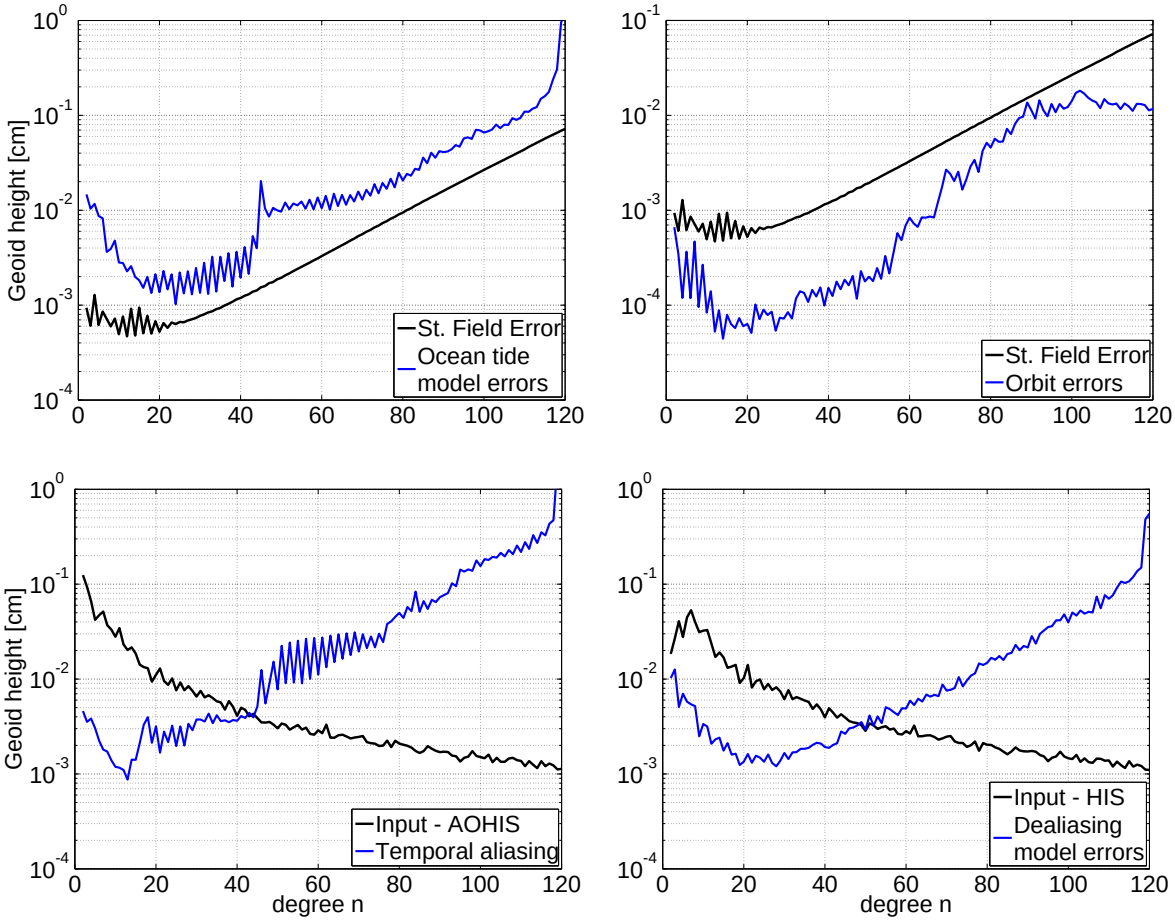

Figure 4.6.3: DDA in terms of geoid heights: Ocean tide model errors (top-left), Orbit errors (top-right), Temporal aliasing errors (bottom-left), De-aliasing model errors (bottom-right). The errors of the input static gravity field (top) and the corresponding input gravity fields (bottom) are depicted in black.

positions of each satellite. For the HL-SST part of the NEQ system, the erroneous orbits served as computational points for the reference values as well as actual observations. On the contrary, error-free dynamic orbits were used as computational points for the reference values of the LL-SST part, in order to maintain the inter-satellite measuring accuracy of a laser instrument. A relative weighting between the HL-SST and the LL-SST part was also applied, with a σ_0 of 1 cm and 10 μm used correspondingly. Fig. 4.6.3 top-right depicts the retrieval error due to errors of the kinematic orbits.

One of the most significant error sources is temporal aliasing. Temporal aliasing occurs when high frequency signals alias into the mean gravity field solutions. The *Nyquist* sampling theorem dictates that a signal with f_s sampling rate can be fully reconstructed only when it is band-limited at $B \leq f_s/2$, where $f_s/2$ is the so-called *Nyquist frequency*. Equivalently, a geophysical signal with a period more than twice the sampling period of the gravity field retrieval, can be perfectly reconstructed. In case of temporal variations of Earth's gravity field retrieved in monthly or even shorter time periods, geophysical signals with periods smaller than the Nyquist frequency unavoidably alias into the solutions. Temporal aliasing

mainly results from the following:

- under-sampling of signal of interest (e.g. hydrology),
- errors of de-aliasing models (usually atmosphere and ocean),
- errors of ocean tide models.

Next, the impact of the temporal aliasing error sources is analyzed individually. Chapter 7 focuses on gravity field processing techniques that minimize the overall temporal aliasing.

Fig. 4.6.3 bottom-left shows the impact of temporal aliasing that results from under-sampling of the main geophysical processes of system Earth. Their signal power averaged over the retrieval period is depicted in black in Fig. 4.6.3. Their time-varying gravity field changes are estimated from the updated Earth System Model of ESA (Dobslaw et al., 2015). Those models are provided with a temporal resolution of 6 hours, and are used as input in the generation of the dynamic orbits (Table 4.3). The values between the 6-hourly snapshots are estimated by piece-wise linear interpolation. The integrated effect of all processes has the abbreviation "AOHIS". It consists of the individual components of atmosphere ("A"), ocean ("O"), hydrology ("H"), ice ("I") and solid Earth ("S"), which are also separately available. Inspecting Fig. 4.6.3 bottom-left, confirms the severity of temporal aliasing due to under-sampling of signals which is also typical for the GRACE mission. In fact, the Signal-to-Noise Ratio (SNR) is smaller than 1 for degrees higher than 40, which is also the cause of the meridional-oriented striping features that are present in GRACE gravity fields of a higher expansion.

GRACE gravity field processing typically makes use of high-frequency non-tidal models of atmosphere and ocean (Dobslaw et al., 2013), in order to de-alias the gravity field solution from those signals. The final product contains the integrated effect of hydrology ("H"), ice ("I" and solid earth ("S"). The de-aliasing models are subject to errors, and the reduction of the high-frequency signals is inaccurate. This results in temporal aliasing effects. For the scope of the "ESA-SC4MGV" project (Iran Pour et al., 2015) an error model for the atmospheric and oceanic part ("AO") de-aliasing models has been estimated. The "AO" error model was synthesized empirically, by combining a signal and a random part. The signal part served to maintain the spatial and temporal signal properties of the "AO" models. The signal dependent part is 10% of the full "AO" signal, while the random part is scaled in a way that the RMS value of each spherical harmonic coefficient is equal to 5% of the corresponding RMS value of the full signal. Fig. 4.6.3 bottom-right depicts the retrieval errors due to the errors of the de-aliasing models. The signal power of the corresponding averaged "HIS" field is plotted in black for reasons of comparison. The SNR this time, remains larger than 1 until d/o 50.

Ocean, solid earth and direct tidal signals are routinely reduced from the observations during the gravity field estimation, via use of models. These models contain errors, which are difficult to be accurately quantified. We assessed the impact of ocean tides model errors, as the tidal model with the largest contribution to the error budget. The difference of two independently produced tide models (GOT4.7 and EOT08a) was taken as an estimate of their error behavior. The model discrepancies are indirectly

propagated into the gravity field solution by using one model to generate the “true”, and the other the “reference” observations (Table 4.3). The GOT4.7 model is an empirical ocean tide model (from the GOT series (Ray, 1999)) based on altimetric data from missions such as TOPEX/POSEIDON, Jason-1, ERS and GFO. The EOT08a model (Savcenko and Bosch, 2008) is also an empirical ocean tide model, with corrections to the FES2004 model based on analysis of 15 years of altimetric data. As shown in Fig. 4.6.3 top-left, the retrieval error due to the ocean tide model errors are quite significant.

Chapter 5

Gravity field processing with enhanced numerical precision

Future gravity satellite missions of a LL-SST-type expect to use the state-of-the-art technology for the inter-satellite measuring unit; namely laser interferometry. In Sec. 4.6, the error budget analysis revealed that gravity field processing with LL-SST measurements from a laser interferometer delivers results at the limits of processing accuracy. It was also demonstrated that all other error sources are by far larger contributors to the error budget. Already on the GRACE-FO mission scheduled to launch in August 2017 (Flechtner et al., 2014a), an LRI will complement the KBR instrument. However, LRI's enhanced accuracy might prove redundant, in the presence of processing limitations and other sources of error. Those limitations have to be dealt with and be taken into account in designing NGGMs. For this purpose, Chapters 6, 7 analyze the treatment of other error sources during gravity field processing, towards a better exploitation of the laser precision. This section focuses on overcoming the numerical accuracy constraints, when it comes to processing of laser measurements. The results are based on the investigations performed in Daras et al. (2014).

5.1 Concept of enhanced numerical precision

In an ideal error-free scenario, the error budget will be dominated by processing errors which present themselves as linearization errors, numerical integration errors, errors of the a priori values and round-off errors among others. Apart from the imprecise a priori values, all other sources of processing errors are increased by the presence of round-off errors at arithmetic operations. Round-off errors could be a limiting factor when working with very precise measurements such as inter-satellite ranges measured with a nm precise laser interferometer. Arithmetic operations with ranges performed with standard double precision processing will exhibit round-off errors at the 15th significant digit (9th digit after the decimal point) given an inter-satellite distance on the order of $10^5 m$. There lies the accuracy limit of a nanometer precise laser interferometer. The product after the arithmetic operation is therefore already

contaminated with round-off errors and the full capability of the laser interferometer remains unexplored. Moreover, the round-off errors accumulate with the calculations and the result deviates further from the "truth" value.

A solution at this point would be to explore the benefits that processing with extended precision can offer. In computer science, precision of a numerical quantity is measured in bits, or alternatively, in decimal digits. *Extended precision* provides a greater precision through a wider exponent range compared to the basic floating-point formats. Floating-point number representation specifies the encoding of a number as a string of digits that can be used by computers. *Double precision* is the basic floating-point format which is nowadays commonly used on PCs. According to the IEEE 754 standard, double precision occupies 8 bytes (64 bits) in computer memory from which the sign bit requires 1 bit, the exponent width 11 bits and the *significand* precision 52 bits. The significand is the part of the floating-point number that consists of the significant digits. A greater precision than double, can be achieved by means of *double-extended*, *double-double* and *quadruple precision*. The double-extended precision format is supported by some processors (i.e. IA32, x86-64 and Itanium) and it occupies 80 bits with a 64-bit significand. Quadruple precision is a format that occupies 16 bytes (128 bits) in computer memory from which the sign bit requires 1 bit, the exponent width 15 bits and the singificand precision 112 bits. This is translated to a 33 to 36 significant decimal digits precision, where for double precision that ranges between 15 and 17. An even greater precision by demand, can be achieved by the *arbitrary precision* floating-point arithmetic, where the variable-length significands are sized depending on how the calculation proceeds. In Ettl (2013), special libraries were used in order to allow for the accuracy of numerical solutions of the equations of motion to be a selectable option.

In this study, we chose to incorporate quadruple precision in our software, even though that might be an overshooting of the problem. Our choice was made for the sake of simplicity, as it was directly applicable in our software which comprises Fortran subroutines. We conducted also some other experiments with arbitrary precision arithmetic which proved to be computationally less efficient. A version of our software (see Sec. 5.2) introduces a hybrid processing scheme, which uses double and quadruple precision in different parts of the processing chain. Since both double and extended (quadruple) precision are used, we use the term *enhanced precision* to describe the processing accuracy.

In case of processing with quadruple precision, due to the precision boost to 33 significant digits, round-off errors will manifest themselves at a much further digit, allowing precise calculations with laser measurements. Fig. 5.1.1 demonstrates this example for ranges measured with KBR and laser, considering an inter-satellite distance of approximately 105km. It is obvious that round-off errors are much more harmful in case of laser measurements. A useful remark could also be that a range-rate observation holds more digits after the decimal point than a range, due its smaller quantity. That allows for more precise calculations during the reduction of the observations, which is a subtraction of two large numbers.

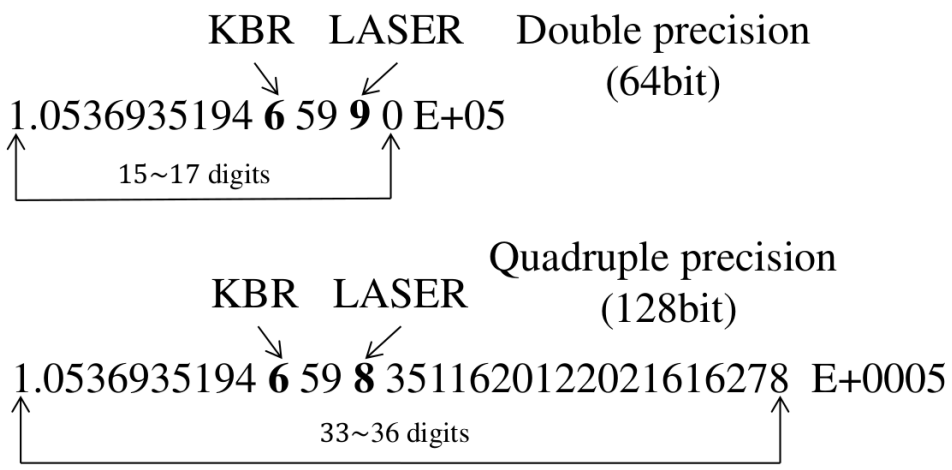

Figure 5.1.1: Exhibition of round-off errors at arithmetic operations with ranges for double and quadruple precision

5.2 Usage of enhanced numerical precision in the gravity field processing chain

As described in Sec 3.1, our processing scheme can be divided into three main individual parts; the orbit simulation, the setup of normal equations (NEQs) and the combination/solution of NEQs. In order to take advantage of the benefits that quadruple precision offers, we created two more main versions of our simulator (Table 5.1) in addition to the standard version:

Version 1 (DP)

Version 1 is the standard version where double precision (DP) is being used at all stages. For the simulation of the dynamic orbits we use the highest level of absolute accuracy for the integration (10^{-8}m). Version 1 was used for all the simulations performed in Chapters 4, 6 and 7.

Version 2 (EP)

Version 2 of the simulator uses double and quadruple precision in different parts of the processing. Therefore, we call the processing with Version 2, processing with enhanced precision (EP). The orbit simulation part now performs in quadruple precision, giving us the opportunity to raise the absolute accuracy level to 10^{-15}m. The second processing part "Setup of NEQs", where the system of equations is formulated through the functional model, performs in quadruple precision until the point where computationally expensive matrix-to-matrix multiplications take place. At this point, highly optimized linear algebra libraries BLAS/LAPACK are called to perform the operations for computing the reference parameters $\mathbf{r}_0^{12}$, $\boldsymbol{\rho}_0$ and $\dot{\boldsymbol{\rho}}_0$, for reasons of computational efficiency. Since BLAS/LAPACK libraries

work only in double precision arithmetic, our quadruple precision arguments experience a cut-off and a rounding to double precision before they enter those subroutines. The big advantage is, that until this stage quadruple precision has been maintained. This means that all the quantities in Eq. (3.9) including $\mathbf{r}_A^{12}$, $\mathbf{r}_B^{12}$ and $\mathbf{f}^{12}$ used as input for the computation of the reference parameters are computed in quadruple precision. This results in a much smaller accumulation of round-off errors from previous calculations, compared to double precision processing. From that point onward, the matrix-to-matrix operations with BLAS/LAPACK libraries are performed in double precision and the NEQs are saved in this format accordingly. The last processing part "Combination/Solution of NEQs" performs completely in double precision, since the BLAS/LAPACK libraries are used extensively.

Version 3 (QP)

Version 3 of the simulator performs completely in quadruple precision (QP). To achieve this, we replaced BLAS/LAPACK libraries with a special version of linear algebra libraries working in quadruple precision from the Numerical Algorithms Group (NAG).

In order to investigate more thoroughly the effect of quadruple precision at the different stages of the processing, an alternative of Version 1 and 2 was generated (Table 5.1):

Version 1 (alternative)

This version differs from Version 1 only in part of orbit simulation. The dynamic orbits are simulated in quadruple precision with an absolute accuracy level equal to 10^{-15}m. This version was created in order to explore the benefits of using very precise simulated orbits as computational points for the reference values $\mathbf{r}_0$ and ρ_0.

Version 2 (alternative)

This version differs from Version 2 only at the part of orbit simulation. The dynamic orbits are simulated in double precision with an absolute accuracy level equal to 10^{-8}m. This version was created in order to explore the benefits of using enhanced precision at the stage of setting up the NEQs.

Versions	Orbit simulation	Setup of NEQs	Combination/Solution of NEQs
Version 1 (DP)	Double precision abs. accuracy 10^{-8}m	Everything including BLAS/LAPACK libraries in double precision	Everything including BLAS/LAPACK libraries in double precision
Version 1 Altern.	Quad. precision abs. accuracy 10^{-15}m	Everything including BLAS/LAPACK libraries in double precision	Everything including BLAS/LAPACK libraries in double precision
Version 2 (EP)	Quad. precision abs. accuracy 10^{-15}m	Everything in quad. precision except for BLAS/LAPACK libraries in double precision	Everything including BLAS/LAPACK libraries in double precision
Version 2 Altern.	Double precision abs. accuracy 10^{-8}m	Everything in quad. precision except for BLAS/LAPACK libraries in double precision	Everything including BLAS/LAPACK libraries in double precision
Version 3 (QP)	Quad. precision abs. accuracy 10^{-15}m	Everything including NAG libraries in quad. precision	Everything including NAG libraries in quad. precision

Table 5.1: Different versions of the simulator

5.3 Benefits of processing with enhanced numerical precision

This section is dedicated to investigations concerning the impact of processing with different numerical accuracies to the gravity field recovery. At first, the effect of processing with enhanced precision in different parts of the gravity field processing chain is analyzed. For this purpose, an error-free scenario was chosen for the simulations. The first part of the simulations is the dynamic orbit determination. As discussed in Sec 3.3 the quality of the satellite orbits plays a crucial role for the precision of the gravity field retrieval. In a simulation environment, the orbits are used implicitly as computational points for the computation of the reference parameters, as well as explicitly, for the computation of the HL-SST and LL-SST pseudo-observations. In real processing, the HL-SST and LL-SST are provided by external measurements. The kinematic orbits though, being erroneous, cannot be directly used for the estimation

of reference parameters. Especially in case of the LL-SST part, the precise inter-satellite measurements would be severely contaminated by the reduction of the erroneous reference values. In this case, a solution could be to use smoother dynamic orbits instead of the kinematic orbits for the estimation of the reference parameters. Another solution would be to use the kinematic orbits as starting evaluation points ($\mathbf{r}(\tau')$ in Eq. 3.9) and let an iterative process through the functional model lead to more accurate values. Mayer-Gürr (2006) gives a general solution to the problem, by establishing a gradient correction term to the functional model, which is estimated by a static gravity field of a very small expansion (n=2). All the above solutions have in common the constraining of the system towards a priori known gravity field models.

In order to keep our error-free scenario unaffected from inaccuracies of external measurements, we assumed "perfect" HL-SST and LL-SST pseudo-observations using the most precise orbits simulated with Version 2 in quadruple precision. This was not the case with the simulations of Sec. 4.6 which were completely performed with Version 1 of the simulator, and the pseudo-observations were generated using orbits simulated in double precision. For exploring the benefits of enhanced precision processing at the computation of the reference values, we used as computational points error-free orbits simulated with Version 1 and 2 of the simulator, which will be called "reference orbits" from now on. Simulations were performed using ranges and range rates individually as an observable type.

Examining the pre-fit residuals of the "observed" (e.g. ρ and $\dot{\rho}$) minus "reference" (e.g. ρ_0, $\dot{\rho}_0$) values gives always a good indication for the quality of the processing. The spectral analysis of the pre-fit residuals, helps to distinguish the frequencies that are affected by specific error sources, and to draw conclusions for their contributors to the system noise budget. Fig. 5.3.1-top depicts the ASD of the pre-fit residuals covering one month of data, and Fig. 5.3.1-bottom the corresponding DDA in geoid heights, for the inter-satellite ranges and range rates of the LL-SST part. The blue and cyan curves are simulated with the alternative versions 1 and 2. Comparing blue with red and green with cyan curves, shows the improvement at the computation of reference values by using precisely simulated reference orbits processed with Version 2. Comparing blue with green and red with cyan curves, shows the improvement stemming from computing the elements of the design matrix with enhanced precision (Version 2). Processing with the alternative Version 1 (blue curve), produces error levels that are considerably lower compared to Version 1 (red curve). This improvement stems from the use of reference orbits simulated at a higher precision. Processing with the alternative Version 2 (cyan curve), produces error levels that are considerably larger compared to Version 2 (green curve), and at the same level with Version 1 (red curve). The gain of processing with enhanced precision is, therefore, diminished by the imprecise orbits simulated with double precision. The afore-mentioned findings are true both for ranges and range rate observable types. Through these comparisons, it is evident that the precision of the reference orbits is a crucial parameter that could pose restrictions in exploiting the enhanced precision of the calculations to its full extent. It is also worth noticing that for the inter-satellite ranges there is an accuracy limit of $10^{-10}m/\sqrt{Hz}$ which appears like a "white" noise of that amplitude on the ASD of the pre-fit residuals. This occurs in the best case scenario (green curve) where all simulation parts are processed with enhanced

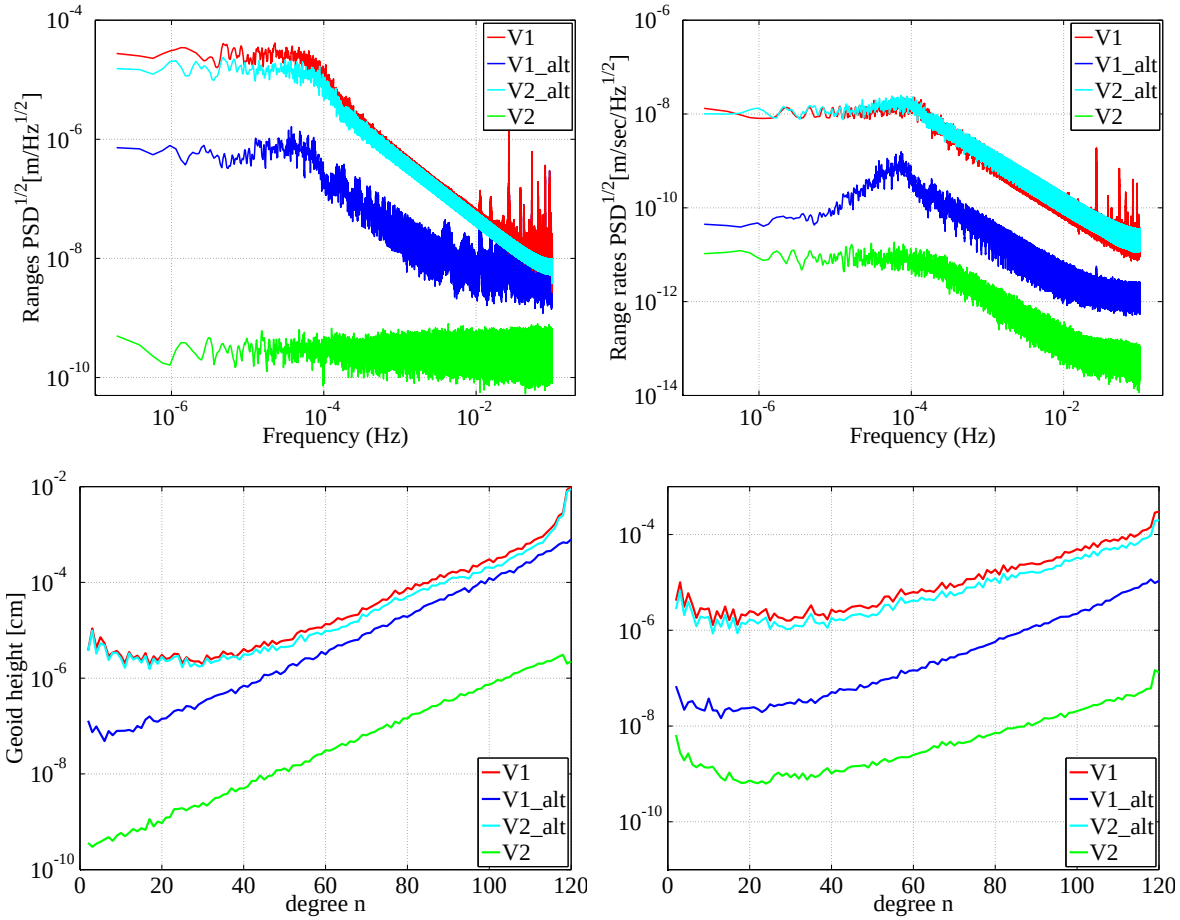

Figure 5.3.1: Top: ASD of pre-fit residuals for the inter-satellite ranges ρ (top-left) and range rates $\dot{\rho}$ (top-right) of d/o 120 solutions. Bottom: The corresponding DDA in geoid heights. The legend provides information on the simulator version (see Table 5.1) which was used.

precision by Version 2 of the simulator. The reason behind this, is the rounding from quadruple to double precision that takes place for the arguments entering the LAPACK/BLAS linear algebra libraries during the computation of the reference values at the second part "Setup of NEQs" of the processing. Therefore despite delivering a much more precise solution, the corresponding ASD from processing with Version 2 does not represent the true spectra of the residuals. However, it has a big advantage compared to Version 1, as demonstrated in the following.

Fig. 5.3.2 depicts the closed-loop simulation results in terms of geoid height differences for Versions 1 and 2. For both cases, "perfect" observations were assumed, using the most precise orbits simulated with Version 2. The reference orbits were simulated according to the versions they are subjected to (i.e., (a) with Version 1, and (b) with Version 2). Processing with enhanced precision delivers a much more precise solution both for ranges and range rates, revealed by the geoid height difference plots. The standard deviation of the geoid height differences in case of ranges improve from $1.2 \times 10^{2}\,\mu m$ to $5.4 \times 10^{-1}\,\mu m$, and in case of range rates from $3.4 \times 10^{1}\,\mu m$ to $2.1 \times 10^{-2}\,\mu m$. It is also worth noticing

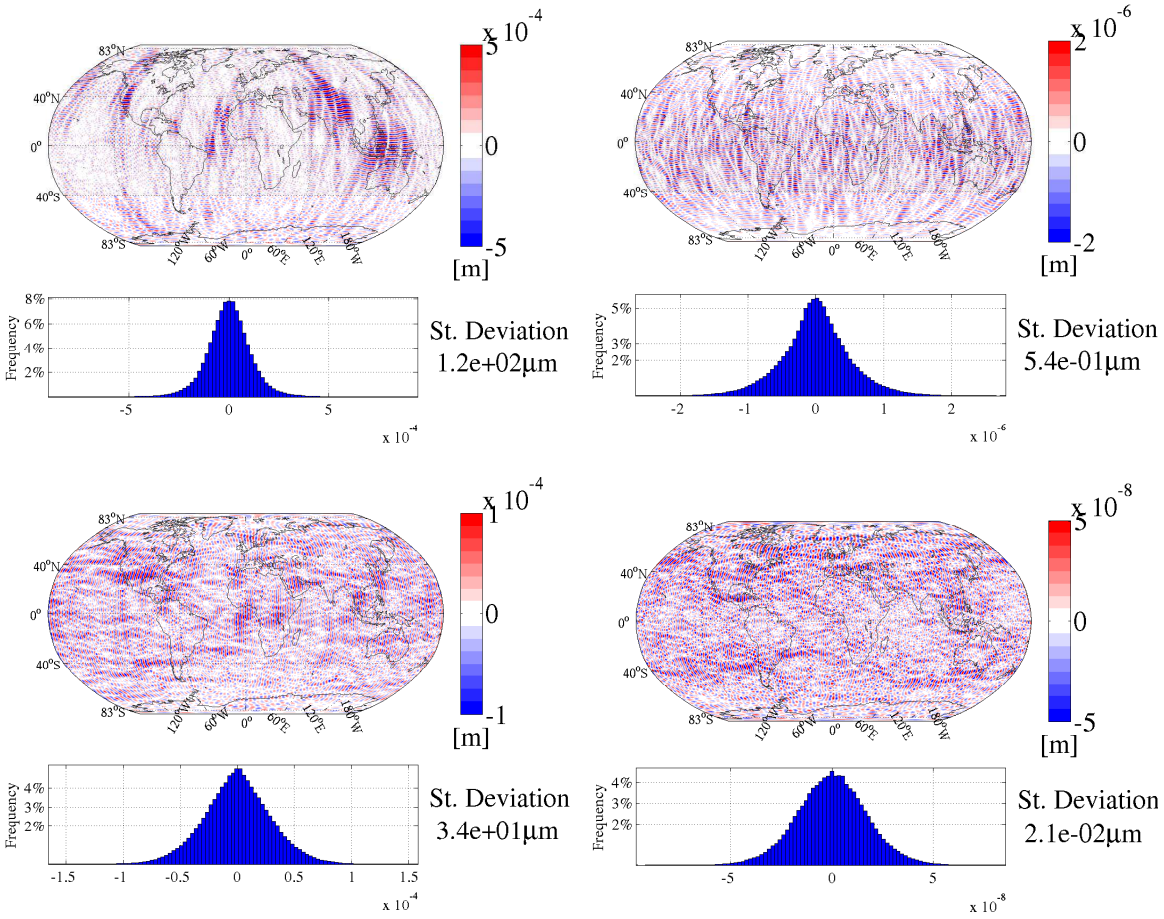

(a) Version 1 – Double precision

(b) Version 2 – Enhanced precision

Figure 5.3.2: Closed-loop geoid height differences of d/o 120 error-free simulations for ranges (top) and range rates(bottom).

that the closed-loop discrepancies shown in Fig. 5.3.2 follow a normal distribution, which is a result of the processing errors. The computational time when processing with Version 2 in enhanced precision increased by a factor of 3 compared to Version 1, which is still considered within reasonable levels for full scale gravity field processing.

Version 3 was used for performing only a simulation run for comparison reasons. Due to computational time issues caused by the very expensive computations in quadruple precision, a resolution with max d/o 70 was chosen for this simulation. Fig. 5.3.3 and Fig. 5.3.4 summarize the results of a d/o 70 error-free scenario for ranges, from all three versions of the simulator. A relative improvement between the versions explained by the gain in numerical precision, can be easily visualized. Version 2 performs approximately 10^3 times better than Version 1, when Version 3 10^4 times better than Version 2 and thus 10^7 better than Version 1. Moreover, one can notice a similar error behavior scaled roughly by a factor of 10^6 between Version 1 and Version 3, in terms of ASD of pre-fit residuals and DDA (Fig. 5.3.3). In spite

of the significant improvements that it delivers, Version's 3 great computational demands would place it as an unfavorable candidate for real gravity field processing, where computations are elaborated in a more complex environment. It is therefore presented in this study for reasons of relative comparisons of the gravity field retrieval in the presence of processing with extended precision, and not as a proposal for real processing of future satellite gravity field missions.

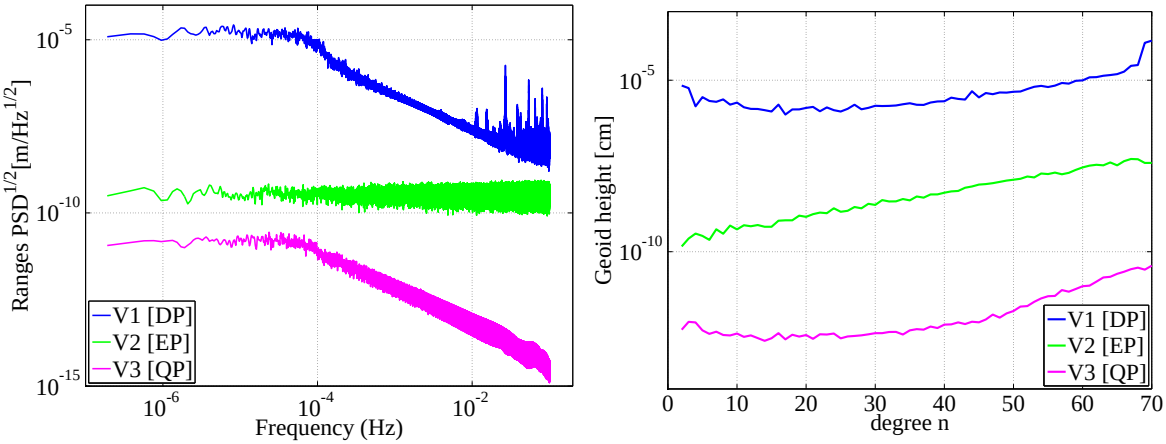

Figure 5.3.3: ASD of LL-SST pre-fit residuals (left) and DDA in geoid heights (right) of d/o 70 solutions for ranges.

After the error-free simulations, it is investigated if the enhanced numerical precision processing can contribute to a reduction of the error level in the presence of laser interferometer errors. The results from an error-free and a laser error case processed with Version 1 and 2 of the simulator are presented in Fig. 5.3.5 for ranges, and 5.3.6 for range-rates. From a quick visualization of the pre-fit residual ASD performed with Version 1 (Fig. 5.3.5 and Fig. 5.3.6 - left) it is evident that the error curves from the laser noise case (in black), at the most significant part of the bandwidth, coincide with the ones from the error-free case (in blue). The black curves exceed the blue ones only in the higher frequencies. This does not seem to be transferred to the final result of the gravity field, as the black curves of the corresponding DDA values of the closed loop simulations almost coincide with the blue ones. This indicates that the processing errors are at least equal or larger than the errors resulting from the laser noise propagation. In other words, measuring with a laser interferometer may deliver more accurate gravity field solutions than the system accuracy could handle. This hypothesis is confirmed by the simulation results from Version 2 (Fig. 5.3.5 and 5.3.6 - right). The system accuracy boosted by the enhanced precision processing, results in error-free curves that are substantially lower than the laser error curves. Therefore, contrary to Version 1, processing with Version 2 in presence of laser errors can efficiently handle precise laser inter-satellite measurements and take full advantage of their accuracy.

Our investigations concern an ideal case scenario which remains unaffected by external error sources other than the inter-satellite laser sensor errors. In a realistic scenario where imprecise kinematic orbits are used, the improvements from processing with enhanced precision could be severly moderated. How-

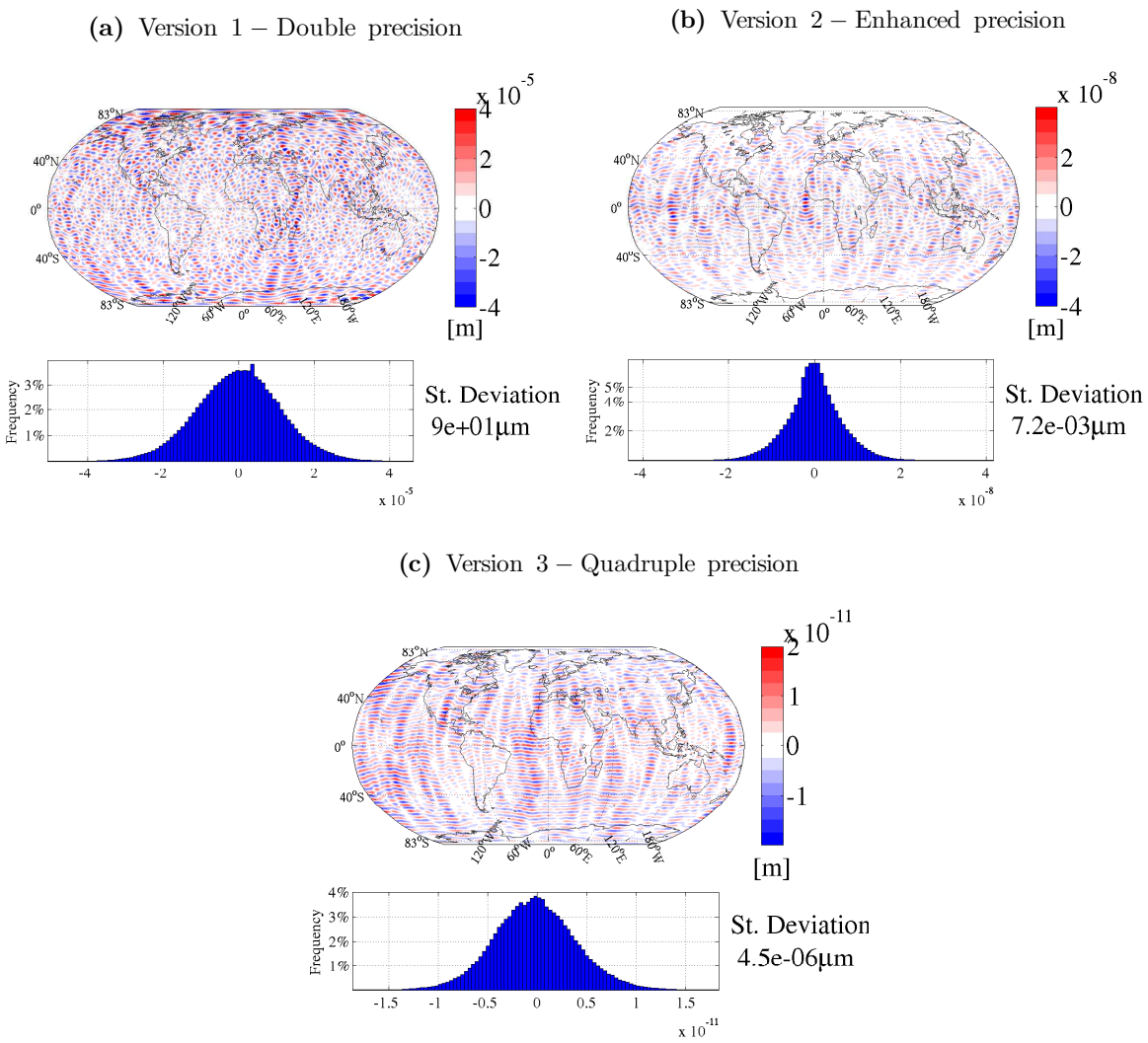

Figure 5.3.4: Closed-loop geoid height differences of d/o 70 error-free closed-loop simulations for ranges

ever, there are cases were processing with enhanced precision can be indeed helpful, or even crucial for a full exploitation of the laser accuracy. For example, in case of employing dynamic orbits as reference orbits for the computation of the reference values of the LL-SST part, processing with enhanced precision offers the advantages already discussed. In case of using kinematic orbits as starting Taylor points in an iterative procedure for estimating the reference values, enhanced precision is expected to minimize the linearization errors and lead to a faster convergence. Even when the gradient correction approach (Mayer-Gürr, 2006) is applied, the error levels from standard precision processing can still be larger than the error levels from the laser error propagation. Enhanced precision processing could therefore also in that case be necessary. On the other hand, the sum of all other error sources (Sec. 4.6) will still lead to larger retrieval errors than the laser errors. Nevertheless, the usage of better metrology, more advanced SFF constellations and improved gravity field processing techniques, may establish the usage

of enhanced precision gravity field processing for NGGMs as a necessity.

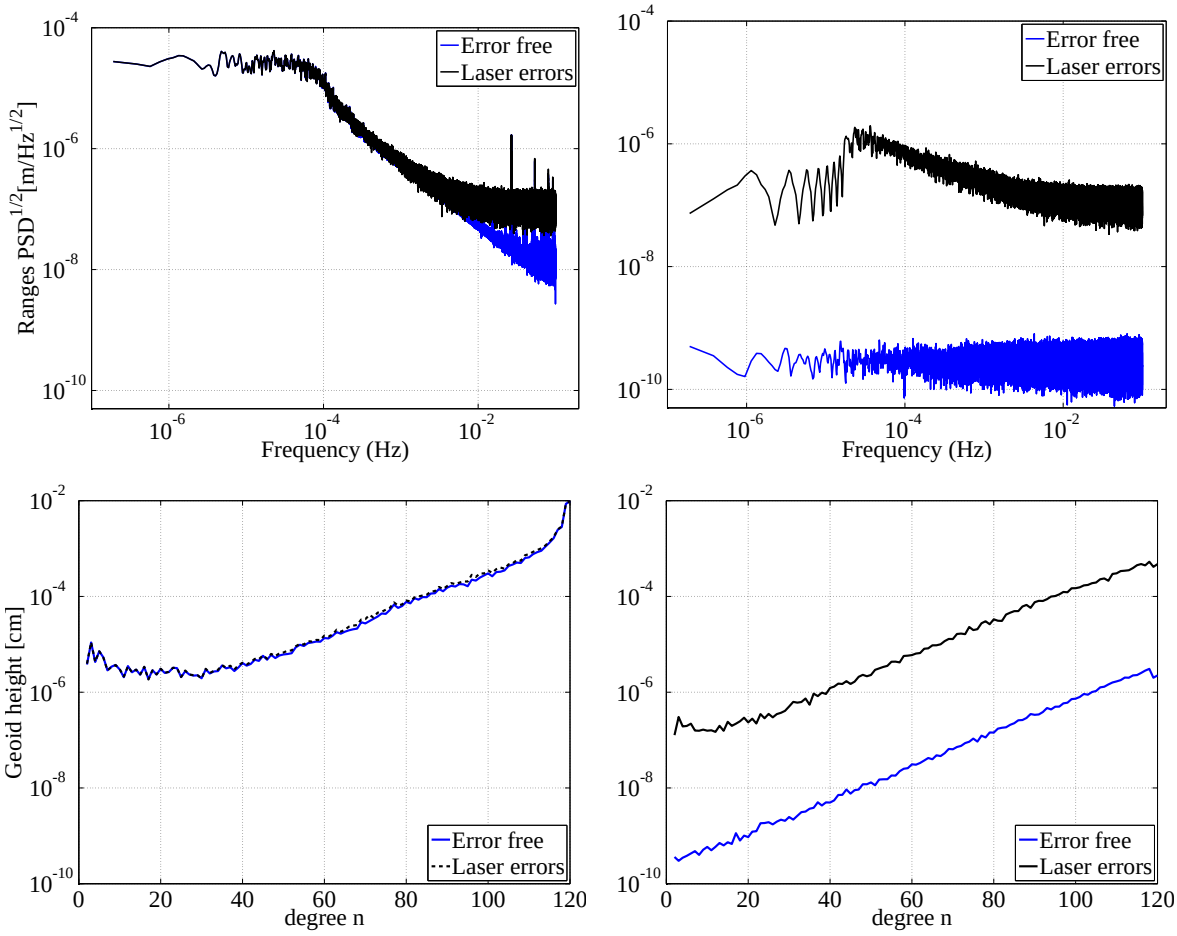

(a) Version 1 – Double precision

(b) Version 2 – Enhanced precision

Figure 5.3.5: ASD of LL-SST pre-fit residuals (top) and DDA in geoid heights (bottom) of d/o 120 solutions for ranges. Left: Processing with double precision (Version 1), right: processing with enhanced precision (Version2).

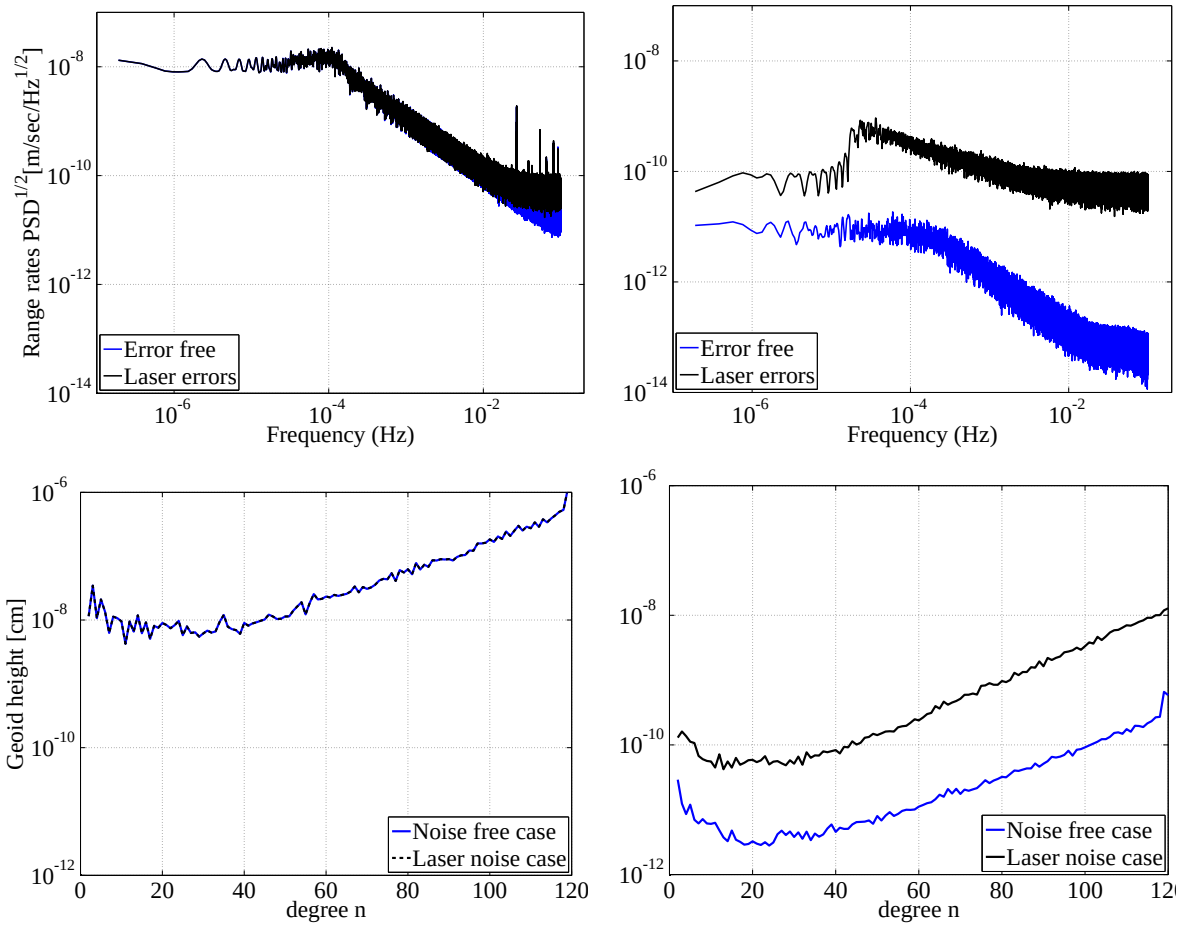

Figure 5.3.6: ASD of LL-SST pre-fit residuals (top) and DDA in geoid heights (bottom) of d/o 120 solutions for range rates. Left: Processing with double precision (Version 1), right: processing with enhanced precision (Version2).

Chapter 6

Methods of noise reduction

In Sec. 4.6 the impact of all noise sources in gravity field retrieval was analyzed. This section is dedicated to investigations concerning the treatment of propagated noise for NGGMs. Main focus is the handling of correlated noise such as the colored noise of sensors. Treatment of other noise sources such as temporal aliasing, is addressed in Chapter 7.

6.1 Frequency dependent data weighting

NGGMs will make use of satellite data that will most probably be corrupted by correlated noise. On-board sensors such as the accelerometers and the laser instrument for example possess noise behavior which is frequency-dependent and can be analytically approximated by the PSD curves shown in Sec. 4.5. The time series of their measurements is therefore corrupted with time-correlated noise which contaminate other quantities during the gravity field estimation.

Real satellite data contain noise which can be highly non-stationary, i.e. its stochastic properties change with time. LEO satellite orbits with an accuracy varying with time are a typical example of non-stationary noise. Moreover, jumps or spikes at the kinematic orbits contribute even more to the non-stationarity. In Ditmar et al. (2007), a methodology for estimating a proper weighting matrix that can be applied to data with gaps and non-stationary behavior, is presented. Since the dependency of noise on frequency is not known a priori, it is estimated on the basis of a posteriori residuals (i.e. the differences between the original and adjusted observations). In our simulation environment, uninterrupted orbits with a white noise behavior are used for reasons of simplification. Noise stemming from the behavior of the accelerometer and laser instruments are also assumed to be stationary, and therefore can be represented by a Power Spectral Density (PSD). As a result, quantities such as residuals, will also have a stationary behavior.

In Koch et al. (2010), covariance matrices are estimated in multivariate models by estimated auto- and cross-covariances. In our simulations, we assume that different components such as the 3-D position differences and the inter-satellite distance, can be considered uncorrelated with each other. The covari-

ance matrix will therefore contain only auto-covariance values of the residuals. Under the assumption that the data contain stationary noise, their covariance matrix is of a Toeplitz kind consisting of auto-covariance vectors. The elements of an auto-covariance vector with index k consist of the covariance c_k between epochs i and $i \pm k$ of the residual time series :

$$c_k = E[r_j r_{j\pm k}], \tag{6.1}$$

where $E[\cdot]$ is the expectation operator; r_j and $r_{j\pm k}$ are the residual values at two epochs separated by lag k. Assuming ergodicity of the noise realization (i.e. residuals), the ensemble average can be replaced by the time average. Eq. (6.1) can be therefore turned into a practical formula for estimating the auto-covariance vector :

$$c_k = \frac{1}{n_k} \sum_i r_j r_{j\pm k} \qquad (0 \le k \le n_a), \tag{6.2}$$

where n_a is the maximum lag for the estimated auto-covariance, and n_k is the number of pairs of elements used in the estimation of the $k-$th auto-covariance element. The covariance matrix of a Toeplitz kind can then then be fully assembled from the auto-covariance vector :

$$\mathbf{C} = \begin{pmatrix} c_0 & c_1 & \cdots & c_{n_{a-2}} & c_{n_{a-1}} \\ c_1 & c_0 & c_1 & \cdots & c_{n_{a-2}} \\ \vdots & c_1 & \ddots & \ddots & \vdots \\ c_{n_{a-2}} & \vdots & \ddots & \ddots & c_1 \\ c_{n_{a-1}} & c_{n_{a-2}} & \cdots & c_1 & c_0 \end{pmatrix}. \tag{6.3}$$

The weight matrix $\mathbf{P}$ can be computed as the inverse of the covariance matrix :

$$\mathbf{P} = \mathbf{C}^{-1}. \tag{6.4}$$

The gravity field modeling approach used in this study, divides the orbit to short arcs with boundary values that are parameterized together with the gravity field coefficients. The weight matrix $\mathbf{P}$ has therefore dimensions equal to the number of epochs n_s inside a short arc. The residual time-series however, contain low-frequency noise components that influence values exceeding the length of a short-arc, even if the boundary value points at the beginning and end of a short arc are set up as unknown parameters. In order to take into account those correlations, residual time series of size equal to $n_a = j \cdot n_s$ (where j an odd integer number) are considered as our noise realization. The corresponding covariance $\mathbf{C}_a$ and weight $\mathbf{P}_a$ matrices are of a $n_a \times n_a$ dimension. The final weight matrix $\mathbf{P}$ is taken then as the inner central $n_s \times n_s$ block of the larger $\mathbf{P}_a$ matrix. It contains auto-covariance values with a maximum lag of n_a, including correlations of $(j-1)/2$ "past" (i.e. before the central) and $(j-1)/2$ "future" (i.e. after the central) points. In Fig. 6.1.1 the procedure of extracting weight matrix $\mathbf{P}$ (Fig. 6.1.1 left) out of weight matrix $\mathbf{P}_a$ (Fig. 6.1.1 top-right) is demonstrated. For reasons of comparison, a weight matrix

computed from the residual time series of one arc is also shown (Fig. 6.1.1 bottom-right). It is evident that this weight matrix contains smaller auto-covariance values compared to those of the extracted matrix **P**, which is explained from the larger length of the time series.

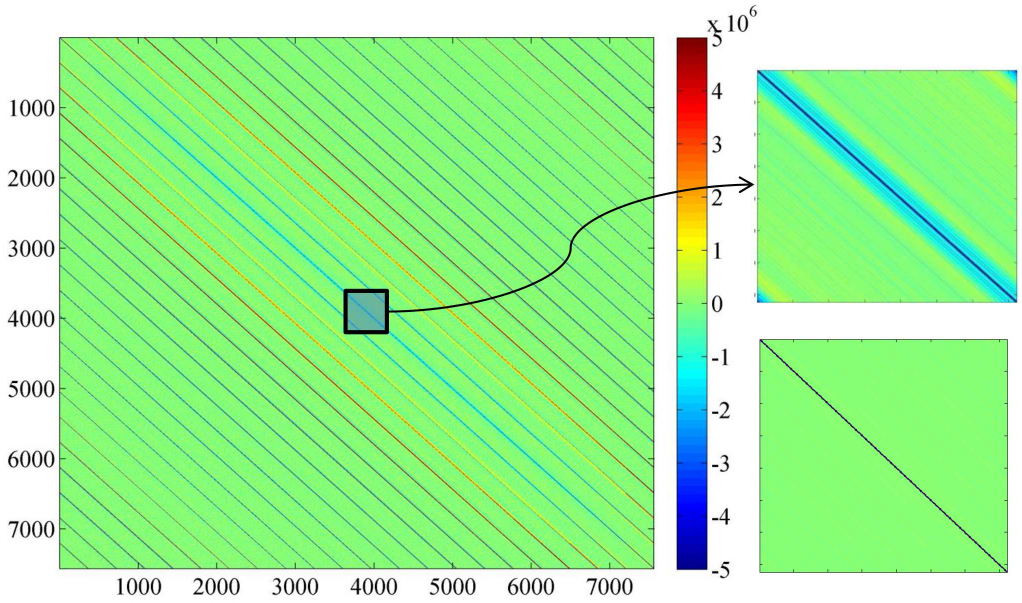

Figure 6.1.1: Weight matrix $\mathbf{P}_a$ (left) and extracted weight matrix **P** (top-right) used for data weighting. $\mathbf{P}_a$ corresponds to time series of a 21-arc period, while **P** to 1 arc (30 min.). A weight matrix computed directly from the residual time series of 1 arc is also shown (bottom-right).

Under the assumption of normally distributed observations, the estimated covariance matrix is positive definite. The weight matrix for the LL-SST part of the NEQ system $\mathbf{P}_{ll-sst}$, is computed from Eq. (6.4) using the method described above. For the HL-SST part, weight matrix $\mathbf{P}_{hl-sst}$ is assembled from components of the 3 individual weight matrices computed from the residuals along the X_1, X_2 and X_3 directions of the TRS. Assuming zero correlations between the individual directions of the 3-D position

differences for simplification purposes, $\mathbf{P}_{hl-sst}$ is a symmetric matrix computed as :

$$\mathbf{P}_{hl-sst} = \begin{pmatrix} p_0^x & 0 & 0 & p_1^x & 0 & 0 & \cdots & p_{n_{a-1}}^x & 0 & 0 \\ & p_0^y & 0 & 0 & p_1^y & 0 & \cdots & 0 & p_{n_{a-1}}^y & 0 \\ & & p_0^z & 0 & 0 & p_1^z & \cdots & 0 & 0 & p_{n_{a-1}}^z \\ & & & \ddots & \ddots & \ddots & \vdots & \vdots & \vdots & \\ & & & & & & p_0^x & 0 & 0 \\ & & & & & & & p_0^y & 0 \\ & & & & & & & & p_0^z \end{pmatrix}, \tag{6.5}$$

with p_k^x, p_k^y and p_k^z the components of the weight matrices for the X_1, X_2 and X_3 directions of the TRS. For the HL-SST and LL-SST NEQs to be accumulated into a combined system of NEQs, it is also assumed, for reasons of simplification, that they contain measurements that are uncorrelated with each other.

6.2 Empirical parameterization

NGGM will suffer from systematic noise as a result of the error sources described in Sec. 4.6. Part of this systematic noise can be compensated by proper stochastic modeling via frequency-dependent data weighting as explained in Sec. 6.1. However, mis-modeling effects and noise of systematic behavior will still be present, even after a proper data weighting has been performed. The sum of those effects is growing with the arc length. The short-arc approach used in this study, by setting up the boundary values at the beginning and end of an arc as unknowns, contributes to the reduction of this error accumulation. This co-parameterization classifies the short-arc approach into the reduced-dynamic strategies for gravity field retrieval. The functional model can be further augmented by introducing empirical accelerations. Together with the boundary points of an arc, they constitute the local parameters to be estimated (see Sec. 3.6.1). Local parameters are valid only for a short period of time (e.g. hourly, time period of a short arc), in order to compensate mis-modeling errors or modeled effects that change rapidly.

Empirical parameterization can be very helpful in cases where the main characteristics of an error pattern have an expected behavior. For example, noise related to spatial sampling accuracy or geometry such as orbit inaccuracies and temporal aliasing, result in noise accumulation at the end of the each orbit revolution. Fig. 6.2 depicts the monthly ASD of pre-fit residuals for the inter-satellite ranges of a d/o 120 solution, considering all error sources. The mis-modeling effects are accumulated and manifested as peaks at the frequencies of 1 cycle-per-revolution (1-cpr) and its multiples. For this reason, a very

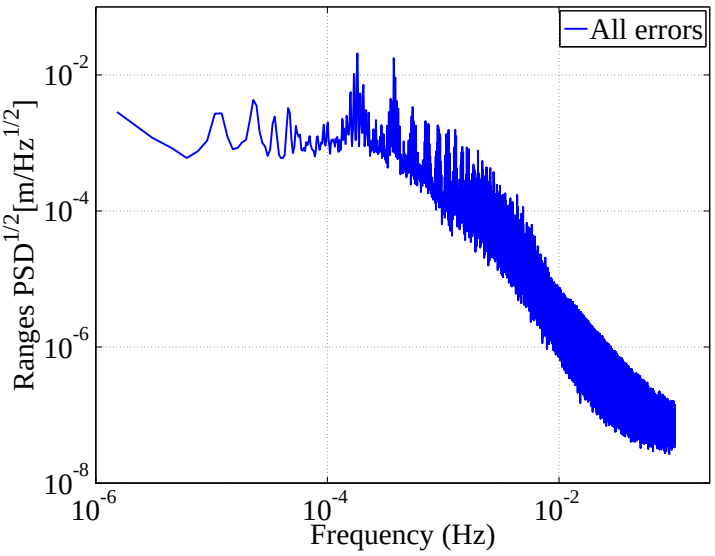

Figure 6.2.1: ASD of pre-fit residuals for the inter-satellite ranges ρ of a d/o 120 solution, considering all error sources.

common practice is the use of trigonometric sine and cosine functions to model the periodicity of the accelerations. Considering a constant term as well, the 1-cpr empirical accelerations can be modeled as :

$$\mathbf{f} = \mathbf{E}(\mathbf{a}_0 + \mathbf{a}_1 \sin\nu + \mathbf{a}_2 \cos\nu), \tag{6.6}$$

with $\mathbf{a}_0$ being the constant acceleration bias vector, $\mathbf{a}_1$ and $\mathbf{a}_2$ the 1-cpr coefficient vectors and ν the true anomaly of the satellite orbit. The vector of empirical accelerations is typically specified in the satellite-fixed reference frame, which is then transformed to the CRF by the transformation matrix $\mathbf{E}$ computed by Eq. 3.2. Empirical parameterization may also contain a linear term. Depending on the error characteristics of the miss-modeled forces, empirical accelerations can be modeled differently for each occasion. Gravity field processing of GRACE data, processed by the science data system centers such as the Center for Space Research (CSR), employ co-estimation of empirical biases and accelerometer scale factors in their official Release 05 solutions (Bettadpur, 2013). Finding the optimal parameterization choice is an empirical procedure that does not come without shortcomings. Even though it can drastically reduce the total error level, it can absorb real gravity signals. Occasionally, empirically estimated parameters may also introduce correlations and coupling effects with other measurement errors. Their modeling should therefore be handled with care and over-parameterization be avoided.

6.3 Simulation results of processing with noise-reduction methods

The error sources that are expected to influence a NGGM were defined in Sec. 4.6. In this section, methods for reducing their effect are applied and the results are demonstrated. All simulations were performed with Version 1 (DP) of the simulator. The solutions refer to a monthly averaged “AOHIS”product. Therefore, all error sources have been taken into account, except for the aliasing effects stemming from the uncertainties of a de-aliasing “AO” product, which would be used in case of a “HIS” retrieval. The

treatment of temporal aliasing effects is addressed extensively in Chapter 7. The chosen orbit for the simulations is the same one used for the error budget analysis performed in Sec. 4.6. Table 6.1 gives

Name	Processing method
Noise-Free (NFC)	Nominal
Noise Case 1 (NC_1)	Nominal
Noise Case 2 (NC_2)	Weighting
Noise Case 3 (NC_3)	Emp. Param. arc-wise bias
Noise Case 4 (NC_4)	Emp. Param. arc-wise linear
Noise Case 5 (NC_5)	Emp. Param. arc-wise 1-cpr + bias
Noise Case 6 (NC_6)	Weighting + Emp. Param. arc-wise linear

Table 6.1: Details of noise reduction processing. The solutions refer to a monthly mean of "AOHIS" signal. Noise-Free case already contains temporal aliasing errors due to under-sampling of "AOHIS" signal.

a description of the methods used for reducing the propagated noise. Term "Nominal" refers to a processing without any error handling. Simulations with individual, as well as combined utilization of frequency-dependent data weighting and empirical parameterization have been performed. Several cases of empirical parameterization have been examined. Each of them includes an arc-wise modeling of either a bias, linear, or 1-cpr and bias term.

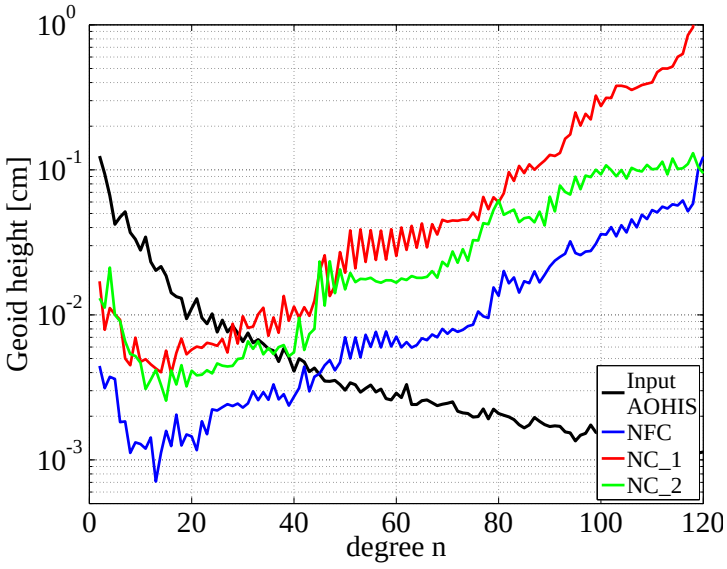

Figure 6.3.1: DDA in geoid heights of d/o 120 solutions. Blue: Noise-Free Case which contains only the effect of temporal aliasing (NFC). Red: NC_1 - nominal, Green: NC_2 - with frequency-dependent data weighting (see Table 6.1).

The weight matrix was computed from a noise realization of pre-fit residuals that was stationary. For the stationarity to hold, the residuals contained only the system processing errors and the effect of

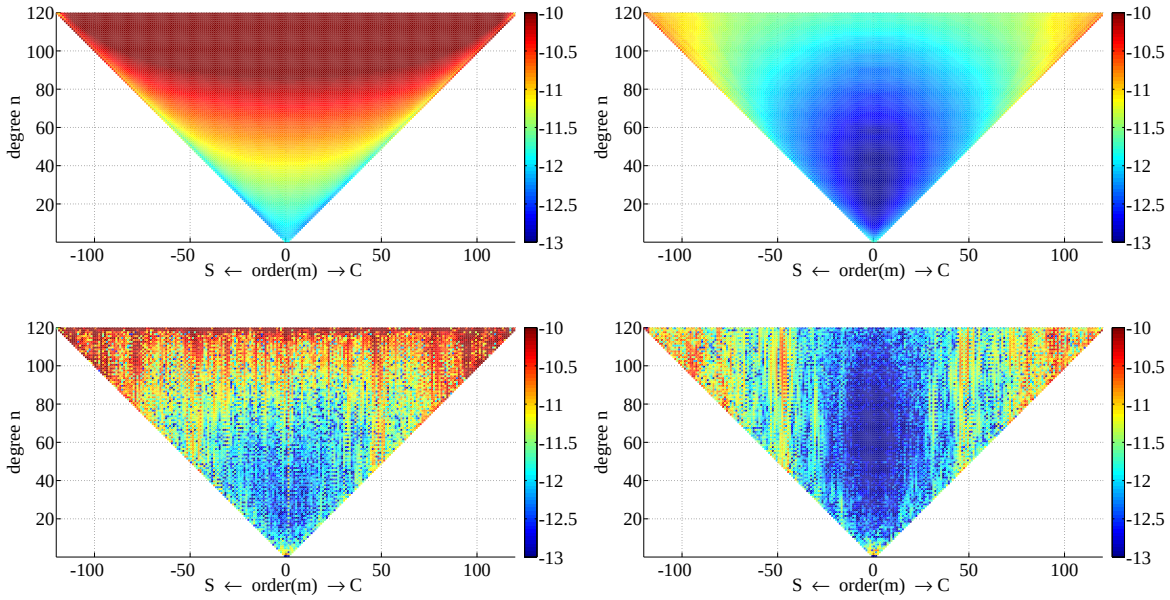

Figure 6.3.2: Formal errors (top) and coefficient differences (bottom) of d/o 120 solutions. Left: NC_1 - nominal, right: NC_2 - with frequency dependent data weighting (see Table 6.1)

propagated accelerometer and laser noise. The weight matrix was generated from a time series consisting 21 short arcs, as described in 6.1. It was then applied to the data including all error sources (NC_2 - Table 6.1). Fig. 6.3.1 depicts the DDA in geoid heights for the noise case with (NC_2) and without (NC_1) data weighting. A Noise-Free case (NFC) shown for reasons of comparison, already contains the temporal aliasing effects due to under-sampling of "AOHIS" signal. When applying weighting, an improvement is evident over the whole bandwidth. Especially at the lower and higher degree coefficients the improvement is larger. An error accumulation is experienced near d/o 50 and d/o 80. The first peak near d/o 50, could be related to the expansion limit (also d/o 50) of the two different models used to simulate the uncertainties of an ocean tide model. The triangle plot of coefficient differences in Fig. 6.3.2 clearly shows this effect near the coefficients of degree 50. Overall, data weighting succeeds in absorbing a large part of the propagated noise, and results in a similar relative improvement for the formal errors and the coefficient differences.

Fig. 6.3.3 depicts the DDA values of solutions processed with co-estimation of empirical accelerations. In all cases, empirical parameterization leads to a small error reduction of the higher coefficients above d/o 90. In the rest of the bandwidth, it not only fails to successfully absorb error, but additionally introduces non-realistic signals that lead to a degradation of the results at the low-to-intermediate coefficients until d/o 50. The biggest change in the error spectrum is achieved with the 1-cpr-plus-bias arc-wise parameterization (6.3.3 bottom-left), where large improvements at higher degree coefficients are manifested together with degradations at the lower. This considerably larger improvement stems from a better approximation of the 1-cpr functions to the higher frequency part of the noise. Similar conclu-

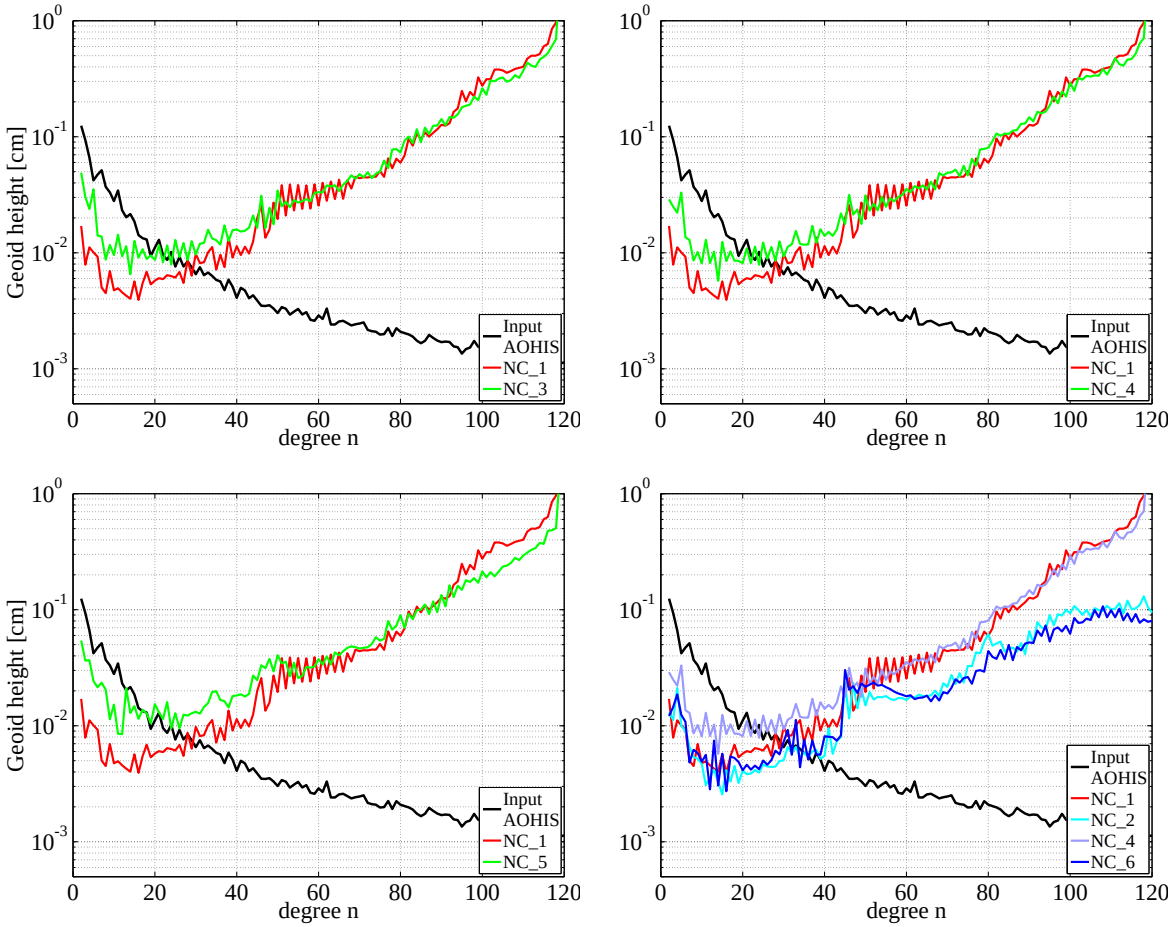

Figure 6.3.3: DDA in geoid heights of d/o 120 solutions. Top-left: NC_3, top-right: NC_4, bottom-left: NC_5, bottom-right: NC_6 (see Table 6.1).

sions can be drawn by inspecting the triangle coefficient difference plots of Fig. 6.3.4. Comparing Fig. 6.3.2 bottom-left with Fig. 6.3.4-bottom-left, an error reduction at the coefficients of high degree and low order can be observed, along with an error increase at the sectorials. In all cases, there is an evident weakness of the empirical accelerations to absorb noise of an intermediate-to-long wavelength behavior. This could be related to the applied short-arc approach for gravity field modeling. The empirical accelerations are updated every 30 min together with the boundary conditions of the short-arc. However, noise included in the observations such as accelerometer errors, has a much longer wavelength behavior. It is therefore unlikely for the long wavelength characteristics of noise to be accurately described by empirical functions of that duration. On the other hand, high frequency effects can be partially modeled by empirical accelerations of a short-arc period, which result in improvements at the higher coefficients bandwidth. This could be helpful, in case where empirical parameterization is applied together with data weighting. The bottom-right plot of Fig. 6.3.3 shows the results from a case where linear empirical parameterization is employed together with frequency dependent data weighting (NC_6). The retrieval

error differs from that of NC_2, by a small degradation at the lower degree coefficient bandwidth until d/o 60, and an improvement at the higher degree coefficients.

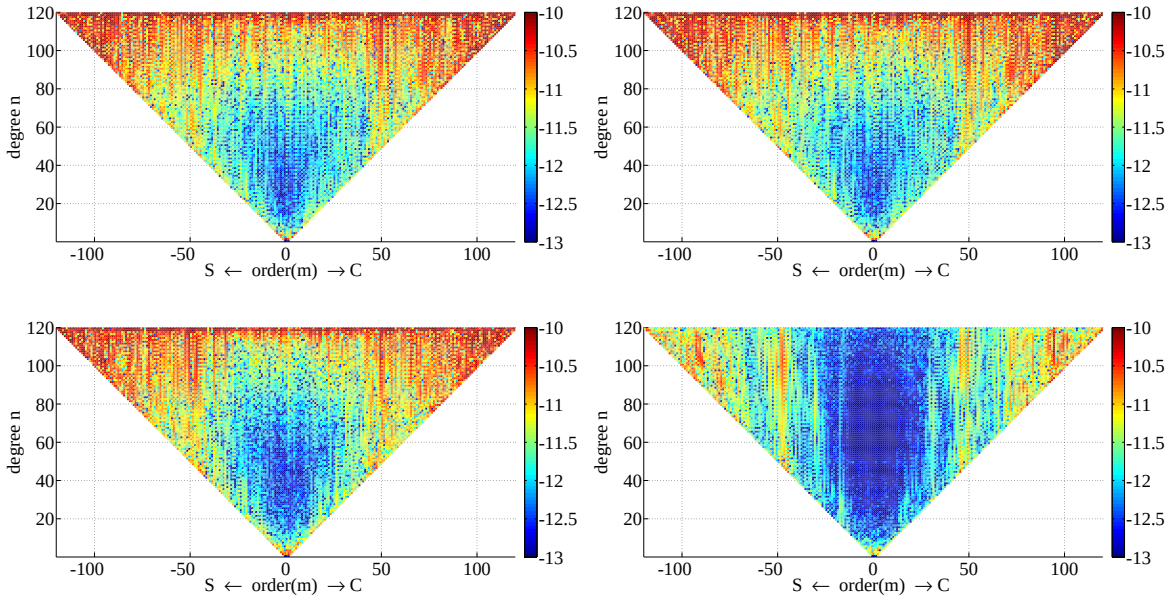

Figure 6.3.4: Coefficient differences of d/o 120 solutions. Top-left: NC_3, top-right: NC_4, bottom-left: NC_5, bottom-right: NC_6 (see Table 6.1).

Fig. 6.3.5 depicts the ASD values of post-fit residuals for the inter-satellite ranges ρ. The post-fit residuals result from the estimated gravity field solution and contain the effect of the applied method for noise reduction. The local parameters are estimated after the solution of the NEQ system by means of back-substitution (Fig. 3.6) and are explicitly used for estimating the post-fit residuals. In case of NC_2 they include only the arc boundary values, whereas in case of NC_3, NC_4, NC_5, NC_6 also the empirical accelerations. The results strengthen the conclusions made by interpreting Fig. 6.3.3, where the use of empirical accelerations resulted in improvement at the shorter wavelengths and degradation at the longer. For the NC_4 and NC_5 cases, the error magnitude of 1-cpr resonances and their multiples is also reduced. However, the biggest improvements are experienced in frequencies larger than 4 mHz for both cases NC_2 and NC_6, where the frequency dependent data weighting is employed. This frequency band is particularly sensitive to important gravity field characteristics. Compared to case NC_5, case NC_6 exhibits improvements at the 1-cpr terms, as a result of additionally employing the linearly estimated empirical accelerations.

Fig. 6.3.6 depicts the results of the noise reduction methods applied, in terms of closed-loop geoid height differences. The plots show differences of the solutions at the maximum resolution of d/o 120. The cases processed with estimated empirical accelerations show mild improvements with a similar error pattern governed by the ground-tracks of the satellites. On the other hand, big improvements are obtained by processing with data weighting. The standard deviation values of geoid height differences improve

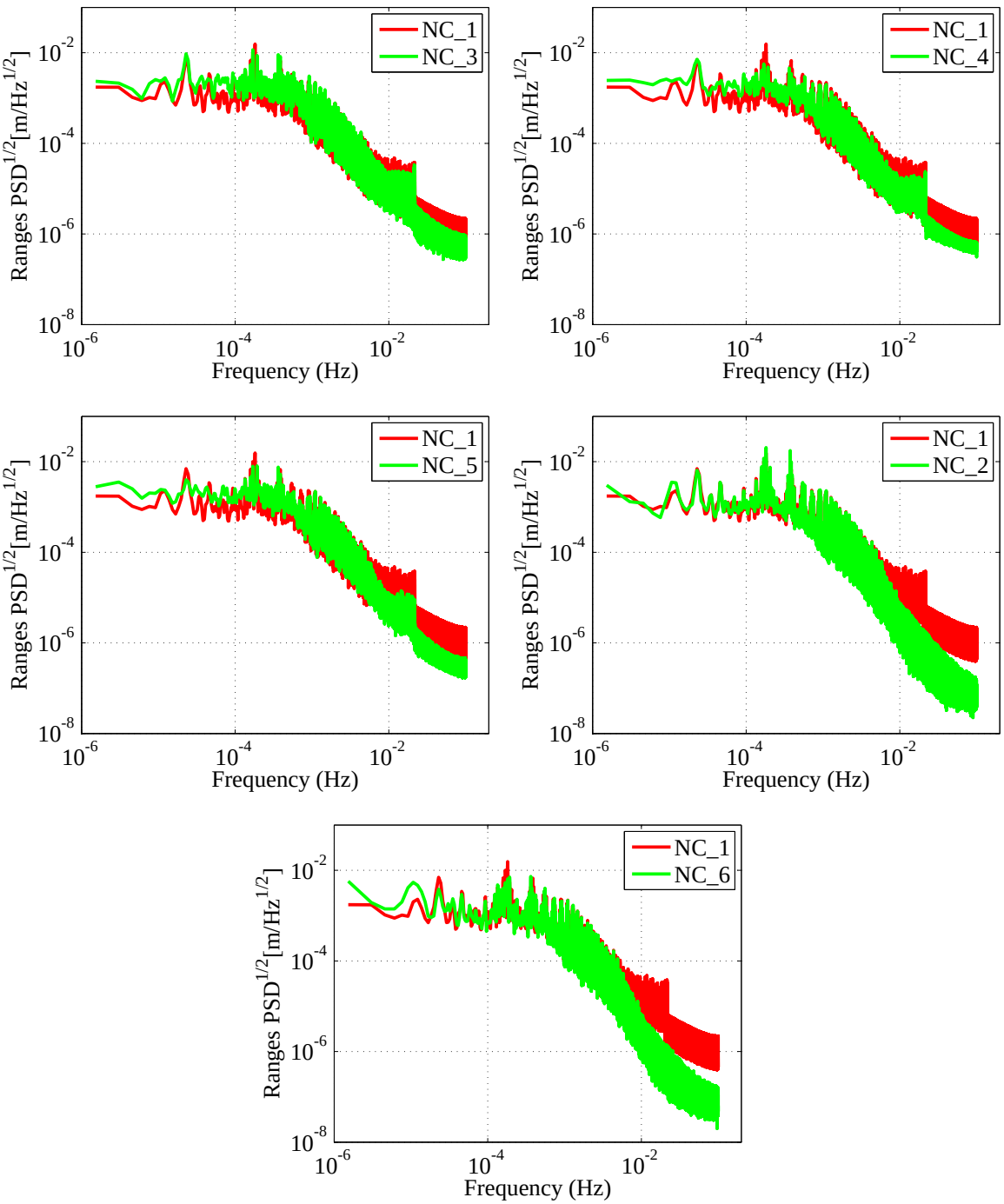

Figure 6.3.5: ASD of post-fit residuals for the inter-satellite ranges ρ of d/o 120 solutions (see Table 6.1).

from 6.45 cm in case of NC_1 to 0.52 cm and 0.44 cm in case of NC_5 and NC_6, respectively. The error pattern is also drastically changed from ground-track based, to north-south oriented striping.

The investigations on methods of noise reduction performed in this section, revealed great improve-

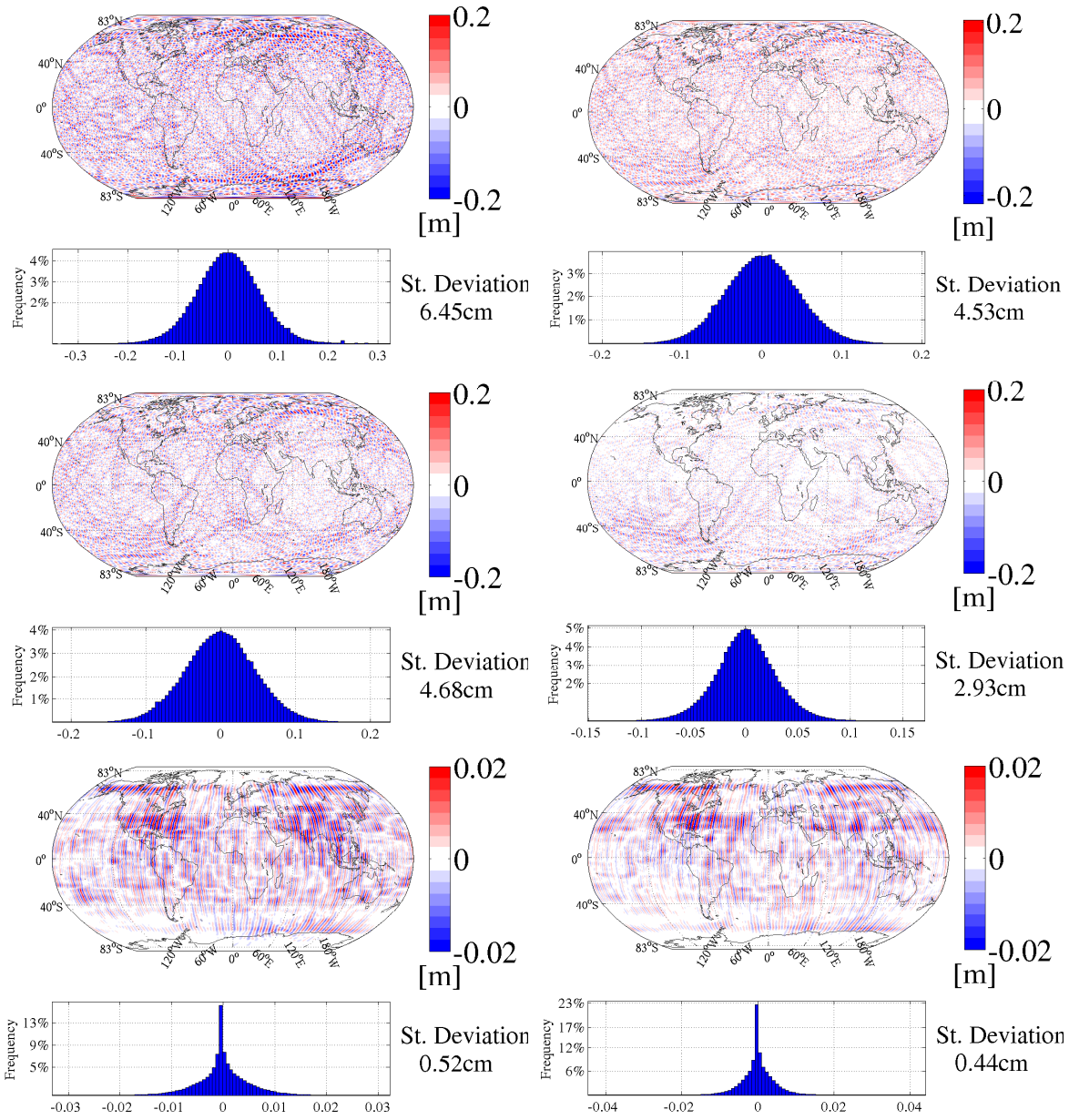

Figure 6.3.6: Closed-loop geoid height differences of d/o 120 solutions. Top: NC_1 (left), NC_3 (right). Middle: NC_4 (left), NC_5 (right). Bottom: NC_2 (left), NC_6 (right). Bottom figures have different colorbar limits. Processing details available in Table 6.1.

ments when the proposed data weighting scheme is applied. On the other hand, the applied parameterization of empirical accelerations did not show the same efficiency in reducing the propagated noise. This does not mean however, that empirical parameterization would not be helpful in gravity field processing of NGGMs. Depending on the parameterization choices (i.e. analytical models, short/long periods, axes used, e.t.c.), the effectiveness of empirically estimated accelerations in absorbing noise may vary. In Beutler et al. (2010), the effect of stochastic pulses (instantaneous velocity changes) and piece-wise

linear accelerations to the gravity field estimation is investigated. Some constraints on the magnitude of those empirically estimated parameters are also considered. It is demonstrated that co-estimation of empirical parameters leads to a reduction of the error levels, making their usage essential for the estimation procedure. Therefore, the employment of empirically estimated parameters depends strongly on the applied gravity field retrieval method and on the nature of the noise present in the system. Finally, the proposed strategy of noise reduction used for the investigations performed in Chapter 7, includes data weighting together with arc-wise linear co-estimation of empirical accelerations.

Chapter 7

Treatment of temporal aliasing effects

This section addresses one of the key limiting factors for NGGMs, namely temporal aliasing. The effect of this major error source was assessed for one near-polar pair in Sec. 4.6. Here, the mitigation of temporal aliasing effect is assessed in the presence of a Bender-type constellation (Sec. 7.1), expected to be operated for future satellite gravity missions. Errors due to temporal aliasing cannot be treated by means of frequency dependent data weighting as introduced in Sec. 6.1, due to their deterministic and non-stationary behavior. Sec. 7.2 investigates gravity field processing techniques that result in a significant reduction of temporal aliasing effects. Those techniques are also applicable to current LL-SST missions, but are specially beneficial for NGGMs with more complex SFF constellations. The investigations performed in this section were performed in the framework of the "ESA-SC4MGV" study (Iran Pour et al., 2015).

7.1 Temporal aliasing for NGGMs

NGGMs are planned to fly as SFF constellations that will lead to substantial improvements compared to the single in-line SFFs used by missions like GRACE, and in the near future by GRACE-FO. SFF constellations are expected to mitigate physical constraints related to sampling that lead to effects such as temporal aliasing.

7.1.1 Benefits of a Bender-type SFF constellation

The advantages of a Bender-type SFF constellation compared to a typical polar pair GRACE-type SFF are already mentioned in Sec. 4.2. Here, a Bender-type constellation with the orbital choices described in Table 4.1 is processed and compared to the polar pair of its constellation. The simulations take all error sources into account, except for errors of the de-aliasing models which do not apply when retrieving the full "AOHIS" signal (see Sec. 7.1.2). The retrieval period time-span was chosen equal to 11 days, which is the duration of a full repeat cycle of the polar pair. According to the revised Colombo-Nyquist rule-of-thumb (Weigelt et al., 2013), for solutions retrieved using near-polar orbits, the maximum resolvable

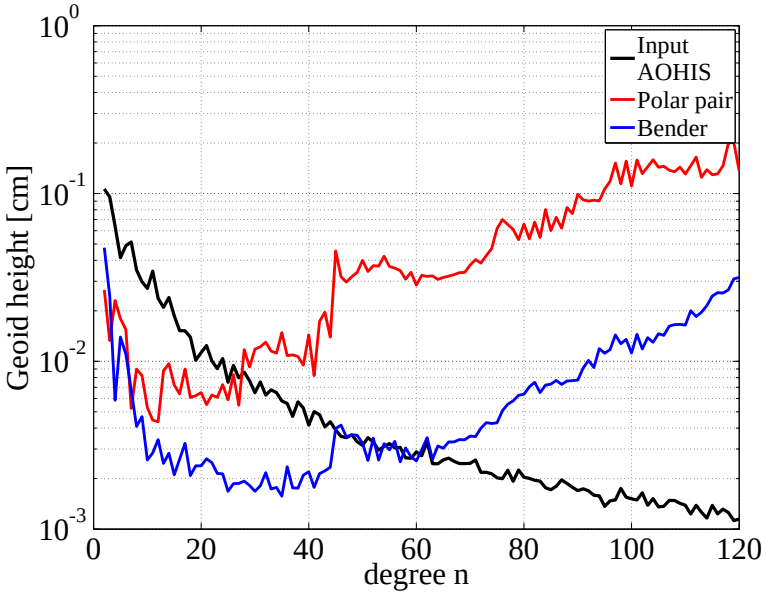

Figure 7.1.1: DDA in geoid heights of 11-day d/o 120 solutions for a polar pair and a Bender-type constellation. All errors included.

order of expansion is equal to the number of orbital revolutions in a repeat period, if the difference between number of revolutions and number of nodal days is of odd parity. This is the case for the near-polar orbit used for our investigations, which performs 15 orbital revolutions in one day. Thus, the retrieval period of 11 days could theoretically deliver homogeneous gravity field solutions up to order 165. The maximum resolvable degree on the other hand, depends on observation technique, observation noise and signal attenuation with altitude, having an impact on the SNR. However, we assume that a homogeneous gravity field solution of d/o 120 and retrieval period of 11 days can be achieved with the near-polar orbit we use for the simulations. The processing includes handling of the propagated noise, with the strategy proposed in Chapter 6, which involves frequency-dependent data weighting and arc-wise (i.e. 30 min) co-estimation of 3D linear empirical accelerations. The remaining errors represent the combined effect of un-modeled propagated noise and temporal aliasing effects. Fig. 7.1.1 depicts the DDA values for the polar pair and the Bender constellation. The addition of the inclined pair (Bender constellation) results in improvements of one order of magnitude at almost the complete error spectrum, except for the very low degrees (i.e. $0 \sim 7$). In case of the polar pair, the errors become larger than the signal near degree 28, while for the Bender constellation near degree 63. This is translated into an increase in maximum spatial resolution from 715 to 315 km.

The formal error estimates of the spherical harmonic gravity field coefficients and the closed-loop coefficient differences, are depicted in the triangle logarithmic plots of Fig. 7.1.2. The solution using the Bender constellation delivers a completely different error spectrum compared to the polar pair, where the higher tesseral harmonics still dominate the error budget, but the error levels are much lower. Moreover, both the formal errors and the coefficient differences exhibit an increased error at specific tesseral coefficients that resembles a “butterfly” pattern. This pattern is typical for Bender constellations due to the lower inclination choice of the inclined pair, and is caused at the transition zone of higher latitudes

where Earth's sampling gradually changes from two pairs to one polar pair.

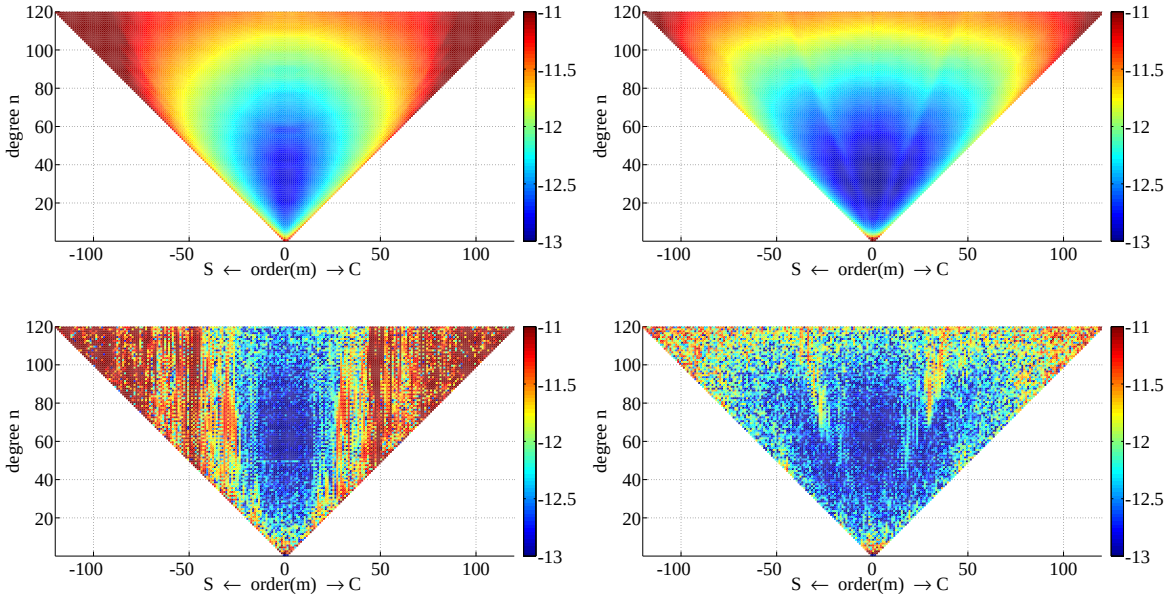

Figure 7.1.2: Formal errors (top) and coefficient differences (bottom) of d/o 120 solutions. Left: Polar pair, right: Bender SFF constellation. Processing includes all errors sources but de-aliasing model inaccuracies.

7.1.2 Processing strategies for retrieval content

LEO satellites are generally affected by time-varying gravitational forces exerted from the underlying mass distribution within the atmosphere, the ocean, Earth's surface and interior. Typically, gravity field processing of missions like GRACE employ background models to remove non-desirable signals from the integrated observations. Such signals can be ocean and solid Earth tides, but also non-tidal high-frequency mass variations that alias into the longer time retrieval periods. Those high-frequency variations are mainly induced by atmosphere and ocean and their effect is reduced in short time intervals by use of de-aliasing models. As mentioned in Sec. 4.6, this study makes use of the de-aliasing models from Dobslaw et al. (2013) with a 6-hourly time resolution, along with an empirical error estimate of those models. Therefore, 6-hourly estimates of atmosphere and ocean non-tidal signals would typically be subtracted from the observations during the gravity field processing. Finally, the retrieved gravity field solutions contain the integrated effect of hydrology, ice and solid Earth (else "HIS"), which is the final product of gravity field processing with GRACE data.

In this study, it is investigated to what extent a retrieval of the full "AOHIS" signal is feasible in the case of NGGMs. The motivation behind this idea is the scientific importance of recovering the full spectrum of non-tidal geophysical processes that comprise system Earth. In the following sections, the ability of a Bender constellation for retrieving the full "AOHIS" signal is investigated. It is expected, that an

increase in error isotropy, temporal and spatial resolution together with an appropriate parameterization (Sec. 7.2) could allow for the rapid sub-weekly changes of the atmosphere and ocean to be successfully recovered and then assigned into a longer-period average solution. Solving for the full "AOHIS" signal requires a crucial change of the gravity field processing strategy that results in a different error tree. The change concerns the usage of de-aliasing models, which are no longer necessary. This results in a gravity field solution that is clean of de-aliasing model errors. On the other hand, temporal aliasing errors due to under-sampling of "AOHIS" are more prominent than "HIS". This counter-effect is quantified in Fig. 7.1.3-left for an 11-day solution of a Bender constellation. The solutions contain a relative weighting between the HL-SST and LL-SST component by using σ_0 values of $1cm$ and $50nm$, respectively. The blue and green curves represent temporal aliasing effects due to "AOHIS" and "HIS" under-sampling correspondingly. The full "AOHIS" signal induces aliasing effects which are one order of magnitude larger than for "HIS". Errors due to de-aliasing model inaccuracies (magenta curve) are also significantly larger than the "HIS" aliasing curves. However, they exceed the "AOHIS" aliasing errors only at the lower coefficients until d/o 25. Fig. 7.1.3-right depicts the results considering all error sources of each retrieval strategy, processed with data weighting and empirical parameterization. Although it contains propagated noise, the blue error curve in Fig. 7.1.3-right is lower than in Fig. 7.1.3-left for the high degree coefficients. This results from the error reduction method applied in the results of Fig. 7.1.3-right compared to the simple relative weighting of Fig. 7.1.3-left. By visualizing Fig. 7.1.3-right, we can conclude that the two strategies result in similar error levels. However, the "HIS" retrieval exhibits larger errors at the lower coefficients until d/o 25, which could be attributed to the errors at the de-aliasing "AO" models. This is confirmed by the higher error levels of the magenta curve compared to the blue curve at the same coefficient bandwidth of Fig. 7.1.3-left, which proves that errors due to de-aliasing "AO" model innacuracies, are more significant than errors due to "AOHIS" under-sampling. At the rest of the bandwidth, the "AOHIS" retrieval shows larger errors, mainly caused by the larger aliasing effects of "AOHIS" compared to "HIS". It is interesting to notice however, that the two processing strategies result in retrieval errors of a similar accuracy for "AOHIS" and "HIS" content. The retrieval errors of the two strategies are re-examined in Sec. 7.3, where the method for reducing temporal aliasing effects has already been applied.

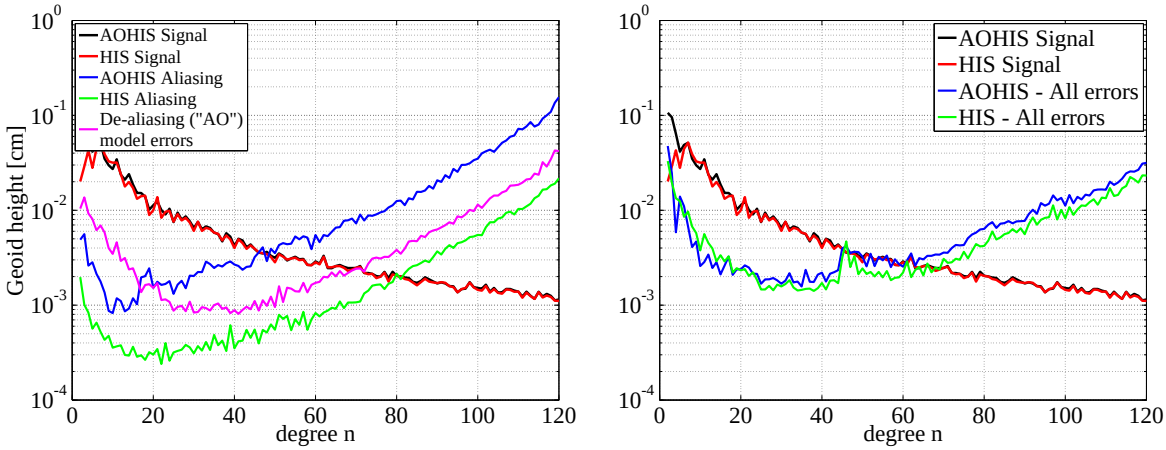

Figure 7.1.3: DDA in geoid heights of 11-day d/o 120 solutions for a Bender-type constellation. Left: Aliasing errors due to under-sampling signals of interest and errors at the de-aliasing "AO" models. Right: All error sources included.

7.2 Co-parameterization of low spatial resolution gravity field solutions at higher frequencies

This section investigates gravity field processing techniques that result in a reduction of temporal aliasing effects at the final solution. The adopted processing strategy was first proposed by Wiese et al. (2011b) and is going to be referenced as the *Wiese approach* from now on. According to this method, low resolution gravity fields are co-estimated at short time intervals together with the higher resolution gravity field which is sampled at a longer time interval. By co-estimating gravity fields at shorter periods (e.g. daily), the high-frequency information contained in them is taken into account. As a result, the aliasing effect of those long-wavelength geophysical signals that have a period larger than twice the chosen sampling period of the short-period gravity field modeling (Nyquist theorem), can be reduced. Consequently, the maximum temporal resolution of the retrieved gravity fields, which were hampered by aliasing effects when applying a classical parameterization, can be increased.

The estimation of n number of low spatial resolution gravity field solutions is achieved by including their coefficients in the set of local parameters (i.e. boundary values and empirical accelerations) to be co-estimated. Practically this leads to an extension of vector $\acute{\mathbf{b}}$ by the lower gravity field coefficients of $\tilde{\mathbf{x}}$ (see Eq. (3.52)) :

$$\acute{\mathbf{b}}_{ext} = \left(\mathbf{b}_1 \quad \cdots \quad \mathbf{b}_J \quad | \quad \tilde{\mathbf{x}}_1 \quad \cdots \quad \tilde{\mathbf{x}}_L\right), \tag{7.1}$$

and an extension of matrix $\acute{\mathbf{B}}$ with the corresponding elements of $\bar{\mathbf{A}}$:

$$\acute{\mathbf{B}}_{ext} = \left(\mathbf{B}_1 \quad \cdots \quad \mathbf{B}_J \quad | \quad \bar{\mathbf{A}}_1 \quad \cdots \quad \bar{\mathbf{A}}_L\right), \tag{7.2}$$

where L the number of unknown coefficients contained in the low resolution solutions. The extended

part of matrix $\acute{\mathbf{B}}_{\mathbf{ext}}$ is updated according to the chosen short-time sampling interval. Accordingly, the vector of unknown gravity field coefficients $\tilde{\mathbf{x}}$ is reduced to :

$$\tilde{\mathbf{x}}_{red} = \begin{pmatrix} \tilde{\mathbf{x}}_{L+1} & \cdots & \tilde{\mathbf{x}}_{M} \end{pmatrix}, \tag{7.3}$$

and the corresponding design matrix $\bar{\mathbf{A}}$ to :

$$\bar{\mathbf{A}}_{red} = \begin{pmatrix} \bar{\mathbf{A}}_{L+1} & \cdots & \bar{\mathbf{A}}_{M} \end{pmatrix}, \tag{7.4}$$

with the number of unknown coefficients for the long-term average field $\tilde{\mathbf{x}}_{red}$ being reduced to that of the remaining higher degree coefficients $H = M - (L+1)$. The local parameters $\acute{\mathbf{b}}_{ext}$ are pre-eliminated at short-time period basis as described in Sec. (3.6.2), forming a reduced system of NEQs. The n reduced and full NEQs are both stored to be used at a later stage. As a next step, the reduced NEQs are accumulated for the period of the longer-time solution, and the system is solved with LSA to obtain the set of higher degree gravity field coefficients. Finally, the n reduced and full NEQs, together with the set of higher degree gravity field coefficients, are used by means of back-substitution (Eq. (3.56)) in order to obtain the n low degree resolution gravity field solutions. Concerning the lower part of the long-period averaged solution, a weighted mean is computed by variance propagation of the n short-time solutions. Fig. 7.2.1 illustrates the flowchart of Wiese parameterization. The main goal of Wiese parameterization is to reduce temporal aliasing effects and improve the estimates of high d/o coefficients. At the same time, it provides short-time gravity field estimates of low spatial resolution which are uncorrelated among each other. These high-frequency solutions constitute a new by-product feasible with NGGMs, that could be of a great value to the scientific user community. The choice of maximum expansion and estimation period for the low resolution solutions, plays an important role for the reduction of temporal aliasing effects in the long-term solution. The multivariate graph of Fig. 7.2.2 was used for consolidation of those choices. Fig. 7.2.2-top-left is taken from Murböck (2015). The background pixeled values in greyscale represent the "AOHIS" signal RMS per degree. Again, the revised Colombo-Nyquist was taken into account like in Sec. 7.1.1. The maximum spatial resolution for the solutions depends on the combination of the orbit configuration and the sensitivity of the measurement system. From the perspective of orbit configuration, the blue curves in Fig. 7.2.2 represent the spherical harmonic degree of expansion (X-axis) that corresponds to the mean gap evolution along the equator, w.r.t. the solution period (Y-axis). The red curves represent the maximum gap evolution accordingly. The dashed curves stand for the polar-pair, while the solid for the Bender constellation. The optimum choice for the maximum d/o of expansion lies somewhere between the red and the blue curve, with the blue curve being a stronger candidate assuming an equally good homogeneity over the whole globe. It is therefore possible to directly visualize the signal variability that can be captured in different time periods, in relation to the maximum degree of expansion.

A first interpretation of Fig. 7.2.2, is that the strongest "AOHIS" variability (darker pixels) has a long-wavelength behavior taking place at periods of 2.5 days until 1 month. In case of our 11-day solution, signals with variations shorter than 5.5 days will alias into the solution. However, a daily

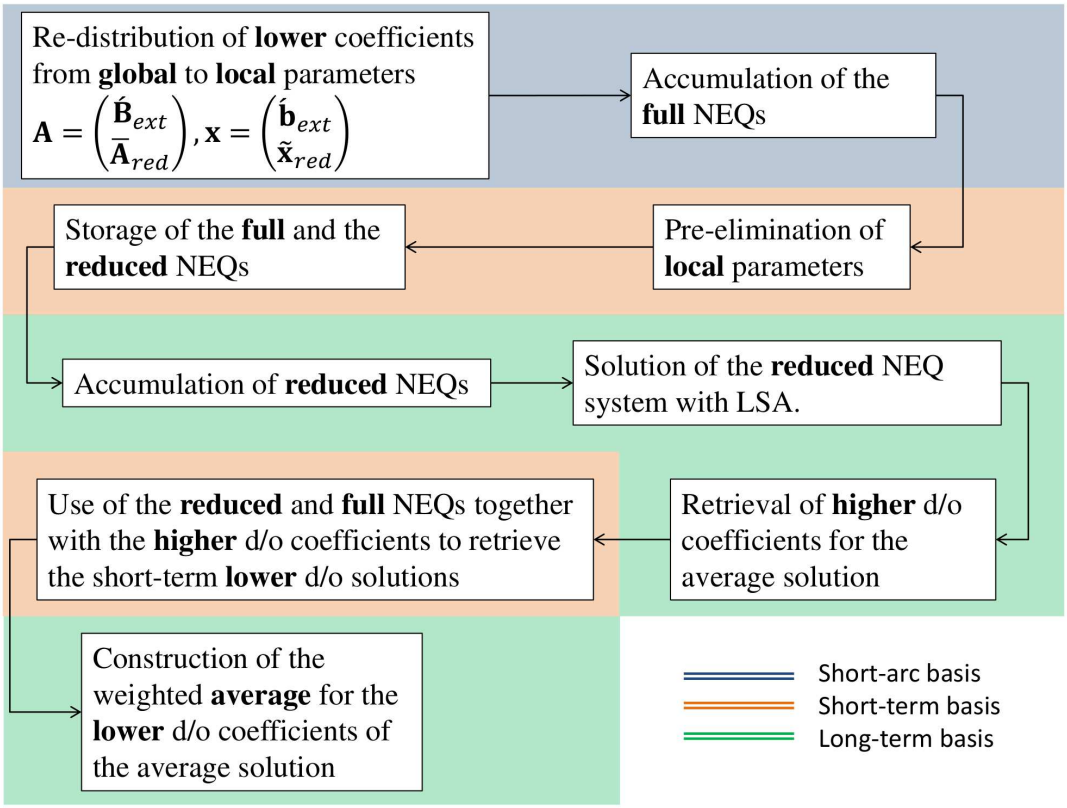

Figure 7.2.1: Flowchart of the Wiese parameterization. Background colors denote the time period of operation.

parameterization can retrieve a significant part of this signal. This is illustrated by the blue rectangle in Fig. 7.2.2 top-right, which highlights the signal variability of a daily solution until d/o 20 according to the Nyquist sampling theorem. It is evident that a large part of the signal that normally aliases, can be co-estimated and assigned afterwards to the average 11-day solution. The black arrow points to the crossing point of the maximum degree with the retrieval period, which is positioned in-between the red and blue solid curves. This suggests an adequate sampling for a daily estimation at the given resolution. Retrieval periods other than daily have also been investigated due to their different signal content. A 3-daily estimation interval was investigated due to the fact that it holds the same period as the sub-cycle of the polar pair. A half-daily interval was also investigated in order to capture signals present at even higher frequencies, mostly driven by atmosphere. Fig. 7.2.2 bottom-left and 7.2.2 bottom-right depict the retrievable “AOHIS” signal for a 3-day and half-day estimation. Table 7.1 gives an overview of the investigated parameterization choices.

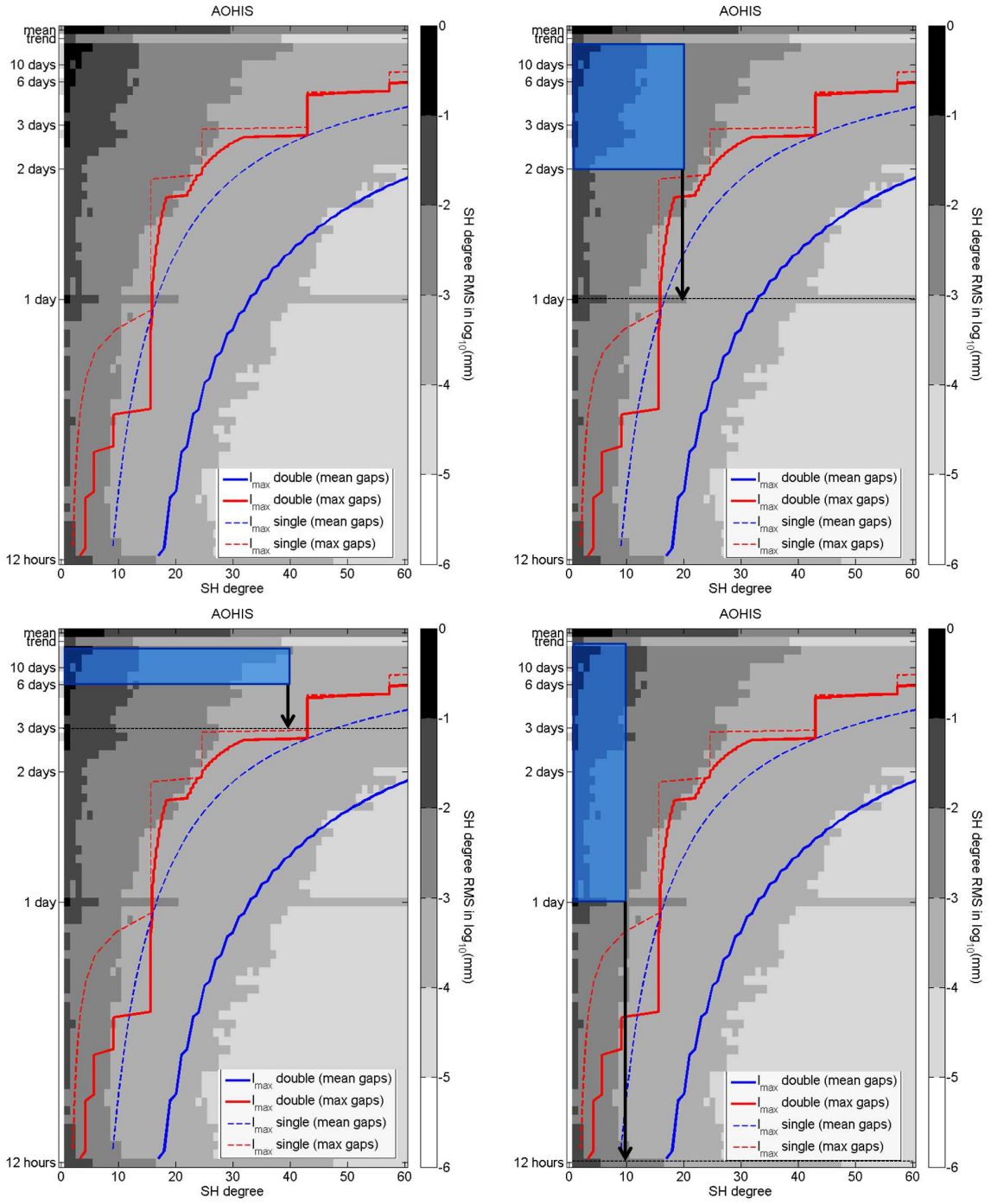

Figure 7.2.2: Consolidation of short-period parameterization choices. Top-left plot is taken from Murböck (2015). X-axis stands for the spatial and Y-axis for the temporal resolution. Dashed rectangles represent the retrievable "AOHIS" signal for given periods and resolution according to the Nyquist theorem. Top-right: daily - d/o 20, bottom-left: 3-daily - d/o 40, bottom-right: half-daily - d/o 10.

Parameterization	Short periods		Long period	
	days	max. d/o	days	max. d/o
Nominal	-	-	-	-
$\text{Wiese}_{1/10-11/120}$	1	10	11	120
$\text{Wiese}_{1/20-11/120}$	1	20	11	120
$\text{Wiese}_{1/30-11/120}$	1	30	11	120
$\text{Wiese}_{3/30-11/120}$	3	30	11	120
$\text{Wiese}_{0.5/10-11/120}$	0.5	10	11	120

Table 7.1: Investigated cases of Wiese parameterization.

7.2.1 Noise-free case analysis

As a first step, the potential benefit of co-parameterizing daily lower gravity fields for a noise-free case was investigated. The reason behind this was to investigate how the Wiese parameterization performs without the influence of other error sources but the physical temporal aliasing induced by under-sampling of "AOHIS" signal. Therefore, the term noise-free is here only used conventionally. All investigations were performed for the same 11-day period lasting from 1-1-1996 until 11-1-1996.

A very important part of the investigations concerned the assessment of the short-period gravity field solutions. The question is, how much signal is retrieved in those fields. Fig. 7.2.3 depicts the temporal aliasing effects in terms of DDA in geoid heights for daily, 3-daily and half-daily solutions. The black curves depict the input "AOHIS" signal and the colored curves the difference of the estimated gravity field solutions with the mean "AOHIS" for the equivalent time period. In case of a 3-daily parameterization, the 11-daily long-term average solution could not be reconstructed from integer number of 3-daily short-term solutions. Therefore, the co-estimation was performed for three 3-daily and one 2-daily short-term solutions. The daily gravity fields (Fig. 7.2.3 top-left) contain indeed a great part of the "AOHIS" signal, with a SNR larger than 1 for the complete bandwidth until degree 30. This holds also for the 3-daily solutions until degree 37 (Fig. 7.2.3 top-right), and for half-daily until degree 10 (Fig. 7.2.3 bottom). Particularly in case of the daily d/o 10 and d/o 20 solutions, spectral leakage effects show up illustrated by the increased error levels close to the maximum degree of expansion, indicating that there is retrievable signal at higher degrees. These findings strengthen our initial assumption that the maximum resolvable d/o follows the blue solid curve in Fig. 7.2.3. Table 7.2 provides statistical analysis of the gravity field solutions estimated at high frequencies. In all cases the statistics refer to the mean values of the individual solutions that were estimated at different maximum expansion. The "AOHIS" signal was estimated each time with the same maximum expansion as the high frequency gravity field solutions, in order to estimate

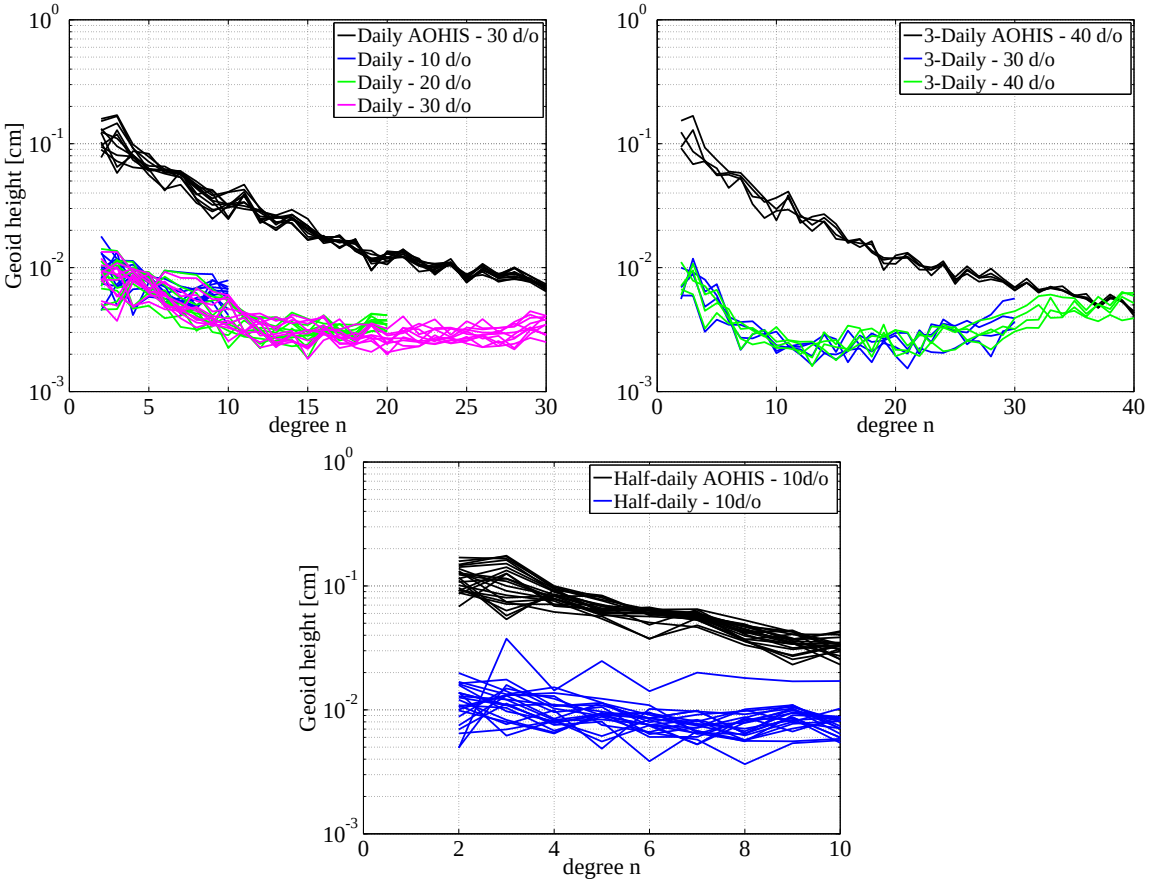

Figure 7.2.3: DDA in geoid heights of solutions estimated at high frequencies. Colored error curves represent temporal aliasing effects due to under-sampling of "AOHIS" signal.

the corresponding SNR for each parameterization. All cases deliver strong SNR values, with the 3-daily d/o 30 case having the strongest. From the daily solutions, the strongest SNR value is achieved by the d/o 20 solutions, while the half-daily solutions deliver the smallest values of all cases. It is also interesting to compare solutions with the same resolution but of different sampling periods. The SNR of daily fields until d/o 10 is larger than the corresponding half-daily ones. This indicates that being sampled at a higher frequency, half-daily estimates may capture larger signal variability, but their estimates might not be as good as the daily ones. The same conclusion is drawn when comparing daily with 3-daily d/o 30 fields. It remains now to be shown, in what way the co-estimation of the low resolution fields contributes to the long-term mean solution.

Fig. 7.2.4 depicts the temporal aliasing effects in terms of DDA geoid heights, for the mean 11-day solutions processed with daily co-estimation of low d/o solutions. Wiese daily parameterization leads to a reduction of temporal aliasing errors for the complete part of the bandwidth for all cases compared to the nominal processing. The longer wavelength part follows the error behavior of daily estimates shown in Fig. 7.2.3, with the error curve representing now the difference between the weighted mean of the daily estimates and the 11-day mean of the "AOHIS" input signal. Concerning the higher bandwidth

Solution	Nr. of gravity field solutions	"AOHIS" Std. deviation (mm)	Aliasing Std. deviation (mm)	SNR
Daily d/o 10	11	2.51	0.25	10
Daily d/o 20	11	2.61	0.24	10.9
Daily d/o 30	11	2.65	0.25	10.6
Half-daily d/o 10	22	2.54	0.31	8.1
3-daily d/o 30	3+"1"	2.59	0.20	13
3-daily d/o 40	3+"1"	2.60	0.24	10.8

Table 7.2: Statistical analysis of the gravity field solutions estimated at high frequencies for a noise-free case. The "AOHIS" signal is estimated at the same expansion as the gravity field solutions and their difference represents temporal aliasing effects. For each parameterization, given is the mean of the standard deviation values over the retrieval time periods.

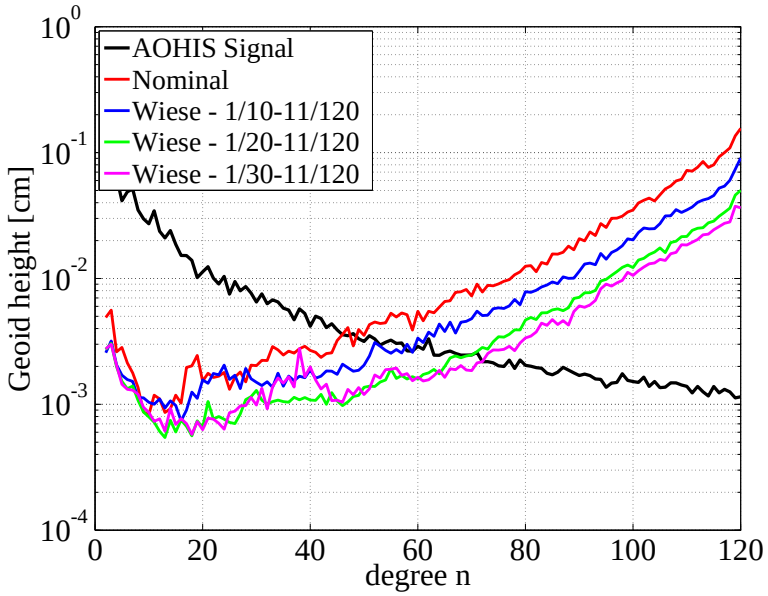

Figure 7.2.4: DDA in geoid heights of 11-day d/o 120 solutions processed with co-parameterization of daily fields (see Table 7.1). Colored error curves represent temporal aliasing effects due to under-sampling of "AOHIS" signal.

part, one can notice that the higher the maximum degree of expansion of the daily solutions, the larger the improvement of the higher degree coefficients. Moreover, the maximum spatial resolution achieved at the spherical harmonic d/o where the SNR equals to one, is increased from d/o 50 (nominal case) to d/o 60 for the Wiese$_{1/10-11/120}$ case, and around d/o 70 for the Wiese$_{1/20-11/120}$ and Wiese$_{1/30-11/120}$ cases. Wiese$_{1/30-11/120}$ case seems to perform best at the short wavelength part of the solution. On the other hand, an error "jump" is evident near the spherical harmonic degree 38, which is not to be noticed for the Wiese$_{1/20-11/120}$ case. This could be attributed to the fact that d/o 30 expansion is close to the

maximum daily resolvable d/o according to Fig. 7.2.2.

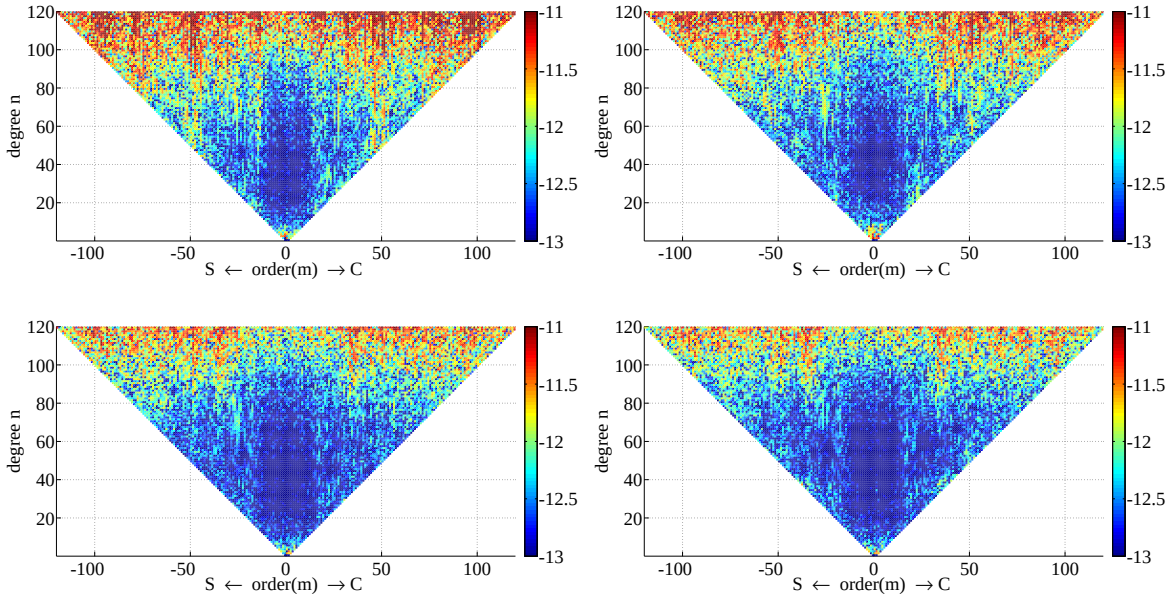

Figure 7.2.5: Coefficient differences of 11-day d/o 120 noise-free solutions. Top-left: Nominal, top-right: $\text{Wiese}_{1/10-11/120}$, bottom-left: $\text{Wiese}_{1/20-11/120}$, bottom-right: $\text{Wiese}_{1/30-11/120}$ (see Table 7.1).

The coefficient differences of the solutions processed with daily Wiese parameterization are depicted in the triangle plots of Fig. 7.2.5. The Wiese parameterization results in an error reduction that is more profound at higher degree coefficients and at orders that are multiples of the number of orbital revolutions (~ 15).

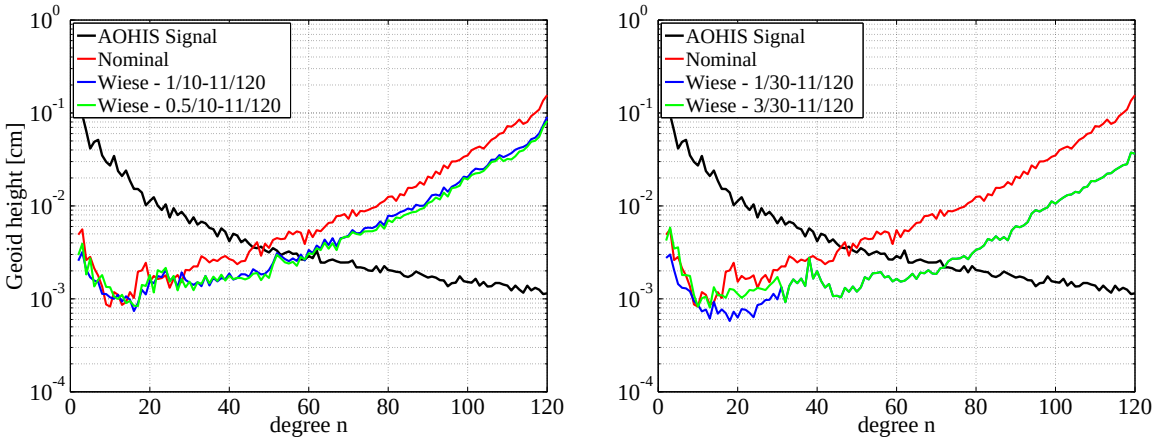

Figure 7.2.6: DDA in geoid heights of 11-day d/o 120 solutions processed with co-parameterization of half-daily (left) and 3-daily fields (see Table 7.1). Colored error curves represent temporal aliasing effects due to under-sampling of "AOHIS" signal.

From a visualization of Fig. 7.2.2, half-daily fields may have a maximum expansion of around d/o

16. However, simulation runs of such an expansion delivered results with severe degradation at the lower degree coefficient bandwidth (not shown). Therefore, a half-daily d/o 10 Wiese parameterization is shown in Fig. 7.2.6-left, where it is also compared with a daily d/o 10 case. Since more signal variability is captured in the half-daily than the daily fields, a larger improvement with the half-daily parameterization is to be expected. However, there is only a marginal improvement for the half-daily case at the coefficients above d/o 40, where for the lower coefficients the error levels are slightly larger. This could be explained by the fact that daily fields have stronger SNR values than half-daily ones.

According to Fig. 7.2.2, 3-daily fields may have a larger expansion than d/o 30. However, Fig. 7.2.3-bottom, shows that SNR values of 3-daily fields are equal to one near d/o 40. This imposes d/o 40 as the resolution limit for 3-daily solutions. Indeed, simulations performed for d/o 40 expansion (Fig. 7.2.14-right in Sec. 7.2.3), delivered a severe increase of the error levels at the intermediate coefficients exceeding the maximum expansion of the 3-daily fields. Fig. 7.2.6-right illustrates the results of a 3-daily parameterization up to d/o 30. Compared to a daily parameterization of the same expansion, 3-daily parameterization delivers identical error curves for coefficients larger than d/o 30, where for the lower coefficients a daily parameterization performs better. This outcome contradicts the quality analysis of the short-term solutions, where the 3-daily solutions have stronger SNR values than the daily ones. This can be explained by the fact that daily solutions contain a larger signal variability than 3-daily, due to the more frequent sampling. The daily parameterization performs therefore better than the 3-daily in the lower coefficient bandwidth, due to a better recovery of the rapid gravity field changes. Thus, the sampling frequency plays also an important role for the mitigation of temporal aliasing effects at the coefficient bandwidth of the co-estimated low-resolution fields. One of the reasons for parameterizing on a 3-daily basis, was also to investigate the benefits of the repeatability that a sub-cycle can offer. However, the 3-daily sub-cycle holds only for the polar pair, and its effect diminishes in case of the Bender constellation, where the sampling of two pairs is interlaced. However, results of daily parameterization for the polar pair still showed larger improvements than 3-daily (not shown), as it was the case for the Bender constellation. Therefore, parameterizing at periods equal to sub-cycles of orbits, is not a prerequisite for a successful reduction of temporal aliasing effects. After all, a period of one day is itself kind of a “sub-cycle” for near-polar LEO satellites.

7.2.2 Noise-case analysis

The following section investigates different Wiese parameterization choices, for a case where all errors but de-aliasing model inaccuracies (see Sec. 7.1.2) are considered. The solutions refer to the same period as the noise-free solutions, and they are processed with frequency dependent data weighting and co-parameterization of arc-wise linear empirical accelerations. Fig. 7.2.7 depicts the error levels of the same short period fields as in Fig. 7.2.3, but for the noise case. As it was expected, the DDA curves of the high-frequency solutions are closer to the signal curves than in the noise-free case. The stronger presence of noise is also confirmed by their SNR values shown in Table 7.3, which are considerably smaller than for the error-free case (Table 7.2).

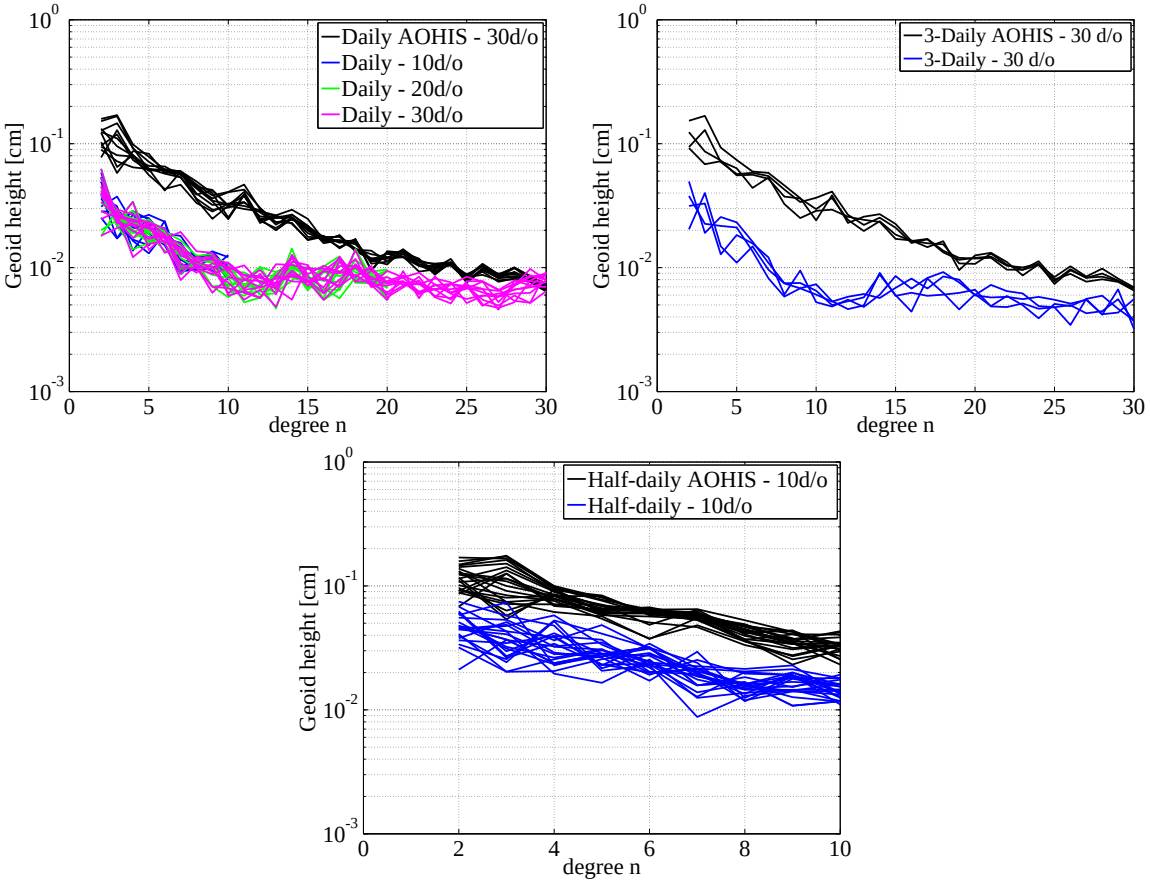

Figure 7.2.7: DDA in geoid heights of solutions estimated at high frequencies. Processing includes all errors sources but de-aliasing model inaccuracies.

Solution	Nr. of gravity field solutions	"AOHIS" Std. deviation (mm)	Error Std. deviation (mm)	SNR
Daily d/o 10	11	2.51	0.68	3.7
Daily d/o 20	11	2.61	0.70	3.7
Daily d/o 30	11	2.65	0.72	3.6
Half-daily d/o 10	22	2.54	0.87	2.9
3-daily d/o 30	3+"1"	2.59	0.64	4

Table 7.3: Statistical analysis of the gravity field solutions estimated at high frequency for the noise case. The "AOHIS" signal is estimated at the same expansion as the gravity field solutions. For each parameterization, given is the mean of the standard deviation values over the retrieval time periods.

Compared to the nominal processing, the Wiese daily parameterization leads to an error reduction in the coefficient bandwidth larger than d/o 40 for the Wiese$_{1/10-11/120}$ and Wiese$_{1/20-11/120}$ cases. Comparing the results of the error-free case (Fig. 7.2.4) with the noise case (Fig. 7.2.8), it can be concluded that the higher the maximum degree of expansion of the daily solutions, the larger the improvement of the higher degree coefficients. However, unlike the noise-free case, the lower coefficients do not show improvements compared to the nominal processing. The Wiese$_{1/20-11/120}$ solution leads to larger improvements than the Wiese$_{1/10-11/120}$, in the coefficient bandwidth above d/o 40. An error increase near the second band of spherical harmonic resonance orders is noticed. This can be attributed to the fact that the daily fields of the Wiese$_{1/10-11/120}$ solution include the first resonance order of the polar pair (15), where usually large amount of error is gathered. This small drawback can be compensated by the fact that the gain in the largest part of the coefficient bandwidth is substantially larger compared to Wiese$_{1/10-11/120}$, which does not contain the first resonance order. At last, the Wiese$_{1/30-11/120}$ case results in a large error increase near d/o 40, which can be attributed to the fact that d/o 30 is close to the maximum daily resolvable expansion, and that the SNR values for the daily gravity fields near d/o 30 are equal or even less than one. Moreover, along with first resonance, d/o 30 fields contain additionally the second resonance order terms. Thus, they absorb an even larger part of the error that would otherwise map into multiples of the resonant order terms at much higher degrees. This results in an error increase after the cut-off degree, which is larger than in case of d/o 20.

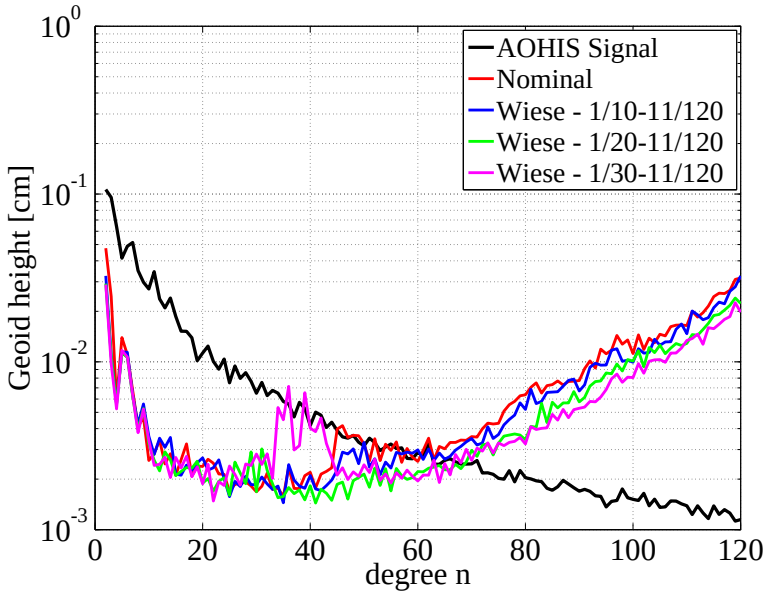

Figure 7.2.8: DDA in geoid heights of 11-day d/o 120 solutions processed with co-parameterization of daily fields (see Table 7.1). Processing includes all errors sources but de-aliasing model inaccuracies.

Fig. 7.2.9 displays the results of half-daily and 3-daily parameterization for the noise case. The half-daily and 3-daily parameterization perform worse than the noise-free case. Nevertheless, the conclusions are similar. Daily parameterization captures best the geophysical phenomena that normally alias into the mean solutions.

As a next step, a spectral analysis of the pre-fit and post-fit residuals for the best case (i.e.

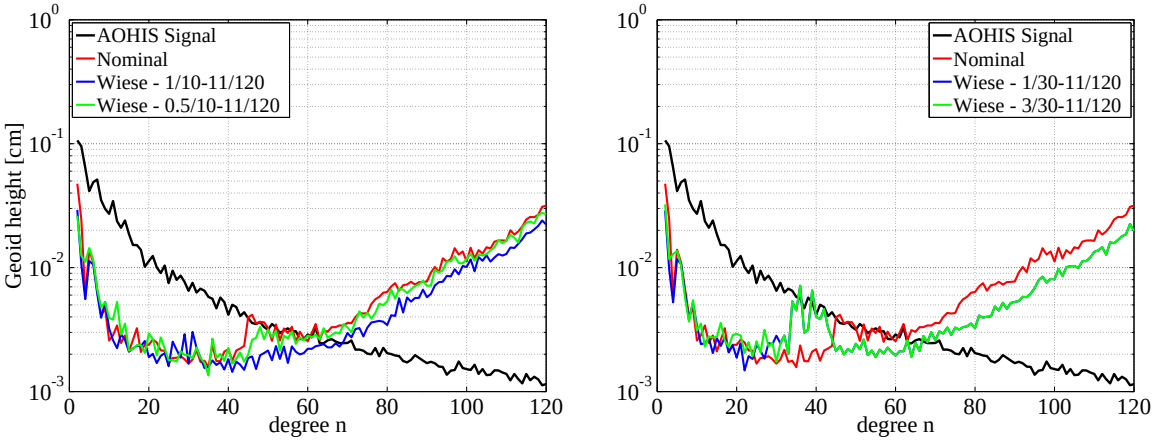

Figure 7.2.9: DDA in geoid heights of 11-day d/o 120 solutions processed with co-parameterization of half-daily (left) and 3-daily fields (see Table 7.1). Processing includes all errors sources but de-aliasing model inaccuracies.

$\text{Wiese}_{1/20-11/120}$) was performed. Figs. 7.2.10 and 7.2.11 summarize the results for the polar and inclined pair respectively, where both HL-SST and LL-SST components are depicted. The residuals are expressed in the CRF. This time, the estimated daily coefficients up to d/o 20 are also taken into account (as part of the local parameters) for the computation of the post-fit residuals. For the polar pair, error peaks are experienced at frequencies that are multiples of 1-cpr (~ 0.18 mHz) for all cases but the cross-track direction of the HL-SST component, where they appear at multiples of the short-arc length (~ 0.56 mHz). The oscillations at multiples of 1-cpr are evident for all cases of the inclined pair, but are less pronounced for the cross-track direction and, interestingly, also for the LL-SST component. The latter phenomenon is related to the sampling geometry of the inclined pair, since the East-West sensitivity (cross-track) is stronger compared to the polar pair. The 1-cpr oscillations of the post-fit residuals are mitigated for both pairs compared to the pre-fit residuals, which comes as a result of the applied error reduction method (i.e. data weighting and empirical parameterization). In cases where the 1-cpr oscillations are present, the daily Wiese parameterization brings a further, more radical reduction of their effect, and a general reduction of the error levels. In those cases however, Wiese parameterization causes an error increase near the frequency of 4 mHz. The degree of expansion l is related to the frequency f by :

$$l = \frac{f \alpha T_e}{\beta + \alpha}, \tag{7.5}$$

where for a full repeat cycle, α is the number of Earth's rotations w.r.t. the satellite's precessing orbital plane in nodal days, β the total number of orbital revolutions performed and T_e the time period of a nodal day in seconds. Applying Eq. (7.5) for the polar pair, we conclude that the error increase at the bandwidth $0.3 \sim 5.5$ mHz corresponds to degree $16 \sim 26$, which includes the resolution of the daily gravity field solutions. Therefore, it is of the same nature as the error increase of the DDA values near d/o 30 in Fig. 7.2.8. Finally, Fig. 7.2.12 depicts the geoid height differences of noise-case d/o 120

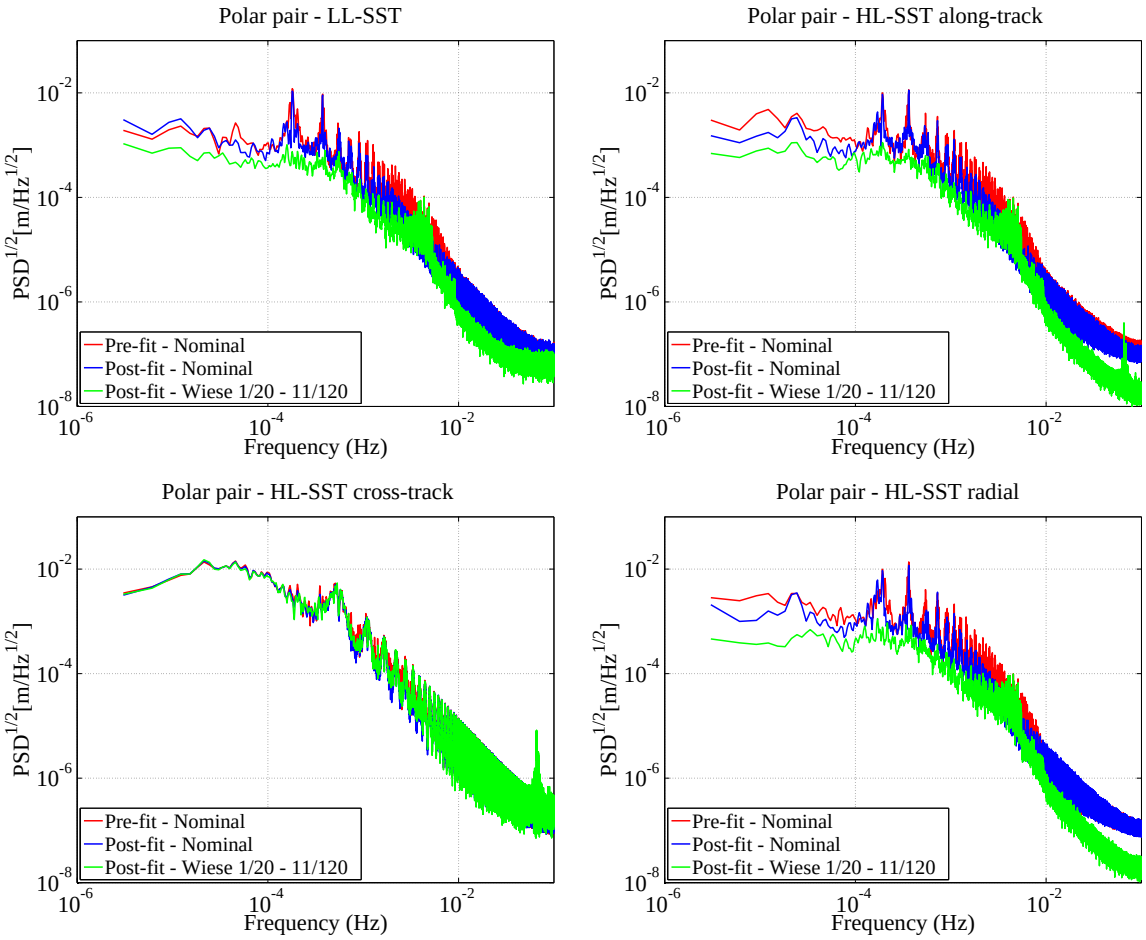

Figure 7.2.10: ASD of pre-fit and post-fit residuals of the polar pair.

solutions, processed with nominal and Wiese daily parameterization. Wiese parameterization results in a clear reduction of the stripes caused by aliasing. The Wiese solutions show also a more isotropic error distribution. The standard deviation values of the closed-loop simulations are improved from 1.14*mm* to 0.89*mm* in terms of geoid height differences.

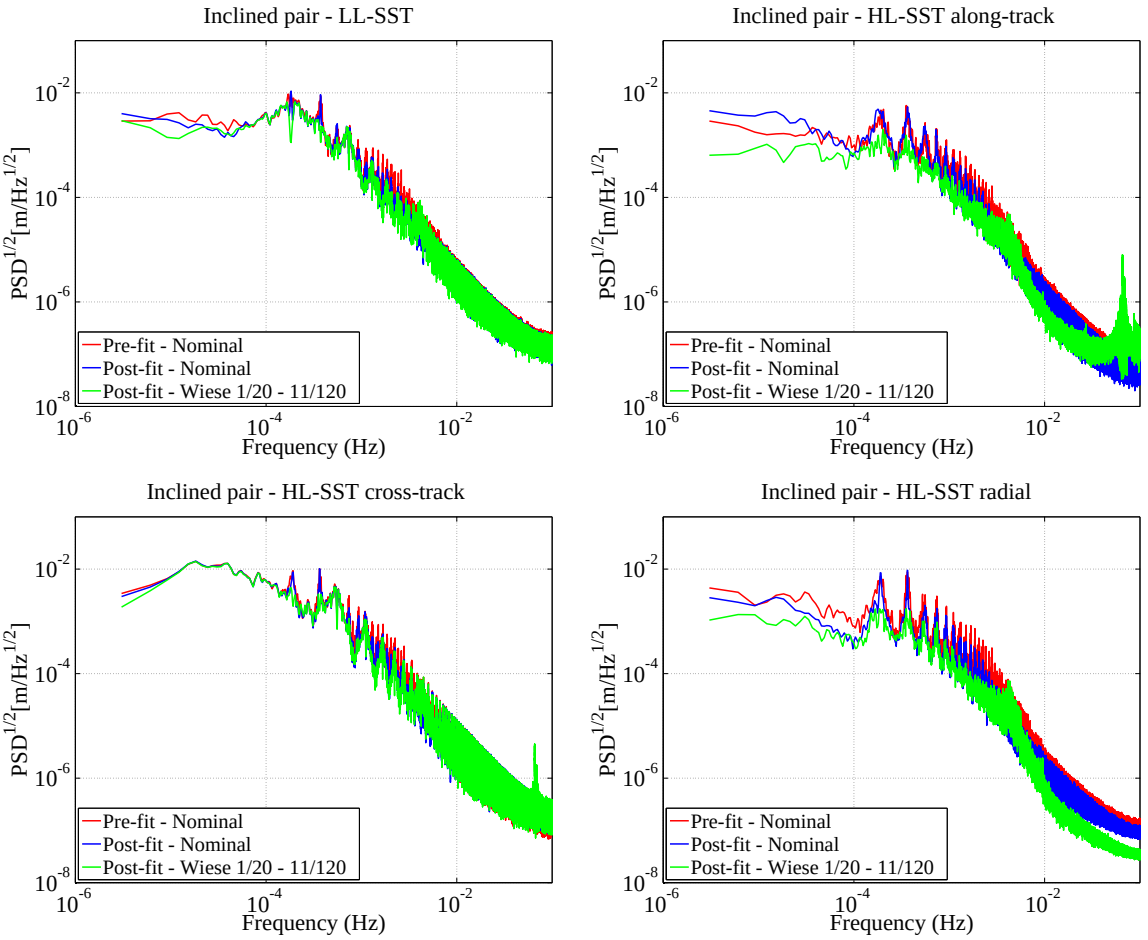

Figure 7.2.11: ASD of pre-fit and post-fit residuals of the inclined pair.

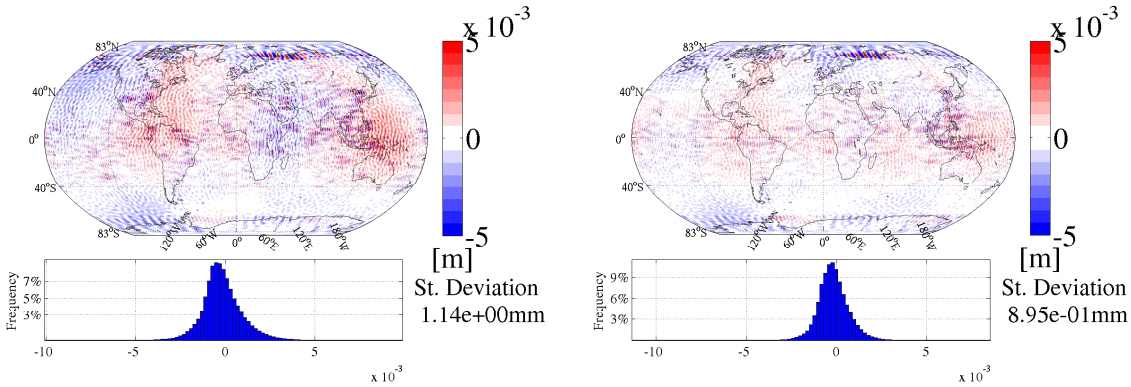

Figure 7.2.12: Closed-loop geoid height differences of 11-day d/o 120 solutions. Left: nominal processing, right: processing with co-parameterization of daily d/o 20 fields (see Table 7.1). Processing includes all errors sources but de-aliasing model inaccuracies.

7.2.3 Sequential co-parameterization

The key element for reducing temporal aliasing effects with the Wiese approach is to capture as much signal variability as possible within the high-frequency estimated gravity field solutions. Parameterizing in single time periods though, has certain limitations when it comes to the signal variability that can be captured. Moving a step further, one can think of taking advantage of the additional space before the blue curve in Fig. 7.2.2, that is left unexploited from a single-period parameterization. This additional signal variability can be recovered by means of a two-step approach which we call *sequential co-parameterization*, and is achieved in 3 steps :

1. The high degree gravity field coefficients (e.g. from 40 to 120 d/o) are estimated with the same method as for the Wiese parameterization.

2. The high degree gravity field coefficients are used for the co-estimation of gravity field solutions at a larger time period (e.g. 3 days) with back-substitution of the pre-eliminated parameters. The weighted mean of the gravity field coefficients from those solutions is then computed, and the intermediate bandwidth (e.g. from 30 to 40 d/o) is kept while the lower coefficients are thrown away.

3. The intermediate together with the high degree gravity field coefficients, form one set of coefficients that is used in a next step for the co-estimation of the daily gravity field solutions. The weighted mean of those solutions provide then the low degree gravity field coefficients.

Fig. 7.2.13 depicts two examples of sequential co-parameterization. Especially the right plot of Fig. 7.2.13 demonstrates the ability of the two colored rectangles to recover signal beyond the limits of a daily parameterization which is at a maximum expansion of d/o 30. Sequential parameterization considers additionally the part covered by the beige rectangle, by co-estimating daily up to d/o 30 and 3-daily from 31 to 40 d/o. Table 7.4 summarizes the details behind the cases investigated.

Parameterization	Short periods		Intermediate periods		Long period	
	days	max. d/o	days	max. d/o	days	max. d/o
$\text{Wiese}_{1/20-3/30-11/120}$	1	20	3	30	11	120
$\text{Wiese}_{1/30-3/40-11/120}$	1	30	3	40	11	120

Table 7.4: Investigated cases of sequential co-parameterization.

Fig. 7.2.14 shows the results of the two cases investigated with sequential co-parameterization, for a noise-free processing. The results of the right plot belong to a parameterization which is at the edge of the resolution limits (according to the findings of Sec. 7.2.1), whereas the left plot shows the results of a more moderate parameterization. Results from daily and 3-daily parameterization are also shown

for reasons of comparison. In both plots, the error curves of the sequential co-parameterization follow the ones from 3-daily in the bandwidth larger than the cut-off degree of the high coefficients (i.e. d/o 30 for Fig. 7.2.14-left, d/o 40 for Fig. 7.2.14-right). Sequential co-parameterization performs also better than 3-daily, in the lower degree bandwidth up to the cut-off degree of the intermediate coefficients (i.e. d/o 20 for Fig. 7.2.14-left, d/o 30 for Fig. 7.2.14-right), as a result of the daily parameterization. The expected improvements compared to a single daily parameterization are achieved for the higher degree coefficients. However, at the bandwidth of intermediate coefficients (i.e. d/o 21 ~ 30 for Fig. 7.2.14-left, d/o 31 ~ 40 for Fig. 7.2.14-right), temporal aliasing effects are reduced more effectively by a daily parameterization. On the other hand, the cyan curve in Fig. 7.2.14-left reveals a marginal gain in terms of spatial resolution w.r.t. the blue one and still maintains lower error levels than the nominal processing (red curve). In case of Wiese$_{1/30-3/40-11/120}$, it was expected to gain some improvements compared to the single daily parameterization at the resolution limits of d/o 30. However, a large error increase after d/o 40, implies that the resolution limits for the 3-daily fields are also exceeded from a choice larger than d/o 30.

From the noise-free simulations, it can be concluded that a daily parameterization is more suitable than a sequential for reducing temporal aliasing effects in case of a 11-day Bender solution. This outcome is also confirmed by the noise-case simulation illustrated in Fig. 7.2.15. A daily parameterization with a maximum resolution of d/o 20 remains the best choice for reducing the error levels in the solutions, since it provides the best compromise between the largest possible amount of signal to be captured and

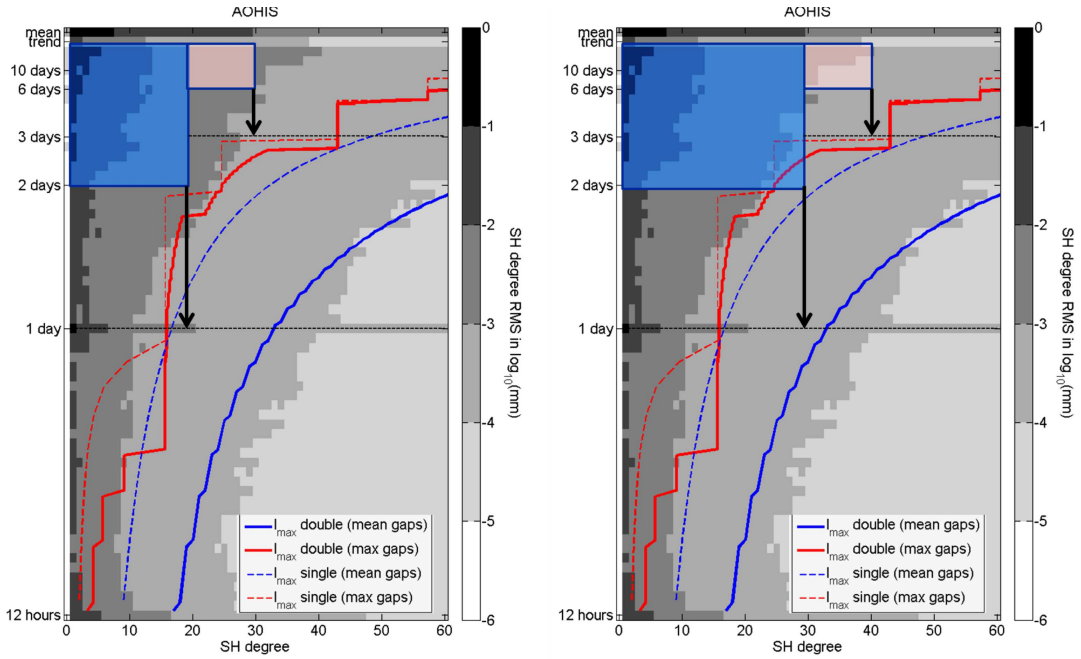

Figure 7.2.13: Consolidation of sequential co-parameterization choices. X-axis stands for the spatial and Y-axis for the temporal resolution. Dashed rectangles represent the retrievable "AOHIS" signal for given periods and resolution according to the Nyquist theorem.

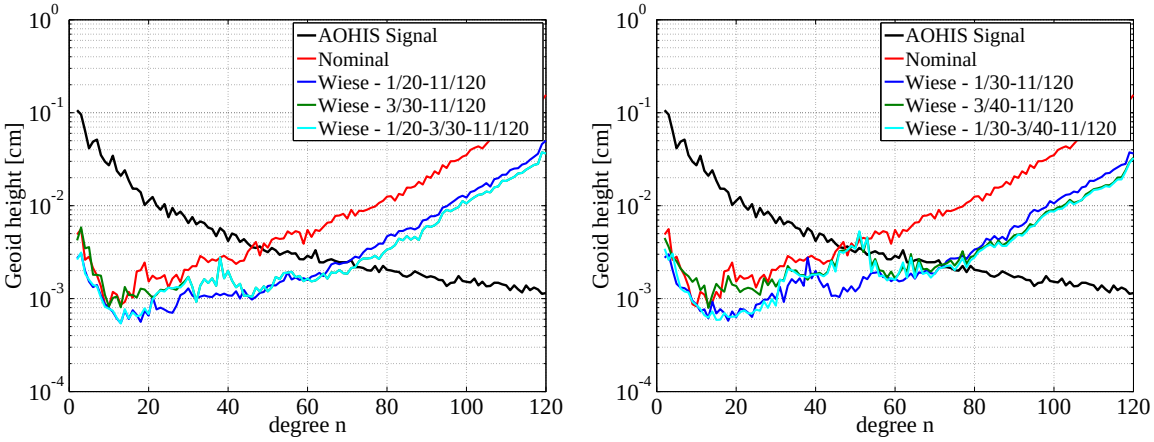

Figure 7.2.14: DDA in geoid heights of 11-day d/o 120 solutions processed with sequential co-parameterization of daily and 3-daily fields for a noise-free case(see Table 7.4). Colored error curves represent temporal aliasing effects due to under-sampling of "AOHIS" signal.

the shortest time period in which it changes.

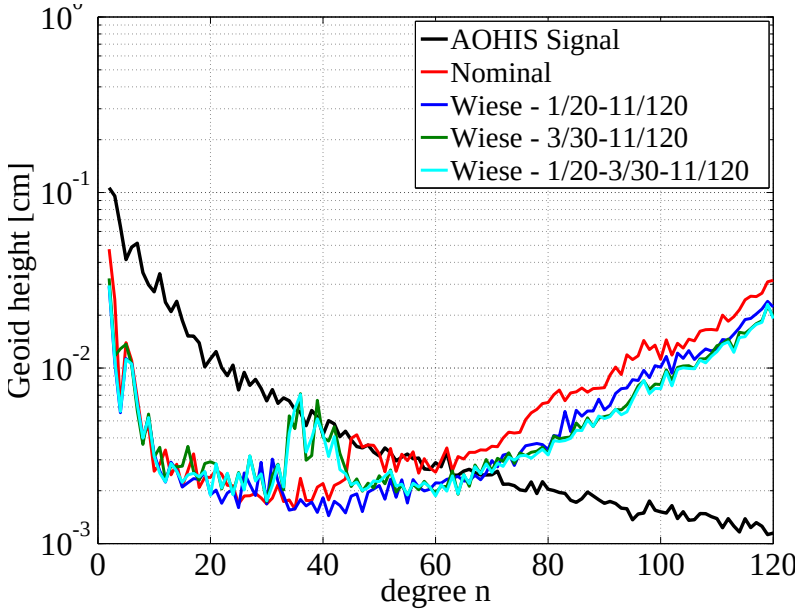

Figure 7.2.15: DDA in geoid heights of 11-day d/o 120 solutions processed with sequential co-parameterization of daily and 3-daily fields for a noise case(see Table 7.4). Processing includes all errors sources but de-aliasing model inaccuracies.

7.2.4 Assessment of individual aliasing components

Previous sub-sections were dedicated to the treatment of aliasing effects induced by the sum of all aliasing sources. However, it is also of high importance to quantify the contribution of the individual aliasing components to the error-budget, and the ability of Wiese parameterization to absorb them. For that case, a $\text{Wiese}_{1/20-11/120}$ co-parameterization was considered. The components investigated, consist of geophysical signals with strong variations at high frequencies, namely atmosphere "A", ocean "O" and

hydrology “H” (ice “I” and solid Earth “S” were not examined), as well as ocean tide model inaccuracies. All cases considered noise propagation of sensor errors. In case of the geophysical signals, processing excluded the effect of ocean tide model inaccuracies. Consequently, for investigating the aliasing effect of ocean tide model inaccuracies, processing excluded the use of any other temporal variations of the gravity field. By this, the effect of all aliasing components was assessed individually in the presence of sensor errors. Table 7.5 provides statistical analysis for the daily fields of the individual geophysical

Component	Solution	Nr. of gravity field solutions	“A”, “O”,“H” Std. deviation (mm)	Error Std. deviation (mm)	SNR
Atmosphere “A”	Daily d/o 20	11	1.8	0.37	4.9
Ocean “O”	Daily d/o 20	11	1.4	0.35	4
Hydrology “H”	Daily d/o 20	11	0.78	0.31	2.5

Table 7.5: Statistical analysis of the gravity field solutions estimated at high frequency for the individual components “A”, “O” and “H”. For each component, the signal is estimated at the same expansion as the gravity field solutions. For $\text{Wiese}_{1/20-11/120}$ parameterization, given is the mean of the standard deviation values over the retrieval time periods.

signals. As expected, the most variability contained in the daily “AOHIS” fields comes from atmosphere. The daily atmospheric fields exhibit also the strongest SNR values, followed by the oceanic fields. The hydrological variations in daily intervals have considerably weaker variation and SNR values than the other components. Therefore, the daily co-parameterization in case of hydrology is expected to exhibit the smallest improvements. Results of the simulations performed for the individual geophysical signals are depicted at Figs. 7.2.16 and 7.2.18. Indeed, the best error reduction is performed in case of atmosphere, which induces also the largest aliasing effects. It is worth noticing, that the improvements hold for the whole bandwidth of coefficients. In case of the ocean signals, aliasing and improvements from the Wiese parameterization are less prominent. A degradation at the second resonance band (i.e. d/o 30) is evident. This error increase is present in the Wiese parameterization of all three “A”, “O” and “H” components, and is caused by including the first orbit resonance term at the daily d/o 20 fields. Aliasing induced by hydrology is only marginally improved for coefficients higher than d/o 40, where at longer wavelengths results are even degraded.

Figs. 7.2.17 and 7.2.18-bottom-right, depict the results of processing with ocean tide model errors. Their aliasing effects constitute the next major contributor to the aliasing error budget along with the aliasing caused by the under-sampling of atmosphere. Contrary to the atmospheric component, aliasing due to the ocean tide model errors does not show the same reduction when processed with the Wiese

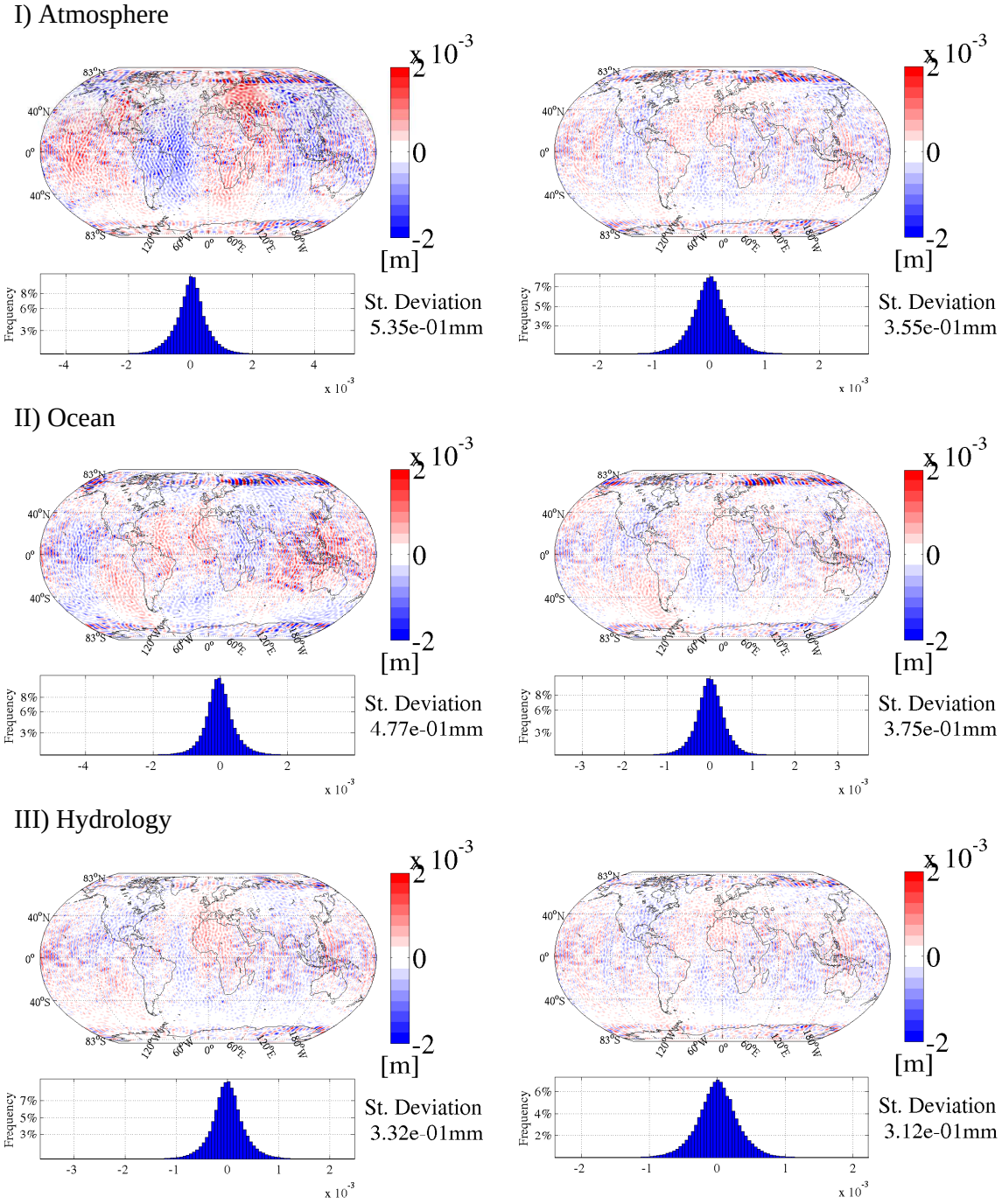

Figure 7.2.16: Closed-loop geoid height differences of 11-day d/o 120 solutions for individual geophysical components. Left: nominal processing, right: processing with co-parameterization of daily d/o 20 fields. All errors sources included but de-aliasing model inaccuracies and ocean tide model errors.

approach. In fact, it remains the biggest contributor to the error budget and dominates the error spectrum at the low to intermediate degrees, until the maximum expansion of the two different ocean tide models

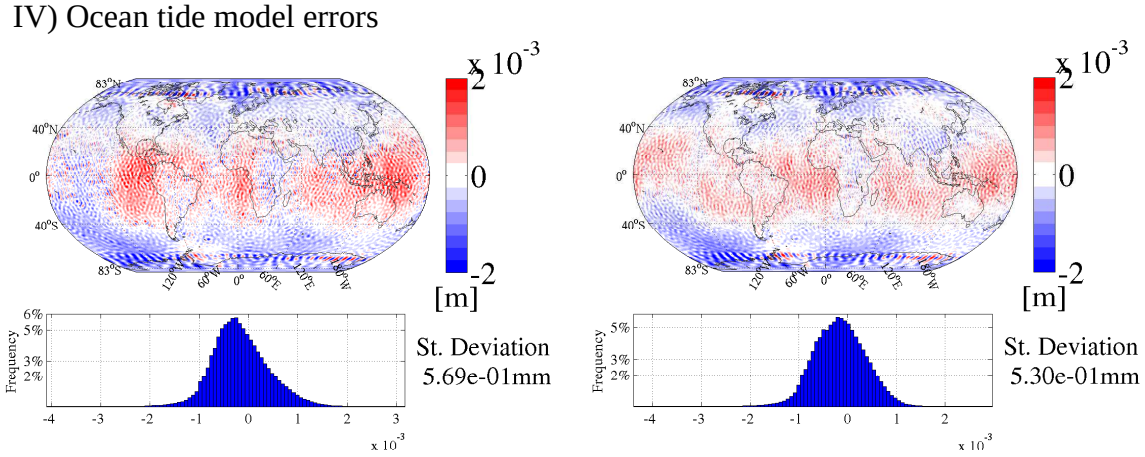

Figure 7.2.17: Closed-loop geoid height differences of 11-day d/o 120 solutions processed with ocean tide model and sensor errors. Left: nominal processing, right: processing with co-parameterization of daily d/o 20 fields. No temporal gravity field variations have been considered.

used (d/o 50) is reached. Around that degree an error increase is manifested, which is attributed to the strict cut-off of their contribution at this expansion. On the other hand, the error increase near d/o 30 present at the previous cases is not to be witnessed. This could predispose a weaker sensitivity of the error behavior, in this case, to the content of the daily fields. As expected, the daily parameterization can hardly capture the main ocean tide signals with daily or even half-daily periods. On the other hand, this might indicate that a daily Wiese parameterization might not be strongly correlated with a dedicated parameterization of ocean tide signals. A proper treatment of errors induced from ocean tide model inaccuracies involves co-estimation of tidal constituents at their aliasing periods, using very long observation time series of nearly a decade. This requires a sophisticated parameterization in case of a Bender constellation, where the estimation of tidal aliasing periods is not so trivial as for a polar pair, and is beyond the scope of this study.

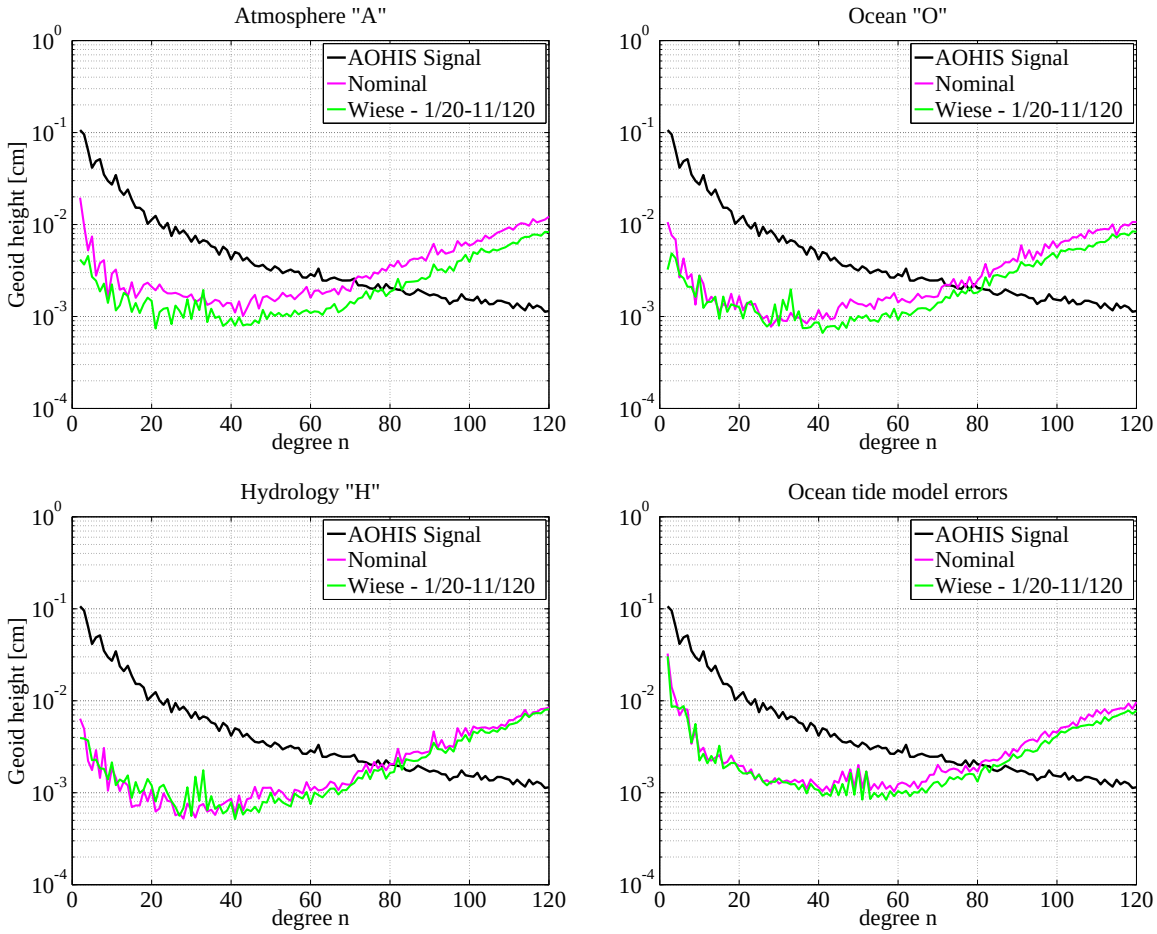

Figure 7.2.18: DDA in geoid heights of 11-day d/o 120 solutions of individual components inducing aliasing effects. Depicted are error curves of nominal and Wiese$_{1/20-11/120}$ solutions.

7.2.5 Processing of an alternative constellation

In order to investigate the effect of the orbit choice on the aliasing reduction method, an alternative constellation has been selected and processed for both nominal and Wiese$_{1/20-11/120}$ parameterization. Table 7.6 summarizes the orbit details of the alternative constellation, with the major differences from the baseline constellation being the following :

- The two pairs exhibit much longer repeat cycles and sub-cycles. In fact, the repeat cycles of both pairs (130 and 131 days) are much longer than the solution period of 11 days. This was not the case for the polar pair of the baseline constellation, which experienced a full cycle exactly after 11 days.
- The polar pair has a prograde orbit instead of a retrograde one.
- The inclined pair has an inclination closer to 90^o,which allows for a larger region to be sampled with two pairs.

Altitude (km)	Inclination (deg)	Inter-satellite distance (km)	β/α (rev./day)	sub-cycle (days)
		Polar pair		
362	89.5	100	2031/130	61
		Inclined pair		
329	70	100	2047/131	8

Table 7.6: Configuration setup of the orbits for the alternative constellation

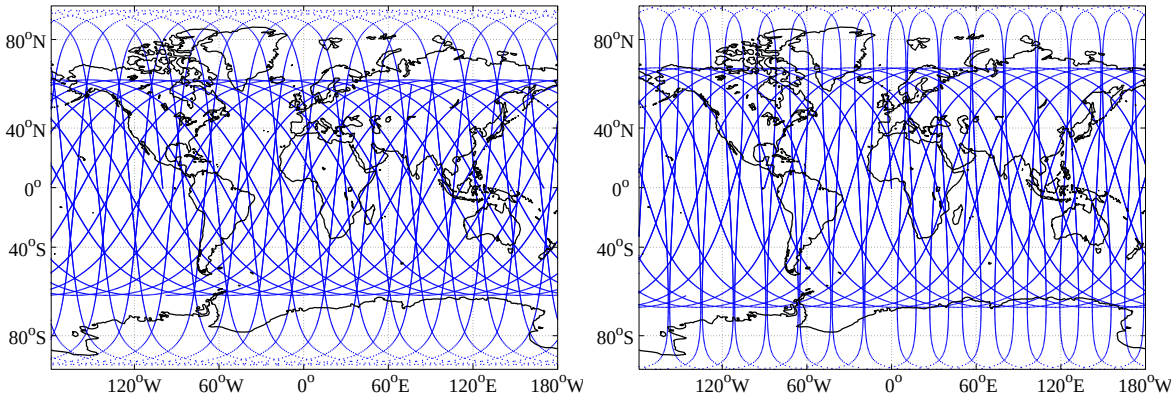

Figure 7.2.19: Spatial ground-track coverage of both pairs of the Bender constellation for the period of 1 day. Left: baseline constellation, right: alternative constellation.

Fig. 7.2.19 depicts the spatial coverage of both pairs for the period of 1 day for both constellations. It is evident that the inclined pair of the alternative constellation covers a larger part of the Earth than the inclined pair of the nominal one. One can also notice that the spatial coverage in 1 day is more or less homogeneous at the same level as for the nominal constellation. This is an important aspect for the effectiveness of the Wiese parameterization.

An 11-day gravity field solution of "AOHIS" signal was generated both for the nominal, as well as for the Wiese case, for the same time period and noise assumptions. The nominal processing for the alternative constellation delivers a solution with accuracy comparable to the baseline one. An inspection of the DDA values (red curves at Fig. 7.2.20) reveals similar error levels for the two constellations. The spatial plots of the errors expressed in geoid undulations (Fig. 7.2.22) reveal a different error pattern. The latitudinal stripes at the very high and low latitudes, which are attributed to the loss of the inclined pair at these regions, are restricted to a smaller area near the poles. This results from the higher inclination choice of the inclined pair. The improvement in those regions is also observable at the triangle plots of the coefficient differences (Fig. 7.2.21-left), where the typical "butterfly" pattern is less pronounced and nar-

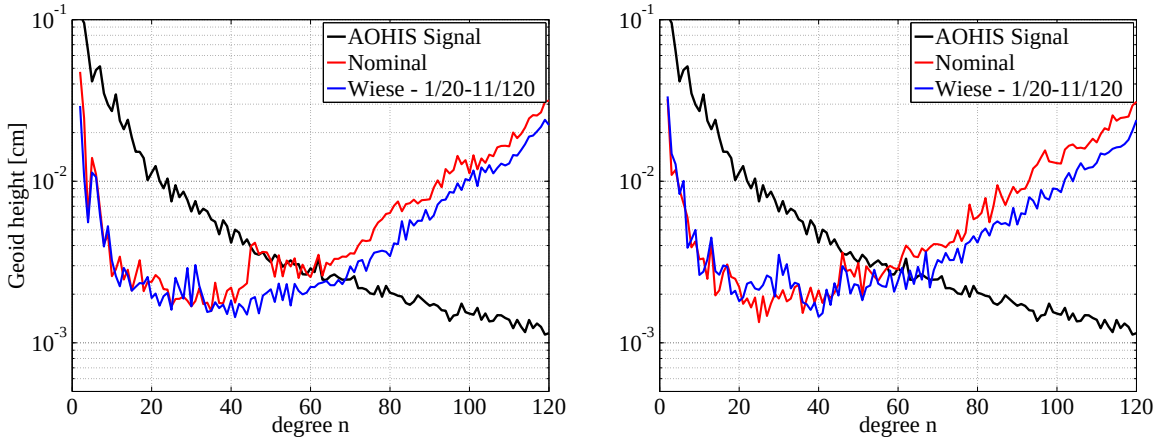

Figure 7.2.20: DDA in geoid heights of 11-day d/o 120 solutions of individual components inducing aliasing effects. Depicted are error curves of nominal and Wiese$_{1/20-11/120}$ solutions.

rower than for the baseline constellation. Processing the alternative constellation with Wiese$_{1/20-11/120}$

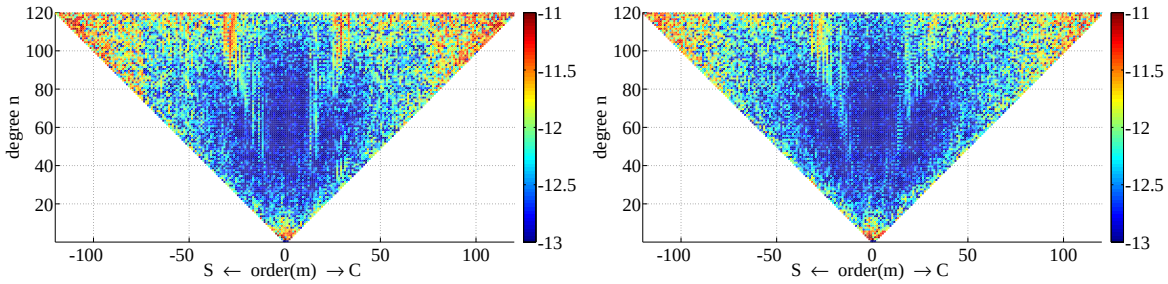

Figure 7.2.21: Coefficient differences of 11-day d/o 120 noise-case solutions of the alternative constellation. Left: nominal processing, right: Wiese$_{1/20-11/120}$ processing (Table 7.1).

parameterization delivers improved solutions compared to the nominal parameterization. The level of improvement is comparable to that of the baseline constellation. However, the error increase at twice the resonant frequency (i.e. d/o 30) is more prominent than for the baseline constellation. This could be related to the higher noise levels of the daily fields in case of the alternative constellation (SNR=3.4 compared to SNR=3.7 for the baseline). Both constellations have a maximum spatial resolution of 285 km half-wavelength. Comparing the geoid plots of Fig. 7.2.22-right and 7.2.12-right, one can notice a more "stripy" behavior for the alternative constellation overall except for the regions of higher latitudes, where the error levels are reduced. This is also confirmed by the coefficient triangle plot of Fig. 7.2.21, where the "butterfly" effect is also reduced. A degradation of the low-to-intermediate sectorial coefficients compared to nominal parameterization can also be observed. The improvements in the high latitude regions, come at the expense of a noisier performance in the intermediate-to-low latitudes, as a result of the smaller amount of observations. Counter-balancing this effect, will therefore be an open

question for mission design of NGGMs. A possible solution of the issue could be to treat the latitudinal stripes at the transition zones with a suitable spatial filtering.

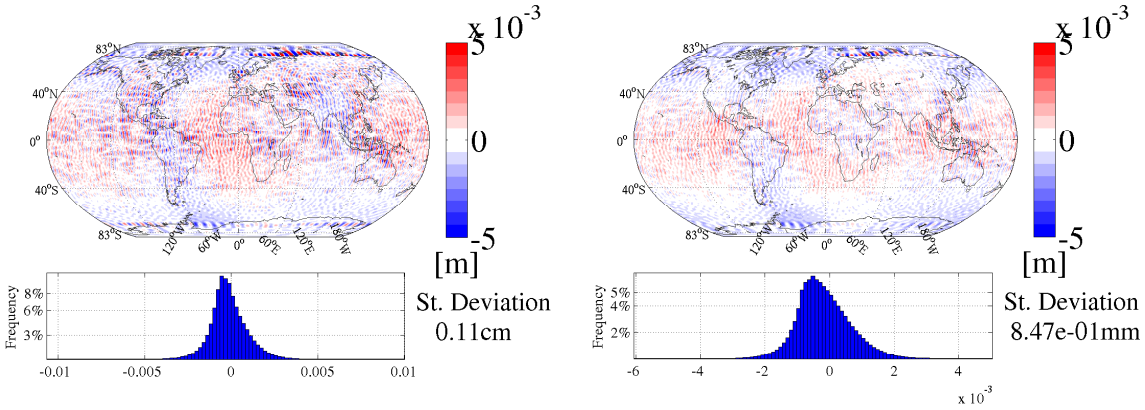

Figure 7.2.22: Closed-loop geoid height differences of 11-day d/o 120 solutions for the alternative constellation. Left: nominal processing, right: Wiese$_{1/20-11/120}$ processing (Table 7.1).

An important conclusion from processing with the alternative constellation is that Wiese parameterization led to similar improvements in the medium-to-short wavelengths and increase of spatial resolution. Consequently, there are strong indications that the performance of Wiese processing in this coefficient bandwidth, is rather insensitive to the orbit choice of cycles or sub-cycles. The only prerequisite seems to be a uniform sampling of the parameterized periods (here 1 day). Nevertheless, the SNR values of daily fields, do play a role for the error increase at the second band of the orbit resonance. This could facilitate mission design of NGGMs, in having no strict constraints for specific repeat periods, or a retrograde orbit, as far as the efficiency of Wiese processing in increasing spatial resolution is concerned. Fine-tuning of the parameterization choices is nevertheless of crucial importance.

7.3 Retrieval content of NGGM gravity field solutions

In Sec. 7.1.2, the ability of NGGMs in retrieving the full "AOHIS" signal was discussed. Here, we address this argument once again in order to enrich it with the insights gained from treating temporal aliasing errors by co-estimating low resolution gravity fields at higher temporal frequencies.

One of the most important findings from processing with Wiese parameterization, is that the method treats aliasing effects induced by under-sampling of atmosphere and ocean signals in a very suitable manner. This is achieved through a retrieval of the strong signal variability at short-term scales, and a successful assignment of their influence to the mean 11-day solution. It was also shown that due to its weak variability at high frequencies, hydrology does not contribute drastically to the aliasing error budget, and consequently does not gain much from the Wiese parameterization. This holds also for the augmented case of "HIS" signals, where the variability of Ice "I" and Solid Earth "S" has a much longer-term behavior. Solving for "HIS", involves use of "AO" de-aliasing models with inaccuracies that alias

into the mean solution. Wiese parameterization can also reduce these aliasing effects, since they are also contained in the short-term solutions. The big difference though compared to solving for "AOHIS", is that the short-term solutions contain the effect of "HIS + AO errors" instead of "AOHIS". This is an additional noise source being present in the short-term fields, that could diminish also the effectiveness of Wiese parameterization.

Strategy	Input	"On-the-fly" De-aliasing (6-hourly)	Output	A posteriori reduction (11-day mean)
1	"AOHIS"	"AO + AOerr"	"HIS"	-
2	"AOHIS"	-	"AOHIS"	"AO + AOerr"

Table 7.7: Strategies for retrieving "HIS" gravity field solutions

Products of LL-SST missions like GRACE and hopefully also GRACE-FO, are extremely useful to many fields of geosciences. However, they have been particularly helpful for hydrological and water cycle observation purposes. As mentioned before, the gravity field solutions provided by the GRACE processing centers include the "HIS" part of the signal. That makes those fields handy for those thematic fields to use. In case NGGMs deliver the full "AOHIS" signal, the users interested in "HIS" will have to use "AO" models to separate them from the "HIS" target signal. The error characteristics of such an a posteriori signal separation, was compared to the classical "on-the-fly" de-aliasing performed so far by the processing centers. Table 7.7 gives a description of the 2 different strategies for retrieving "HIS" signal. Fig. 7.3.1 shows the results of retrieving "HIS" gravity field solutions using both strategies.

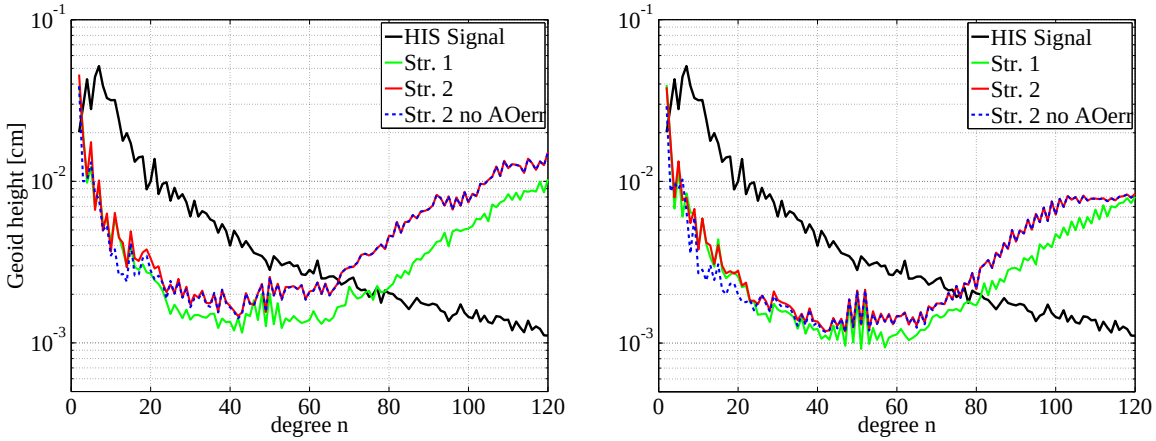

Figure 7.3.1: DDA in geoid heights of 11-day d/o 120 "HIS" solutions using both retrieving strategies. Left: nominal processing, right: Wiese$_{1/20-11/120}$ processing (Table 7.1).

Results from strategy 2 include a case where the a posteriori subtraction of "AO errors" is considered (red curves), and a case where it is not (blue dashed curves). Fig. 7.3.1-left depicts the results of a

nominal, where Fig. 7.3.1-right of a Wiese$_{1/20-11/120}$ processing. The two strategies deliver similar results for the nominal processing until d/o 20, where results from Strategy 2 start to reveal a higher noise level. This is most probably attributed to the higher aliasing error levels induced by under-sampling of "AOHIS", compared to "HIS" signal. The effect of the de-aliasing "AO" model errors, can only be quantified at an a posteriori basis, by comparing the red with the blue dashed curves. On the other hand, Wiese parameterization leads to error levels that are closer for the two strategies. The error levels for Strategy 2 begin to degrade for coefficients larger than d/o 40 compared to Strategy 1. The difference in maximum spatial resolution is also smaller. This error convergence is related to the fact that Strategy 2 shows larger improvements when processed with Wiese parameterization. Spatial plots of closed-loop geoid height differences depicted in Fig. 7.3.2, reveal that the main differences from the two strategies processed with Wiese parameterization are located in the transition zones, where information from the inclined pair is gradually unavailable. The spatial plots show differences and statistics from a latitude band-limited area with $-65^o \leq \text{lat} \leq 65^o$. Nominal processing results in a noisier pattern for Strategy 2, while Wiese processing delivers similar error patterns, and standard deviation values that differ only by $10\mu m$.

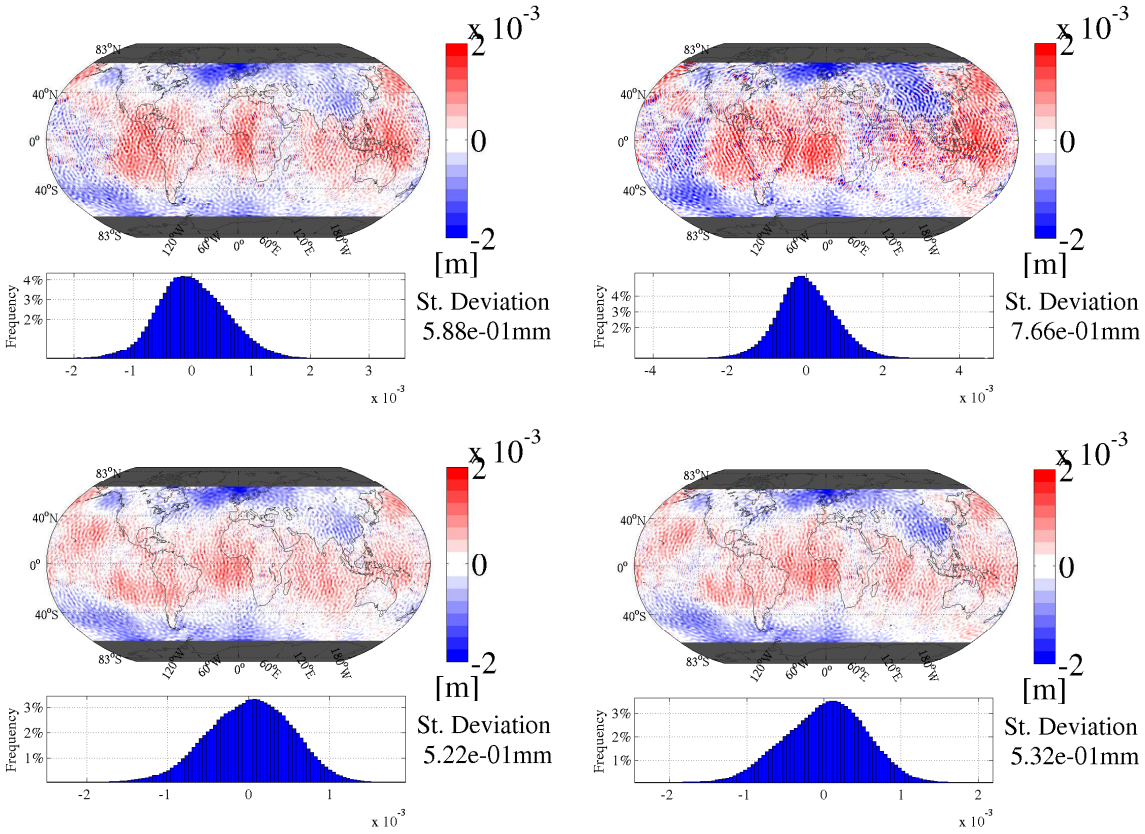

Figure 7.3.2: Closed-loop geoid height differences of 11-day d/o 120 "HIS" solutions. Results are latitude band-limited to $-65^o \leq \text{lat} \leq 65^o$. Top: nominal processing, bottom Wiese$_{1/20-11/120}$ processing (Table 7.1). Left: strategy 1, right: strategy 2.

Investigations concerning retrieval strategies for “HIS” solutions revealed the ability of Wiese parameterization to deliver equally good solutions with both strategies for regions covered by both pairs. The conclusions are based on simulations performed with specific error assumptions. If the assumptions for the de-aliasing model errors or the signal power in “AOHIS” models are not realistic, the conclusions might be different. Nevertheless, conclusions from the investigated Bender-type constellation support the ability of NGGMs to observe additionally the high frequency signals in atmosphere and ocean, and to deliver the full integrated “AOHIS” signal. This can be of a great value to the scientific community, due to the following reasons :

- Mean solutions will contain the full spectrum of non-tidal geophysical processes that comprise system Earth, free of de-aliasing model errors.
- Meaningful “HIS” solutions can be retrieved by the users through an a posteriori subtraction of mean “AO” fields.
- By-product of short-term (e.g. daily) solutions will be for the first time available. Since they will contain the full “AOHIS” signal, they could be of a great value to atmospheric science, opening doors to new fields of application.

Finally, it is worth to mention the possibility of a mixed strategy that could be investigated at the framework of future studies. High frequency signals that cannot be resolved at the short-term basis of a Wiese parameterization, could be reduced by a high-pass filtered “AO” de-aliasing. Assuming a daily parameterization, a cut-off frequency of $1/2$ days could be used to high-pass filter the “AO” time series. The de-aliasing of high-pass filtered “AO” signals would lead then to a better treatment of aliasing due to under-sampling, with an average solution however influenced by the high frequency part of the “AO” model errors.

Chapter 8

Conclusions

The main objective of this study was to investigate the potential of future LL-SST satellite missions in improving the knowledge of the gravity field of the Earth. The integral equation (short-arc) approach was used for the full-scale gravity field simulations. Stochastic models of the instrument errors expected to be applicable for NGGMs were used to assess their contribution to the error budget. At a first stage, simulations were performed for a GRACE-type polar pair, flying in a drag-free mode. The maximum resolution of the solutions was set to d/o 120, and the observation time period to one month.

Analysis of closed-loop simulations has exposed the insufficiency of numerical processing accuracy, when observations from new generation sensors such as a laser interferometer are used. It was shown that gravity field processing with double precision may be a limiting factor for exploiting the laser's nm-level accuracy. A new scheme of enhanced precision processing was proposed instead, where double precision and quadruple precision processing are used in different parts of the processing chain. Processing with enhanced precision leads to a reduction of processing errors induced by round-off errors which limit the system accuracy in case of double precision. Misclosures of noise-free closed-loop simulations in terms of geoid height differences for solutions complete to d/o 120, show improvements compared to the standard processing from $1.2 \times 10^{2}\,\mu$m to $5.4 \times 10^{-1}\,\mu$m in case of using ranges as observations and $3.4 \times 10^{1}\,\mu$m to $2.1 \times 10^{-2}\,\mu$m in case of range rates. At the same time, the computational times of this hybrid scheme are kept within reasonable limits for full-fledged gravity field processing. Results from noise propagation of a laser interferometer show that enhanced precision can efficiently handle laser measurements and take full advantage of their accuracy. Other error sources (e.g. accelerometers) have a considerable larger impact to the error budget than the laser interferometer. However, advances in sensor metrology and design of SFF constellations, may lead to reduction of these error levels, and thus necessitate the usage of enhanced numerical precision gravity field processing for NGGMs.

Error budget analysis of a polar pair NGGM scenario was performed with the double precision version of the simulator. It was concluded that the accelerometer instrument noise and temporal aliasing effects constitute the most significant error sources. Temporal aliasing refers to effects that mainly result from three individual error sources: under-sampling of non-tidal signal of interest (e.g. hydrology),

errors of de-aliasing models (atmospheric and oceanic part) and errors of ocean tide models. All three aliasing error sources result in similar gravity field error levels, from which temporal aliasing due to under-sampling of "AOHIS" signal is the most significant, leading to a 3.3×10^1 mm standard deviation of closed-loop geoid height differences for solutions complete to d/o 120. Propagation of accelerometer errors resulted in a standard deviation of 4.4×10^1 mm. The individual effects of laser, attitude and orbit errors have also been assessed and found to be less significant.

Methods of noise reduction have been investigated for a noise case considering all error sources. Frequency dependent data weighting proved to be a very efficient method to de-correlate colored noise present in the system. In case of processing with real data, a noise realization is not known a priori, and the dependency of noise on frequency can be estimated on the basis of residuals. In the performed simulations, a weight matrix was computed from the auto-covariance values of residuals. The preconditions of non-stationarity and ergodicity of the noise realization were satisfied by using residuals which contained only the effect of system errors and propagated accelerometer and laser noise. The weight matrix constructed from these residuals, considered time correlations among all epochs separated by a maximum lag of almost half a day. A noise case considering all error sources processed with this weight matrix, showed improvements over the complete error bandwidth. Standard deviations of geoid height differences were reduced from 6.45 cm to 0.52cm. Processing with co-parameterization of empirical accelerations did not show the same efficiency in reducing the propagated noise. The investigated models for empirical parameterization resulted in improvements at the higher, and degradations at the lower degree coefficients. This may be related to the applied gravity field approach which updates the set of empirical accelerations together with the boundary conditions of a short-arc (every 30 min), and should be further investigated. Using data weighting together with empirical parameterization, showed the same relative error behavior compared to a case considering only data weighting. In general, empirical estimated parameters may reduce the total error level, but can also absorb real gravity signals. The usage of frequency dependent data weighting is suggested as a more efficient method of noise reduction.

Temporal aliasing is one of the key limiting factors for the precision of NGGM gravity field solutions. Investigations were performed for a more complex SFF scenario with two pairs of satellites, consisting of one pair in a near-polar orbit and the other in an inclined orbit. This so-called Bender-type constellation resulted in major improvements of "AOHIS" solutions in terms of de-aliasing potential and recovery performance, translated into an increase in spatial resolution of 11-day solutions from 715 to 315 km compared to the polar pair. Treatment of temporal aliasing effects was also investigated at the level of gravity field processing. The Bender constellation results in an increase of temporal and spatial resolution. This facilitates the retrieval of high frequency gravity field information at large spatial scales. The *Wiese approach* takes advantage of this information and uses it as a natural de-aliasing of the long-term average solution. According to this parameterization, low resolution gravity fields are co-estimated at short time intervals together with the higher resolution gravity field which is sampled at a longer time interval. A fine-tuning of the Wiese approach for the chosen constellation was performed. Different temporal resolutions of daily, half-daily and 3-daily periods were among the investigated parameterization

choices. Validation was performed for the long-term as well as the short-term solutions. The SNR values of the short-term solutions in connection with the frequency at which they are sampled, play the most important role for the efficiency of the Wiese approach in mitigating temporal aliasing effects. Moving a step forward from Wiese parameterization, a two-step approach was developed in order to capture more signal variability than in single periods. This *sequential co-parameterization* exploits a larger retrievable space, by co-estimating intermediate-degree coefficients in longer periods (e.g. 3 days) additional to the low-degree coefficients co-estimated in shorter periods (e.g. 1 day). However, investigations concluded that the best results are obtained with a daily co-parameterization of a d/o 20 maximum resolution. The application of this parameterization led in a clear reduction of the stripes caused by aliasing, and of the total error levels. For a case considering only temporal aliasing due to under-sampling of "AOHIS" signal, the maximum spatial resolution was increased from 400 km to 285 km, and for a case considering all error sources from 320 km to 285 km half-wavelength. The key findings of the investigations performed with the Wiese approach can be summarized as follows:

- One day is the optimal sampling period for reducing the error levels in the solutions, since it provides the best compromise between the largest possible amount of signal that can be captured and the shortest time period in which it changes.
- The performance of Wiese processing at the medium-to-short wavelengths, is rather insensitive to the orbit choice of cycles or sub-cycles. The only prerequisite seems to be a uniform sampling at parameterized short periods (e.g. 1 day).
- Errors due to ocean tide model inaccuracies cannot be handled efficiently by a Wiese parameterization, and remain the biggest contributor to the aliasing error budget after applying the method.
- NGGMs could deliver the full spectrum of geophysical processes that comprise system Earth (i.e. "AOHIS"), free of de-aliasing model errors.
- Additional by-products of short-term (e.g. daily) "AOHIS" solutions available for the first time from a gravimetric satellite mission could be of a great value to atmospheric science, thus opening doors to new fields of application.

Acronyms

APG Lehrstuhl für Astronomische und Physikalische Geodäsie

ASD Amplitude Spectral Density

AU Astronomical Unit

CIO Conventional International Origin

CNES Centre National d'Études Spatiales

CRF (conventional) Celestial Reference Frame

CRS (conventional) Celestial Reference System

CSR Center for Space Research

CEDA Cummulative Error Degree Amplitude

CHAMP Challenging Minisatellite Payload

DDA Difference Degree Amplitude

DLR Deutsches Zentrum für Luft und Raumfahrt

EDA Error Degree Amplitude

ESA European Space Agency

EOP Earth Orientation Parameters

EWH equivalent water height

GFZ Deutsches Geoforschungszentrum

GIA Glacial Isostatic Adjustment

GPS Global Positioning System

GRACE Gravity Recovery and Climate Experiment

GRACE-FO GRACE Follow-OnGravity Recovery and Climate Experiment Follow-On

GRAIL Gravity Recovery and Interior Laboratory

GOCE Gravity field and steady-state Ocean Circulation Explorer

GRF Gradiometer Reference Frame

HL-SST High-Low Satellite-to-Satellite Tracking

IAT International Atomic Time

IAU International Astronomical Union

IERS International Earth Rotation Service

IMU Inertial Measurement Unit

JD Julian Date

KBR K-Band Ranging

LEO Low Earth Orbiter

LL-SST Low-Low Satellite-to-Satellite Tracking

LOS line-of-sight

LRI Laser Ranging Interferometer

LRZ Leibniz Rechnenzentrum

LSA Least Squares Adjustment

MJD Modified Julian Date

NASA National Aueronautics and Space Administration

NEQ Normal Equation

NGGM Next Generation Gravity Mission

OMC observed minus computed

OpenMP Open Multi-Processing

PECE Predict-Evaluate-Correct-Evaluate

PSD Power Spectral Density

RMS root mean square

SCA Star Camera Assembly

SDA Signal Degree Amplitude

SFF Satellite Formation Flight

SI Système International d'unités

SNR Signal-to-Noise Ratio

SOFA Standards Of Fundamental Astronomy

SST Satellite-to-Satellite

SST Satellite-to-Satellite Tracking

TRF (conventional) Terrestrial Reference Frame

TRS (conventional) Terrestrial Reference System

TT Terrestrial Time

UTC Universal Time Coordinated

UT Universal Time

List of Figures

List of Tables

Bibliography

Bender PL, Wiese DN, Nerem RS (2008) A possible dual-grace mission with 90 degree and 63 degree inclination orbits. In: in Proceedings, 3rd International Symposium on Formation Flying, Missions and Technologies. European Space Agency Symposium Proceedings, SP-654., ESA, ESA, Noordwijk, The Netherlands, jILA Pub. 8161

Bettadpur S (2013) CSR Level-2 Processing Standards Document for Product Release 05. University of Texas at Austin, URL ftp://podaac.jpl.nasa.gov/allData/grace/docs/L2-CSR0005_ProcStd_v4.0.pdf

Beutler G, Jäggi A, Mervart L, Meyer U (2010) The celestial mechanics approach: application to data of the grace mission. Journal of Geodesy 84(11):661–681, DOI 10.1007/s00190-010-0402-6, URL http://dx.doi.org/10.1007/s00190-010-0402-6

Board IS (2015) Iau sofa software collection. URL http://www.iausofa.org

Brockmann JM, Zehentner N, Höck E, Pail R, Loth I, Mayer-Gürr T, Schuh WD (2014) EGM_TIM_RL05 An independent geoid with centimeter accuracy purely based on the GOCE mission. Geophysical Research Letters 41(22):8089–8099, DOI 10.1002/2014GL061904, URL http://dx.doi.org/10.1002/2014GL061904

Chen JL, Wilson CR, Tapley BD (2011) Interannual variability of greenland ice losses from satellite gravimetry. Journal of Geophysical Research: Solid Earth 116(B7), DOI 10.1029/2010JB007789, URL http://dx.doi.org/10.1029/2010JB007789, b07406

Clohessy WH, Wiltshire RS (1960) Terminal guidance system for satellite rendezvous. J of the Aerospace Sciences 27(9):653–658

Daras I, Pail R, Murböck M, Yi W (2014) Gravity field processing with enhanced numerical precision for LL-SST missions. J Geod 89(2):99–110, DOI 10.1007/s00190-014-0764-2, URL http://link.springer.com/article/10.1007/s00190-014-0764-2

Ditmar P, Klees R, Liu X (2007) Frequency-dependent data weighting in global gravity field modeling from satellite data contaminated by non-stationary noise. J Geod 81(1):81–96, DOI 10.1007/s00190-006-0074-4

Dobslaw H, Flechtner F, Bergmann-Wolf I, Dahle C, Dill R, Esselborn S, Sasgen I, Thomas M (2013) Simulating high-frequency atmosphere-ocean mass variability for dealiasing of satellite gravity observations: AOD1b RL05: ATMOSPHERE-OCEAN MASS VARIABILITY: AOD1b. Journal of Geophysical Research: Oceans 118(7):3704–3711, DOI 10.1002/jgrc.20271, URL http://doi.wiley.com/10.1002/jgrc.20271

Dobslaw H, Bergmann-Wolf I, Dill R, Forootan E, Klemann V, Kusche J, Sasgen I (2015) The updated esa earth system model for future gravity mission simulation studies. Journal of Geodesy 89(5):505–513, DOI 10.1007/s00190-014-0787-8, URL http://dx.doi.org/10.1007/s00190-014-0787-8

Einarsson I, Hoechner A, Wang R, Kusche J (2010) Gravity changes due to the sumatra-andaman and nias earthquakes as detected by the grace satellites: a reexamination. Geophysical Journal International 183(2):733–747, DOI 10.1111/j.1365-246X.2010.04756.x, URL http://dx.doi.org/10.1111/j.1365-246X.2010.04756.x

Elsaka B (2010) Simulated satellite formation flights for detecting the temporal variations of the earth's gravity field. PhD thesis, Technische University of Bonn

Elsaka B, Raimondo JC, Brieden P, Reubelt T, Kusche J, Flechtner F, Pour SI, Sneeuw N, Müller J (2014) Comparing seven candidate mission configurations for temporal gravity field retrieval through full-scale numerical simulation. J Geod 88(1):31–43, DOI 10.1007/s00190-013-0665-9

ESA (2010) Assessment of a next generation mission to monitor the variations of Earth's gravity field. URL http://emits.sso.esa.int/emits-doc/ESTEC/AO7317_RD4-NGGM_FinalReport_Issue2.pdf, ESTEC Contract No. 22643/09/NL/AF, Final Report, Issue 2, Thales Alenia Space report SDRP-AI-0688

ESA (2011) Assessment of a next generation gravity mission to monitor the variations of Earth's gravity field. URL http://emits.sso.esa.int/emits-doc/ESTEC/AO7317_RD5-Final_Report_Issue_1_w_ESA_dissemination_rights.pdf, ESA Contract No. 22672/09/NL/AF, Final Report, Thales Alenia Space report SDRP-AI-0688

Ettl M (2013) Hochgenaue numerische lösung von bewegungsproblemen mit frei wählbarer stellengenauigkeit. PhD thesis, Technische Universität München, Munich, URL http://nbn-resolving.de/urn/resolver.pl?urn:nbn:de:bvb:91-diss-20121128-1108595-0-5

Flechtner F, Morton P, Watkins M, Webb F (2014a) Status of the GRACE Follow-On Mission. In: Marti U (ed) Gravity, Geoid and Height Systems, no. 141 in International Association of Geodesy Symposia, Springer International Publishing, pp 117–121, URL http://link.springer.com.eaccess.ub.tum.de/chapter/10.1007/978-3-319-10837-7_15

Flechtner F, Sneeuw N, Schuh WD (eds) (2014b) Observation of the System Earth from Space - CHAMP, GRACE, GOCE and future missions. Advanced Technologies in Earth Sciences, Springer Berlin Heidelberg, Berlin, Heidelberg, URL http://link.springer.com/10.1007/978-3-642-32135-1

Friis-Christensen E, Lühr H, Knudsen D, Haagmans R (2008) Swarm - an earth observation mission investigating geospace. Advances in Space Research 41(1):210–216, DOI 10.1016/j.asr.2006.10.008, URL http://www.sciencedirect.com/science/article/pii/S0273117706005497

Gruber T, Murböck M, NGGM-D T (2014a) e2.motion - earth system mass transport mission (square) - concept for a next generation gravity field mission. Deutsche Geodätische Kommission der Bayerischen Akademie der Wissenschaften, Reihe B, Angewandte Geodäsie 318, C.H. Beck, URL http://dgk.badw.de/fileadmin/docs/b-318.pdf

Gruber T, Murböck M, Van Dam T, Weigelt M (2014b) Assessment of Satellite Constellations for Monitoring the Variations in Earth Gravity Field "SC4MGV" - Technical Note 1. ESA Contract AO/1-7317/12/NL/AF

Han SC, Jekeli C, Shum CK (2004) Time-variable aliasing effects of ocean tides, atmosphere, and continental water mass on monthly mean grace gravity field. Journal of Geophysical Research: Solid Earth 109(B4):n/a–n/a, DOI 10.1029/2003JB002501, URL http://dx.doi.org/10.1029/2003JB002501, b04403

Han SC, Shum CK, Bevis M, Ji C, Kuo CY (2006) Crustal dilatation observed by grace after the 2004 sumatra-andaman earthquake. Science 313(5787):658–662, DOI 10.1126/science.1128661, URL http://science.sciencemag.org/content/313/5787/658, http://science.sciencemag.org/content/313/5787/658.full.pdf

Hofmann-Wellenhof B, Moritz H (2006) Physical Geodesy. Springer Vienna, URL http://link.springer.com/10.1007/978-3-211-33545-1

Hofmann-Wellenhof B, Lichtenegger H, Collins J (2001) Global Positioning System. Springer Vienna, Vienna, URL http://link.springer.com/10.1007/978-3-7091-6199-9

Ilk KH, Flury J, Rummel R, Schwintzer P, Bosch W, Haas C, Schröter J, Stammer D, Zahel W, Miller H, Dietrich R, Huybrechts P, Schmeling H, Wolf D, Götze HJ, Riegger J, Bardossy A, Güntner A, Gruber T (2005) Mass transport and mass distribution in the earth system. Proposal for a german priority research program, 2nd edition, GOCE-Projektbüro TU München, GeoForschungsZentrum Potsdam, URL http://www.massentransporte.de/fileadmin/Dokumente/programmschrift-Ed2.pdf

Iran Pour S, Sneeuw N, Daras I, Pail R, Murböck M, Gruber T, Tonetti S, Cornara S, Weigelt M, Van Dam T, Visser P, Teixeira da Encarnação (2015) Assessment of satellite constellations for monitoring the variations in earth gravity field - SC4MGV. ESA - ESTEC Contract No. AO/1-7317/12/NL/AF, Final Report

Jin S, Chambers DP, Tapley BD (2010) Hydrological and oceanic effects on polar motion from grace and models. Journal of Geophysical Research: Solid Earth 115(B2):n/a–n/a, DOI 10.1029/2009JB006635, URL http://dx.doi.org/10.1029/2009JB006635, b02403

Kaula WM (1966) Theory of Satellite Geodesy. Blaisdell, Toronto

Kim J (2000) Simulation study of a low-low satellite-to-satellite tracking mission. PhD thesis, University of Texas at Austin

Knocke P, Ries J, Tapley B (1988) Earth radiation pressure effects on satellites. In: Astrodynamics Conference, American Institute of Aeronautics and Astronautics, URL http://arc.aiaa.org/doi/abs/10.2514/6.1988-4292

Koch K, Kuhlmann H, Schuh WD (2010) Approximating covariance matrices estimated in multivariate models by estimated auto- and cross-covariances. Journal of Geodesy 84(6):383–397, DOI 10.1007/s00190-010-0375-5, URL http://dx.doi.org/10.1007/s00190-010-0375-5

Lambert A, Huang J, van der Kamp G, Henton J, Mazzotti S, James TS, Courtier N, Barr AG (2013) Measuring water accumulation rates using GRACE data in areas experiencing glacial isostatic adjustment: The Nelson River basin. Geophys Res Lett 40(23):2013GL057,973, DOI 10.1002/2013GL057973, URL http://onlinelibrary.wiley.com/doi/10.1002/2013GL057973/abstract

Luthcke SB, Sabaka T, Loomis B, Arendt A, McCarthy J, Camp J (2013) Antarctica, Greenland and Gulf of Alaska land-ice evolution from an iterated GRACE global mascon solution. Journal of Glaciology 59(216):613–631, DOI 10.3189/2013JoG12J147

Mayer-Gürr T (2006) Gravitationsfeldbestimmung aus der Analyse kurzer Bahnbögen am Beispiel der Satellitenmissionen CHAMP und GRACE. PhD thesis, URL http://hss.ulb.uni-bonn.de/2006/0904/0904.htm

Mayer-Gürr T, et al. (2012) The new combined satellite-only model GOCO03s. Abstract submitted to GGHS2012. Venice, Italy

Montenbruck O, Gill E (2000) Satellite Orbits. Springer Berlin Heidelberg, Berlin, Heidelberg, URL http://link.springer.com/10.1007/978-3-642-58351-3

Murböck M (2015) Virtual constellations of next generation gravity missions. DGK, Reihe C 750, Verlag der Bayerischen Akademie der Wissenschaften, URL http://dgk.badw.de/fileadmin/docs/c-750.pdf

Murböck M, Pail R, Daras I, Gruber T (2014) Optimal orbits for temporal gravity recovery regarding temporal aliasing. J Geod 88(2):113–126, DOI 10.1007/s00190-013-0671-y

Pail R, Bingham R, Braitenberg C, Dobslaw H, Eicker A, Güntner A, Horwath M, Ivins E, Longuevergne L, Panet I, Wouters B (2015) Science and user needs for observing global mass transport to understand global change and to benefit society. Surveys in Geophysics 36(6):743–772, DOI 10.1007/s10712-015-9348-9

Panet I, Flury J, Biancale R, Gruber T, Johannessen J, van den Broeke M, van Dam T, Gegout P, Hughes C, Ramillien G, Sasgen I, Seoane L, Thomas M (2013) Earth system mass transport mission (e.motion): A concept for future earth gravity field measurements from space. Surveys in Geophysics 34(2):141–163, DOI 10.1007/s10712-012-9209-8, URL http://dx.doi.org/10.1007/s10712-012-9209-8

Petit G, Luzum B (2010) IERS Conventions (2010); Technical Note 36. Frankfurt am Main:Verlag des Bundesamts für Kartographie und Geodäsie

Prange L (2010) Global Gravity Field Determination Using the GPS Measurements Made Onboard the Low Earth Orbiting Satellite CHAMP. Geodätische-geophysikalische Arbeiten in der Schweiz, Inst. für Geodäsie und Photogrammetrie, URL https://books.google.de/books?id=2k-6twAACAAJ

Ramillien G, Biancale R, Gratton S, Vasseur X, Bourgogne S (2011) GRACE-derived surface water mass anomalies by energy integral approach: application to continental hydrology. J Geod 85(6):313–328, DOI 10.1007/s00190-010-0438-7, URL http://link.springer.com/article/10.1007/s00190-010-0438-7

Ray RD (1999) A global ocean tide model from topex/poseidon altimetry: Got99.2. Tech. rep., NASA Technical Memorandum 209478

Reigber C (1995) CHAMP: A Challenging Micro-satellite Payload for Geophysical Research and Application; Feasibility Study for the German Space Agency (DARA). Technical notes. Appendices. URL https://books.google.de/books?id=ho7eMgEACAAJ

Reubelt T, Sneeuw N, Sharifi M (2010) Future mission design options for spatio-temporal geopotential recovery. In: Mertikas SP (ed) Gravity, Geoid and Earth Observation, International Association of Geodesy Symposia, vol 135, Springer Berlin Heidelberg, pp 163–170, DOI 10.1007/978-3-642-10634-7_22, URL http://dx.doi.org/10.1007/978-3-642-10634-7_22

Rietbroek R, Fritsche M, Brunnabend SE, Daras I, Kusche J, Schröter J, Flechtner F, Dietrich R (2012) Global surface mass from a new combination of GRACE, modelled OBP and reprocessed GPS data. Journal of Geodynamics 59-60:64–71, DOI 10.1016/j.jog.2011.02.003

Riva RE, Gunter BC, Urban TJ, Vermeersen BL, Lindenbergh RC, Helsen MM, Bamber JL, van de Wal RS, van den Broeke MR, Schutz BE (2009) Glacial Isostatic Adjustment over Antarctica from combined ICESat and GRACE satellite data. Earth and Planetary Science Letters 288(3-4):516–523, DOI 10.1016/j.epsl.2009.10.013, URL http://linkinghub.elsevier.com/retrieve/pii/S0012821X09006128

Rummel R (2003) How to climb the gravity wall. In: Beutler G, Drinkwater M, Rummel R, Von Steiger R (eds) Earth Gravity Field from Space - From Sensors to Earth Sciences, Space Sciences Series of ISSI, vol 17, Springer Netherlands, pp 1–14, DOI 10.1007/978-94-017-1333-7_1, URL http://dx.doi.org/10.1007/978-94-017-1333-7_1

Rummel R, Yi W, Stummer C (2011) GOCE gravitational gradiometry. J Geod 85(11):777–790, DOI 10.1007/s00190-011-0500-0, URL http://link.springer.com/article/10.1007/s00190-011-0500-0

Sanchez BV (1975) Rotational dynamics of mathematical models of the nonrigid earth. PhD Thesis p 29, URL http://adsabs.harvard.edu/abs/1975PhDT.....29S

Savcenko R, Bosch W (2008) EOT08a - empirical ocean tide model from multi-mission satellite altimetry. Tech. Rep. Report No. 81, Deutsches Geodätisches Forschungsinstitut (DGFI)

Schall J, Eicker A, Kusche J (2014) The ITG-Goce02 gravity field model from GOCE orbit and gradiometer data based on the short arc approach. J Geod 88(4):403–409, DOI 10.1007/s00190-014-0691-2

Schneider M (1969) Outline of a general orbit determination method. In: Champion KSW, Smith PA, Smith-Rose RL (eds) Space Research IX, Proceedings of Open Meetings of Working Groups (OMWG) on Physical Sciences of the 11th Plenary Meeting of the Committee on Space Research (COSPAR), Tokyo, North-Holland Publishing Company, pp 37–40, mitteilungen aus dem Institut für Astronomische und Physikalische Geodäsie, Nr. 51

Schrama EJO, Wouters B (2011) Revisiting greenland ice sheet mass loss observed by grace. Journal of Geophysical Research: Solid Earth 116(B2), DOI 10.1029/2009JB006847, URL http://dx.doi.org/10.1029/2009JB006847, b02407

Shampine LF, Gordon MK (1975) Computer solution of ordinary differential equations: the initial value problem. W.H. Freeman, San Francisco

Sheard BS, Heinzel G, Danzmann K, Shaddock DA, Klipstein WM, Folkner WM (2012) Intersatellite laser ranging instrument for the GRACE follow-on mission. J Geod 86(12):1083–1095, DOI 10.1007/s00190-012-0566-3

Sneeuw N, Flury J, Rummel R (2005) Science requirements on future missions and simulated mission scenarios. In: Flury J, Rummel R (eds) Future Satellite Gravimetry and Earth Dynamics, Springer New York, pp 113–142, DOI 10.1007/0-387-33185-9_10, URL http://dx.doi.org/10.1007/0-387-33185-9_10

Tapley BD, Bettadpur S, Ries JC, Thompson PF, Watkins MM (2004) GRACE Measurements of Mass Variability in the Earth System. Science 305(5683):503–505, DOI 10.1126/science.1099192, URL http://www.sciencemag.org/content/305/5683/503

Velicogna I, Wahr J (2013) Time-variable gravity observations of ice sheet mass balance: Precision and limitations of the grace satellite data. Geophysical Research Letters 40(12):3055–3063, DOI 10.1002/grl.50527, URL http://dx.doi.org/10.1002/grl.50527

Vetter JR, Nerem RS, Cefola P, Hagar H (1993) A historical survey of Earth gravitational models used in astrodynamics from Sputnik and transit to GPS and TOPEX. Proceedings of the AIAA/AAS Astrodynamics Specialist Conference, AAS Publications Office, San Diego, Calif.

Visser PNAM, Sneeuw N, Reubelt T, Losch M, Van Dam T (2010) Space-borne gravimetric satellite constellations and ocean tides: aliasing effects. Geophysical Journal International 181(2):789–805, DOI 10.1111/j.1365-246X.2010.04557.x, URL http://dx.doi.org/10.1111/j.1365-246X.2010.04557.x

Weigelt M, Sneeuw N, Schrama E, Visser P (2013) An improved sampling rule for mapping geopotential functions of a planet from a near polar orbit. Journal of Geodesy 87(2):127–142, DOI 10.1007/s00190-012-0585-0, URL http://dx.doi.org/10.1007/s00190-012-0585-0

Wiese D, Folkner W, Nerem R (2009) Alternative mission architectures for a gravity recovery satellite mission. Journal of Geodesy 83(6):569–581, DOI 10.1007/s00190-008-0274-1, URL http://dx.doi.org/10.1007/s00190-008-0274-1

Wiese D, Nerem R, Lemoine F (2012) Design considerations for a dedicated gravity recovery satellite mission consisting of two pairs of satellites. Journal of Geodesy 86(2):81–98, DOI 10.1007/s00190-011-0493-8, URL http://dx.doi.org/10.1007/s00190-011-0493-8

Wiese DN, Nerem RS, Han SC (2011a) Expected improvements in determining continental hydrology, ice mass variations, ocean bottom pressure signals, and earthquakes using two pairs of dedicated satellites for temporal gravity recovery. J Geophys Res : Solid Earth 116(B11405), DOI 10.1029/2011JB008375

Wiese DN, Visser P, Nerem RS (2011b) Estimating low resolution gravity fields at short time intervals to reduce temporal aliasing errors. Adv Space Res 48:1094–1107, DOI 10.1016/j.asr.2011.05.027

Wouters B, Riva REM, Lavallée DA, Bamber JL (2011) Seasonal variations in sea level induced by continental water mass: First results from GRACE: SEASONAL PASSIVE SEA LEVEL FROM GRACE. Geophysical Research Letters 38(3):n/a–n/a, DOI 10.1029/2010GL046128, URL http://doi.wiley.com/10.1029/2010GL046128

Yi W (2012) The Earth's gravity field from GOCE. PhD thesis, Technische Universität München, URL http://mediatum.ub.tum.de/node?id=1091412

Zenner L, Fagiolini E, Daras I, Flechtner F, Gruber T, Schmidt T, Schwarz G (2012) Non-tidal atmospheric and oceanic mass variations and their impact on GRACE data analysis. Journal of Geodynamics 59-60:9–15, DOI 10.1016/j.jog.2012.01.010